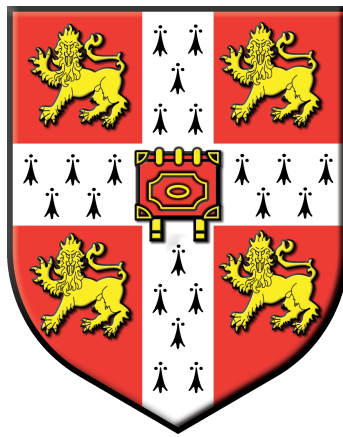


Nanostructured Transparent Conducting Oxides *via* Blockcopolymer Patterning



Joung Youn Ellie Kim

Sidney Sussex College
Supervisor: Prof. Ullrich Steiner
Department of Physics
December, 2012

This dissertation is submitted for the degree of Doctor of Philosophy.

Declaration

This thesis is the result of my own work and includes nothing which is the outcome of work done in collaboration except where specifically indicated in the text.

I declare that no part of this work has been submitted for a degree or other qualification at this or any other university.

This thesis does not exceed the word limit of 60,000 words set by the Physics and Chemistry Degree Committee.

Joung Youn Ellie Kim, December 2012

Acknowledgements

Completion of this dissertation would not have been possible without the support and inspiration of many.

First and foremost I would like to thank my supervisor Prof. Ullrich Steiner, who has always been there for help and guidance as well as moral support. Your scientific insights have been invaluable to my journey here. Your values and insights on professionalism and life in general, have also made a positive impact on me.

I am truly grateful for having been part of such a wonderful research group, Thin Film and Interfaces Group (TFI). Thank you very much to all the current and past members for your friendliness, willingness for help, interesting scientific discussions, and looking over my work to give feedback whenever I was in need: Alexander Finnemore, Mathias Kolle, Silvia Vignolini, Sven Hüttner, Alessandro Sepe, Gen Kamita, Maik Scherer, Katherine Thomas, Li Li, Pedro Cunha, Pola Goldberg-Oppenheimer, Sarah Rong, Stefano Salvatore, Rosa Poetes, Xiaoyuan Sheng and Yuan Zhou, Ahu Gumrah Perry.

Further afield, I would like to thank the members of Nokia research centre: Dr. Chris Bower, Dr. Piers Andrews, Dr. Di Wei, Markku Rouvala, Tapani Ryhänen. Your financial support as well as scientific input have been invaluable.

Outside of TFI, I am indebted to the friends and colleagues in the Cavendish Laboratory. First, I would like to thank the members of Nanophotonics and Optoelectronics group as well as the professors (Prof. Jerome Baumberg, Prof. Richard Friend, Prof. Henning Sirringhaus, and Prof. Neil Greenham). I shared great fun with you in the annual SNAP Winterschool, during lunchtime at the Kapitza kitchen area and in other social events. In addition, the random scientific discussions in these social moments sparked many good ideas and sometimes helped me get out of low points in my research. Especially, I would like to thank Dr. DH Ko for showing me the initial steps for synthesis of ZnO nano crystals and providing me with career related advice. I am thankful to Dr. Yana Vaynzof for the collaboration of solar cell work and the XPS measurements as well as other scientific insights. I am grateful to Dr. K.K. Banger for the help with conductivity measurements as well as the collaborative work on the amorphous TCO. His insights on sol-gel chemistry as well as TCO's in general have been invaluable for my projects. I would also like to

acknowledge the help of Dr. Dinesh Kabra and Dr. Sumeet Mahajan, who offered lending ears and advice during difficult times of my research.

I would also like to thank the administrative and support staffs of Cavendish and Nanoscience Centre: Richard and Sue Guymer, Tom Mitchell, Tracy Inman, Stefani Gerber, Suresh Mistry, Pete Bone, Owen Dunn, thank you for ensuring a resourceful and well-functioning working environment.

There are many scientists from outside of the the Cavendish(Physics Department), I am extremely grateful to. I am thankful to Tony Andrews, Dr. Marry Vickers at the Department of Material Sciences for the help with XRD Dr. Caterina DuCati (same dept) for the HRTEM imaging. All of you have always made time to help me, and thanks to that, I was able to solve important questions in my research.

I would also like to express my gratitude to the scientists from outside of Cambridge University. I am grateful to Professor Ulrich Wiesner at Cornell University for providing some of the block-copolymer used in my study as well as his scientific advice, Professor Henry Snaith at Oxdord University and his group members, Dr. Agnese Abrusci, Varun Sivaram, for the advice and the actual building of DSSC solar cells, Professor Roy Gordon at Harvard University and his post-doc Dr. Jae Young Heo for the collaborative preliminary studies on ALD of SnO₂. Professor Dominik Eder at University of Muenster for providing insightful scientific advice and support on materials characterisation and the collaborative work on zeolite materials (not included in the thesis).

I want to acknowledge Sidney Sussex College and its members for providing me with a great scholarly atmosphere and an active College life. I would like to thank the Graduate Tutors: Dr. Julius Ross and Dr. Iain Black for their efforts to provide support in any way they could.

My journey in Cambridge would have been incomplete without the company and support from my friends. I would like to thank all of them for the fun times, lending their ears, and being such great teachers of life. Especially, I would like to thank Nate Lipkowitz for his friendship, tireless moral support and editing my thesis.

Finally, I am indebted to my family for their love and existence. It is not an exaggeration that their support carried me through to the end. Thank you mum, dad and Lauren.

Joung Youn Ellie Kim, December 2012

Introduction

Motivation

Transparent conducting oxides (TCOs) have been the dominant material for transparent electrodes for decades. Over the last decade, there have been dramatic technological advances in portable electronics, solar cells, flexible electronics, transistors, multifunctional windows, and numerous other devices that feature transparent electrodes. The heavy use of transparent conducting oxides (TCO) in these increasingly important applications, coupled with the increasing cost of common TCO precursors and potential opportunities in other applications, has stimulated wide research interest on the science of a variety of transparent conductors.

The majority of TCO materials research over the past few decades has been focused on minor variants of three main n-type TCOs: In_2O_3 , SnO_2 , and ZnO thin films. These, mainly empirical, studies have been executed with an aim to improve the performance of these semiconducting metal oxides and meet ever-increasing industrial requirements. It is a fair statement that currently this field of research has reached maturity.

In recent years, however, efforts have begun to develop completely new TCO materials including p-type TCOs such as CuInO_2 , CuGaO_2 , SrCu_2O_2 and CuAlO_2 . In addition, contrary to the conventional perception that crystalline materials exhibit superior properties, a new class of amorphous TCOs has emerged, ones that demonstrate equal or even better properties compared to their crystalline counterparts.

Furthermore, studies on transparent conductors which are not TCO-based have emerged in the recent years. These materials include conductive polymers, graphene, carbon nanotubes, and metal grids; each of the material system has its own challenges and the research efforts to overcome such challenges are ongoing.

Another emerging areas of transparent conductors research is to create a new class of TCO materials with additional engineered (or non-engineered) properties. This

can extend the possibilities for improved or completely new device architectures and applications. Therefore, it behooves the scientific community to develop TCO materials that also possess other specific, useful properties such as bandgap, work function, surface roughness, nanostructure, and thermal/chemical resistivity and diffusivity.

For example, TCO materials which are also transparent in ultraviolet region can be utilised in applications such as UV-sensors, anti-biostatic activity and optical detection of DNA and nucleotides. For this, instead of conventional TCOs which have band gaps ~ 3 eV, a large band gap TCO such as β - Ga_2O_3 (~ 4.8 eV) is found to be more suitable.

Nano-structuring of TCOs is another example. Conventionally, TCOs have been used as a planar transparent electrode, which only required a 2D film form of TCO. However, the advances in lithography techniques as well as solution processing and chemical vapour deposition methods are now enabling fabrication of 3D, nano-structured TCOs. Nanostructuring of TCO implies engineering in a nano-scale feature size as well as high internal surface area of the material. These materials can be integrated into complex hybrid devices (e.g. organic-inorganic hybrid solar cells) or used as a functional material on its own (e.g. thermochromic or electrochromic window, gas sensor).

Despite the vast number of publications and industrial interest in TCO materials, the efforts to develop these new types of materials have only started recently. Although premature, such efforts have a high potential to significantly change the paradigm for a technology or be a catalyst for another. This dissertation aims to make a contribution to this growing field of research by describing the fabrication, processing, and application of 3D, nano-structured transparent conducting oxide materials.

Bibliography:

- [1] Hosono, H. and Paine, D.C. and Ginley, D.S., (2010), Handbook of Transparent Conductors, Springer
- [2] Ellmer, K., (2012) *Past achievements and future challenges in the development of optically transparent electrodes*, Nature Photonics, **6** (12), 809-817

Thesis Overview

The aim of this thesis was to develop a new class of TCO material in thin film form, one featuring a mesoporous structure with a 20-40 nm length scale. The microphase-separation of block copolymer was exploited for patterning the TCO materials into this nanostructure.

As portable electronics become more widespread and integrated into daily life, and impending energy shortages drive progress towards more efficient and economical photovoltaic technologies, the development of fabrication routes to nanostructured TCO has become a subject of study for many. This thesis concentrates on the development of zinc oxide (ZnO) based materials.

One of the more common TCOs, ZnO has many potential applications in piezoelectric devices, organic (and dye-sensitised) photovoltaics, gas sensors, and so on. Unfortunately, nanostructured ZnO has been particularly difficult to realise, due to its rapid crystallisation into wurtzite crystals. Therefore, much of this work's focus lies in bypassing the widely recognised problems of creating such a nanostructured material, and its processing into a thin film form useful for many applications.

The first chapter of this work reviews the main principles of transparent conducting oxides, trends in past research, and current directions of inquiry. Chapter 2 presents the basic underlying principles of block copolymer self-assembly, and discusses its application to the creation of mesoporous metal oxides. Broadly speaking, there are two different ways to do so – either as a sacrificial template, or as a structure guiding agent. Both uses of BCP are demonstrated throughout this work.

Chapter 3 describes the experimental methods used in this study, including approaches to film processing as well as characterization techniques. In Chapter 4, a reliable and controllable route to preparing 3D bicontinuous polymeric template is presented, which employs phase separation of block copolymer. Using the templates developed in Chapter 4, two fabrication routes to ZnO based materials are presented in Chapter 5 and 6.

In Chapter 5, atomic layer deposition was utilised to realise 3D structures of ZnO with 20-40 nm length scale, exploiting its ability to conformally deposit one layer at a time. These structures include an extremely periodic gyroid structure, as well as a bicontinuous wormlike morphology. This mesoporous ZnO was processed into thin film form, and its use was demonstrated in an inverted P3HT-ZnO hybrid solar cell.

In Chapter 6, a solution impregnation approach was explored, using sol gel of a

recently developed amorphous TCO material, In-Ga-ZnO. Various thin film processing techniques were explored to arrive at the optimum fabrication route to 3D mesoporous In-Ga-ZnO. Upon electrical and optical characterisation, this material revealed excellent transparency and electrical conductivity even in mesoporous form, exhibiting great potential for use as a transparent electrode.

Chapter 7 presents a different approach to the previous chapters, where block copolymer was used not as a template, but as a structure guiding agent to fabricate 3D nanostructured ZnO. Due to its simplicity and elegance, this bottom-up coassembly method has been utilised and well-established for other metal oxide systems, but hardly applied to zinc oxide successfully. The issues of rapid crystallisation were bypassed by first synthesising ZnO nano crystals, and incorporating them into the BCP nano-architecture.

Finally, Chapter 8, concludes this work by summarising the results and insights gained, and by presenting some preliminary results for possible future work.

Publications and Conferences

Publications

E. Kim, K.K. Banger, H. Siringhaus, and U. Steiner. “Fabrication of 3D mesoporous amorphous I(G)ZO” *In Preparation*.

E. Kim, Y. Vaynzof, S. Guldin, and U. Steiner. “Atomic Layer Deposition of Gyroid ZnO Using Self-Assembled Blockcopolymer Template” *In Preparation*.

E. Kim, Y. Vaynzof, D.H. Ko and U. Steiner. “Fabrication of Mesoporous ZnO via Block-copolymer directed Assembly of nc-ZnO for Organic Solar Cell Application” *In Preparation*.

Conferences

E. Kim, S. Guldin, and B. Ehrler, U. Steiner. “Atomic Layer Deposition of Three-Dimensional Gyroid ZnO Using Self-Assembled Blockcopolymer Template” *Winter-school on Chemistry and Physics of Materials*, 2011.

E. Kim, S. Vignolini, S and U. Steiner. “Highly-Ordered, Three-Dimensional Gyroid structure of (Al:)ZnO by Atomic Layer Deposition” *Transparent Conductive Materials*, 2010.

Contents

Declaration	i
Acknowledgements	ii
Introduction	iv
Publications and Conferences	viii
1 Transparent Conducting Oxides	1
1.1 Introduction	1
1.2 Electrical Conductivity of TCO	2
1.3 Optical properties of TCO	5
1.4 Conventional TCO Materials	7
1.5 Amorphous TCO	9
1.6 Nanostructured TCOs	12
2 Blockcopolymer Self Assembly and Its Use in Nanotechnology	21
2.1 Phase separation in block copolymers	21
2.1.1 Macrophase separation of Polymer Blends	21
2.1.2 Microphase Separation of BCP	22
2.1.3 The Gyroid (G) Phase	25
2.2 Application of Blockcopolymer Patterning in Nanotechnology	28
3 Techniques and Instrumentation	36
3.1 Fabrication Techniques	36
3.1.1 Thin Film Deposition	36
3.1.2 Atomic Layer Deposition	38
3.1.3 Sol-Gel	40
3.2 Characterisation Techniques	42
3.2.1 Electron Microscopy	42
3.2.2 X-ray Diffraction	44
3.2.3 Dynamic Light Scattering	45

3.2.4	X-ray Photoelectron Spectroscopy	47
3.2.5	Ellipsometry	48
3.2.6	Solar Cells Characterisation	51
4	Fabrication of Porous Polymer Templates	56
4.1	Introduction	56
4.2	Experimental	59
4.2.1	Materials	59
4.2.2	Fabrication Steps	60
4.3	Results and Discussion	62
4.3.1	Gyroid structure	62
4.3.2	Wormlike Structure	67
4.4	Conclusions	76
5	Fabrication of 3D Mesoporous ZnO via Atomic Layer Deposition	80
5.1	Introduction	80
5.2	Experimental	82
5.3	Results and Discussion	84
5.3.1	Mesoporous ZnO structures preparation	84
5.3.1.1	Polymer templates	84
5.3.1.2	ALD deposition of ZnO onto PS templates	85
5.3.1.3	Deposition temperature	92
5.3.1.4	Mesoporous ZnO characterization	93
5.3.1.5	X-ray diffraction (XRD)	93
5.3.1.6	X-ray photoemission spectroscopy (XPS)	94
5.3.1.7	Potential application in hybrid photovoltaics	95
5.4	Conclusions	97
6	Fabrication of 3D Amorphous I(G)ZO via Solution-Impregnation	102
6.1	Introduction	103
6.2	Experimental	106
6.3	Results and Discussion	109
6.3.1	Chemical compatibility	109
6.3.2	Replication of I(G)ZO by solution impregnation	109
6.3.2.1	Infiltration in bulk (gyroid samples)	111
6.3.2.2	Preparation of thin films	112
6.3.2.3	Further Characterisation	117
6.4	Conclusions and Future Work	123

7	Fabrication of Mesoporous ZnO via Blokcopolymer Co-Assembly	128
7.1	Introduction	128
7.2	Experimental	131
7.3	Results and Discussion	134
7.3.1	Solvent and size requirements for nc-ZnO	134
7.3.2	Thin film Deposition methods	135
7.3.3	Potential in Solar cell Applications	142
7.4	Conclusions	144
8	Conclusions and Potential Future Work	148

Chapter 1

Transparent Conducting Oxides

1.1 Introduction

Transparent conducting oxides (TCO) are semiconductors with two conjugate properties electrical conductivity and optical transparency. Because such a combination of properties are extremely useful for electrode materials in electronic applications such as displays, solar cells, and transistors, TCOs have been subject of intense research ever since they were discovered a century ago.^[1] Normally, conducting materials such as metals have low optical transparency, while transparent oxides exhibit poor conductivity due to the coupled behaviour of the two properties. TCOs are oxide semiconductors that have a band gap ($\approx 3\text{eV}$) large enough for optical transparency yet small enough for sufficiently good conductivity.^[2]

Commercially, thin films of indium-tin-oxide (ITO) have been the standard material used for transparent electrodes in optoelectronic devices. However, the high cost and scarcity of indium as well as difficulties of processing ITO has motivated a search for other materials that can potentially replace ITO as demand grows. Commonly investigated replacement materials include doped zinc oxide (ZnO), indium oxide (In_2O_3) and tin oxide (SnO_2).

Recent TCO research focuses on developing thin films of these materials with particular desirable properties, such as conductivity and carrier concentration of the thin films depending on their crystallinity and deposition methods. A thin film transparent electrode generally requires a carrier concentration on the order of 10^{20} cm^{-3} , at minimum, and a band-gap energy above 3 eV.^[1,3] The materials which satisfy these requirements include both n-type and p-type semiconductors but most attention has been given to n-type semiconductor oxide materials for preparation of transparent electrodes; however, p-type semiconductors are starting to be studied more recently.^[1]

The main focus in transparent electrode research has been on achieving a thin film of resistivity comparable to that of ITO by empirical routes. However, technological advances in electronics shifted the attention to developing new classes of TCOs with controllable additional properties such as tunable work function, conductivity, surface area, and length scale.

In this chapter, we review the basic principles of TCO and the recent developments of TCO research, leading to the discussion of nanostructured TCOs and some of their emerging applications such as surface coating and organic photovoltaics.

1.2 Electrical Conductivity of TCO

The electrical conductivity σ in bulk transparent conducting oxides (TCOs) can be derived starting from Drude's free-electron theory.^[4] As most TCO materials are n-type semiconductors, the charge carriers in question are conduction band electrons. Since the natural frequency of electrons are negligible compared to the frequencies of interest- visible (VIS) and near infrared (NIR) with respect to the ion core, the

(dc) conductivity can be given in a simplified term:

$$\sigma = \frac{ne^2\tau}{m^*} \quad (1.1)$$

depends on the density of charge carriers n and their mobility μ given by

$$\mu = \frac{e\tau}{m^*} \quad (1.2)$$

Here, the relaxation time, τ is the mean time between scattering events and m is the effective mass of the conduction electron in the crystal lattice. The mobility (and therefore, conductivity) is fundamentally limited by the relationship between τ and n . As the carrier density increases, electron-electron collisions become more frequent, decreasing τ . Other effects place more practical limits on the mobility, depending upon the nature of the material.

Typical TCOs feature a large band gap ($E_g > 3$ eV), such that thermal excitation of valence band electrons at room temperature ($kT \approx 0.03$ eV) is negligible. Therefore, perfectly crystalline stoichiometric TCOs behave as insulators. The conducting nature of these materials is due to the presence of defects in the metal oxide lattice, and a number of models exist to describe both the population of the conduction electrons and their mobility.^[4,5]

In the case of intrinsic materials, these defects are generally attributed to the presence of interstitial metal atoms or oxygen vacancies. These behave as electron donor centers, producing populated defect states shallow enough that thermal effects can excite these electrons into the conduction band.

For example in tin oxide, the multivalent nature of tin leads to local non-stoichiometry, such as interstitial Sn and O vacancies. These donor centers dominate the defect structure of SnO₂, turning an otherwise insulating material into an intrinsic n-type semiconductor. The role of these defects in the generation of charge

1.2 Electrical Conductivity of TCO

carriers has been conclusively supported by first-principle calculations .^[6]

Extrinsic dopants also play an important role in the population of the conduction band and their intentional introduction provides a useful handle for controlling the density of charge carriers. However, unintentional dopants also play a role. It has been conjectured for example that in the case of ZnO, the presence of interstitial hydrogen might be responsible for the population of conduction-band electrons.^[7]

High conductivity is typically desirable in TCO applications, and it may seem a simple way to increase the conductivity might be to increase the density of conduction electrons by introducing more dopant atoms. However, there is a limit to how long this can be continued.^[4,5]

At high carrier densities (above 10^{20} cm^{-3}), charge transport is dominated by ionised impurity scattering - that is, scattering via Coulomb interactions between the conduction electrons and the dopant sites. As more and more dopant is introduced, increased scattering reduces the carrier mobility (and has a detrimental effect on the optical properties), resulting in diminishing returns. Further doping can ultimately lead to non-homogeneous clustering of the dopant atoms, which significantly increases scattering) and eventually a limit is reached.

For example, in ITO films, the limiting carrier density was found^[8] to be approximately $1.5 \times 10^{21} \text{ cm}^{-3}$. ZnO films also exhibit similar behaviour. Here the measured resistivity and carrier mobility are limited to $2 \times 10^{-4} \text{ } \Omega \cdot \text{cm}$ and $50 \text{ cm}^2/\text{V} \cdot \text{s}$, respectively^[9,10], independent of deposition technique.

Other scattering mechanisms have similar effects on the charge mobility, and to varying extents this phenomenon is a universal limitation of all semiconductors. All TCO materials, doped and undoped, suffer the same limits, and only the absolute best samples have a resistivity below $1 \times 10^{-4} \text{ } \Omega \cdot \text{cm}$.

1.3 Optical properties of TCO

Light being an electromagnetic phenomenon, the optical properties of TCO materials are intimately coupled to the electrical properties as well.^[1,4] The interaction of light and materials can be described by the oscillatory motion of electrons bound to the atomic lattice. These electrons undergo harmonic motion in response to the time-varying electric field of the radiation:

$$\frac{md^2x}{dt^2} = \frac{-n_e e^2 x}{\varepsilon} \quad (1.3)$$

Here ε is the dielectric constant of the material, n_e the electron density, and e the electric charge. The solution to this oscillatory equation of motion has a resonance at the so-called the plasma frequency, ω_p :

$$\omega_p = \sqrt{\frac{n_e e^2}{m\varepsilon}} \quad (1.4)$$

Free electrons also follow this behavior, with the addition of a damping term that represents collisions with the atomic lattice. The rate of these collisions depends on τ , and on the carrier density, so the plasma frequency can be written in terms of the conductivity:

$$\omega_p^2 = \frac{\sigma_e^0}{\varepsilon\tau} = \frac{n_e e \mu_e}{\varepsilon\tau} \quad (1.5)$$

Light at the plasma frequency impinging upon the material undergoes strong resonant absorption, but above ω_p , the inertial mass of the electrons cannot be overcome, so the material becomes transparent. The refractive index is then a complex, frequency-dependent quantity:

$$\langle n \rangle^2 = (n + i\kappa)^2 = \frac{\varepsilon_L}{\varepsilon_o} - \frac{i\sigma}{\omega\varepsilon_o} \quad (1.6)$$

1.3 Optical properties of TCO

The imaginary component κ is called the extinction coefficient, which describes the resonant optical absorption and is related to the absorption coefficient

$$\alpha = \frac{4\pi\kappa}{\lambda} \quad (1.7)$$

At still higher frequencies, the photon energy is sufficient to excite valence electrons into the conduction band, yet a different absorption mechanism. This narrow window, above the resonant absorption frequency but below the band gap, spans the visible region of the spectrum for TCO materials.

When deposited as a thin film, other considerations must also be included to understand the materials optical properties.^[5] Specular reflections at the film-air and substrate-film interfaces reduce the transmission, such that the minimum transmission achievable (neglecting absorption) is

$$T_{min} = \frac{4n^2n_{sub}}{(1+n^2)(n^2+n_{sub}^2)} \quad (1.8)$$

For a typical TCO film ($n = 1.8 - 2.8$), deposited on a glass or silica substrate ($n_{sub} = 1.4-1.6$), the minimum transmission coefficient is then only 0.5 to 0.8. Interference effects for films with thickness greater than 100 nm, surface roughness and so on also play a role in diminishing the transparency.

As the relationship described above indicates, the electrical and optical properties of the film are linked, as increased conductivity shifts the resonant absorption edge and tends to shrink the transmission window. So, a useful metric to quantify the performance of a TCO film is in terms of the ratio of conductivity to absorption coefficient:

$$\frac{\sigma}{\alpha} = \frac{1}{R_s \ln(T+R)} \quad (1.9)$$

This wavelength-dependent quantity provides a useful handle to characterise

and assess the relative strengths of different TCO materials and their deposition techniques.

Based on the previous discussions, it can be suggested that the figure of merit can be improved via two routes. First way is improving the electrical properties, i.e. the mobility of TCO materials without compromising the transparency. Second way is to improve the optical properties, i.e. higher transmittance, without decreasing the conductivity. This has been the main effort in this field of research as well as the industry, although much more efforts were given by using the first approach.

1.4 Conventional TCO Materials

The literature reveals an enormous number of TCO systems fabricated from a variety of oxides, ranging from simple binary compounds to complex multicomponent mixtures. However, nearly all transparent electrodes developed to date contain at least one of indium, tin, zinc and cadmium^[2]. However, Cd-based systems are of limited practical use due to cadmium's high toxicity. Based on this factor alone, the field of TCO has been considered to narrow down to mainly In_2O_3 , SnO_2 , and ZnO based systems (**Fig1.1**).

The indium-tin axis has been extensively documented as mentioned earlier in this chapter, and provides a valuable benchmark system by which performance can be measured.

TCO films made of multi-component oxides have been closely examined in the recent years.

Minami et al have investigated multicomponent oxides based on three main oxides, In_2O_3 , SnO_2 , and ZnO , using MSP technique.^[11-13] It was found that the multicomponent materials contained the properties of both oxide materials. Furthermore, it was possible to estimate the properties of multicomponent oxides based

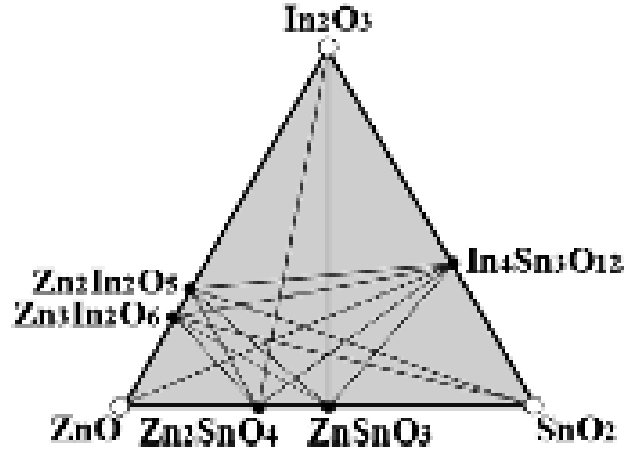


Figure 1.1: Practical TCO semiconductors for thin-film transparent electrodes.^[2]

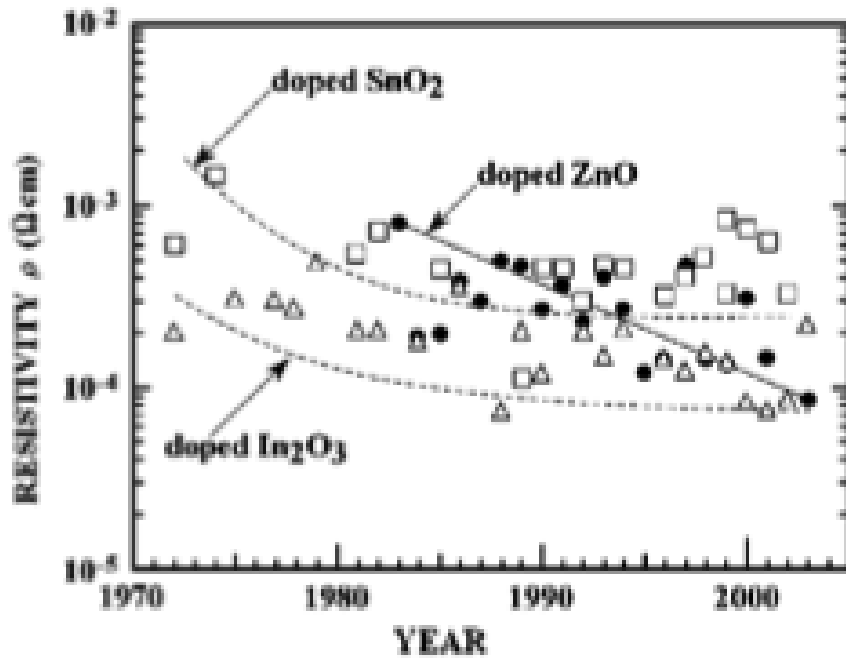


Figure 1.2: Reported resistivity of impurity doped binary TCO films over the past 30 years. Impurity-doped SnO_2 (\square), In_2O_3 (\triangle), and ZnO (\bullet)^[2]

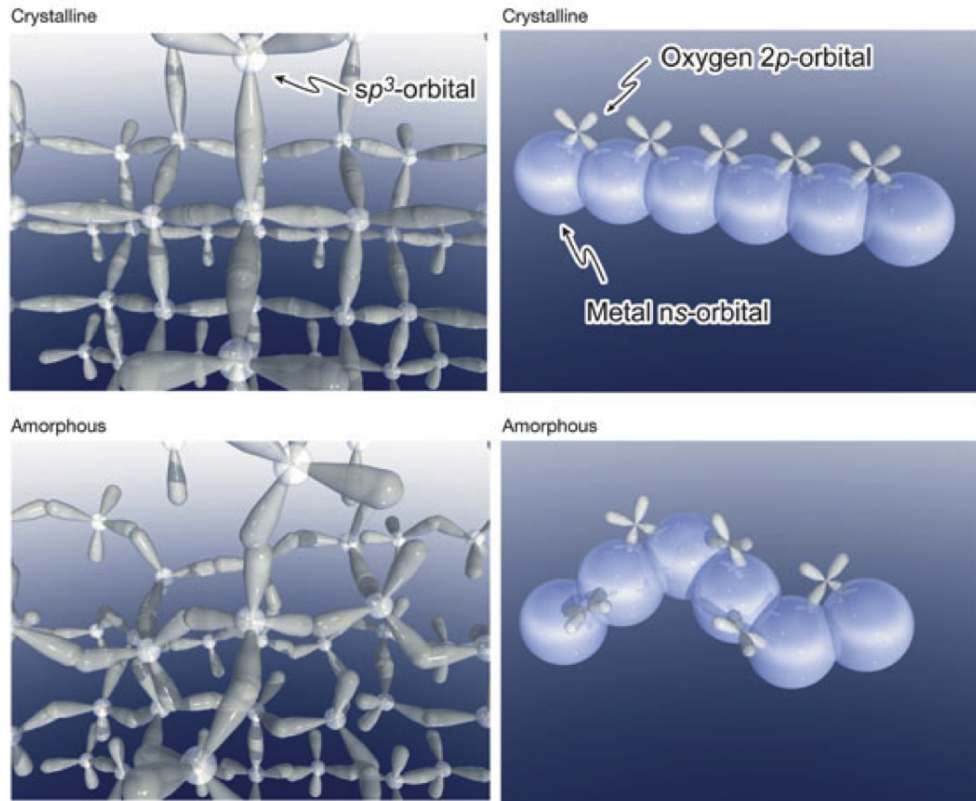
on the properties of the constituent oxide materials. The chemical properties such as etching rate depended on the type and the composition of the metal elements in the film.^[14]

1.5 Amorphous TCO

In the recent years, transparent amorphous oxides (TAO) have been introduced and presented as a promising alternative material to the aforementioned conventional transparent (semi)conducting oxides (TCO).^[15,16] In 2004, thin films of IGZO has been demonstrated as a superior replacement material for a-Si:H in the reports by Hosono et al.^[15] It was suggested that in amorphous post transition metal oxides such as IGZO, conduction can happen via metal s orbital instead of covalent bonds because the spatial spread of metal s-orbital is large enough to directly overlap with the neighbouring metal cation. In **Fig1.3**, the conduction mechanism is visualised through orbital drawings of Si and a post transition metal (PTM), and the PTM elements which can utilise this conduction mechanism are also indicated. From the illustration, it can be clearly understood that the electron mobility is drastically decreased in the a-Si compared to that of c-Si, whereas in the a-PTM still retains moderate level of mobility.

The conduction in PTM oxides resemble that of amorphous metal alloys in that the overlap of metal orbitals contributes to the main electron pathway.^[16] As shown in **Fig1.4**, the conductivity is lower for the amorphous alloys, as is the case for PTM oxides. However, a-TCOs over the conventional c-TCOs are favourable in terms of uniformity of thin film characteristics, absence of grain boundaries, which could cause unwanted brittleness and scattering, as well as processing temperature. Such characteristics not only improve the current electronic applications but also can serve as a platform for new device technologies such as flexible electronics.

1.5 Amorphous TCO



Group →	1	2	3	4	5	6	7	8	9	10	11	12	13	14	15	16	17	18		
↓ Period																				
1	1 H																	2 He		
2	3 Li	4 Be											5 B	6 C	7 N	8 O	9 F	10 Ne		
3	11 Na	12 Mg											13 Al	14 Si	15 P	16 S	17 Cl	18 Ar		
4	19 K	20 Ca	21 Sc	22 Ti	23 V	24 Cr	25 Mn	26 Fe	27 Co	28 Ni	29 Cu	30 Zn	31 Ga	32 Ge	33 As	34 Se	35 Br	36 Kr		
5	37 Rb	38 Sr	39 Y	40 Zr	41 Nb	42 Mo	43 Tc	44 Ru	45 Rh	46 Pd	47 Ag	48 Cd	49 In	50 Sn	51 Sb	52 Te	53 I	54 Xe		
6	55 Cs	56 Ba		72 Hf	73 Ta	74 W	75 Re	76 Os	77 Ir	78 Pt	79 Au	80 Hg	81 Tl	82 Pb	83 Bi	84 Po	85 At	86 Rn		
7	87 Fr	88 Ra		104 Rf	105 Db	106 Sg	107 Bh	108 Hs	109 Mt	110 Ds	111 Rg	112 Cn	113 Uut	114 Uuq	115 Uup	116 Uuh	117 Uus	118 Uuo		
				Lanthanides		57 La	58 Ce	59 Pr	60 Nd	61 Pm	62 Sm	63 Eu	64 Gd	65 Tb	66 Dy	67 Ho	68 Er	69 Tm	70 Yb	71 Lu
				Actinides		89 Ac	90 Th	91 Pa	92 U	93 Np	94 Pu	95 Am	96 Cm	97 Bk	98 Cf	99 Es	100 Fm	101 Md	102 No	103 Lr

Figure 1.3: Visualisation of conduction mechanism in covalently bonded crystalline Si (top) and amorphous TCO (bottom), and the elements indicated from the periodic table which are able to form amorphous TCO

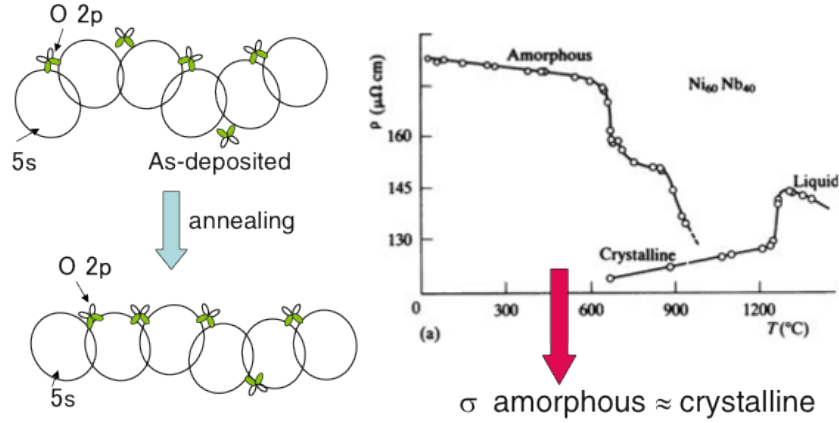


Figure 1.4: Similarity between ionic oxides and metals. (Left) Expected change in wavefunctions at conduction band minimum (CBM) of ionic amorphous oxide semiconductors with annealing.^[15] (Right) Comparison of resistivity among liquid, amorphous, and crystalline metals. The electron mobility is expected to be enhanced by annealing as in the case of a-metals.^[17]

Vast interests in this materials were indicated by the recent studies an effective thin film deposition method, compositional studies, and improving the properties of amorphous ternary oxides such as InZnO (IZO), InGaZnO(IGZO), and ZnSnO(ZTO).^[18-21] These films were deposited mainly via physical vapour deposition methods such as magnetron sputtering or pulse laser deposition (PLD), as they are currently the methods conventionally used for thin film TCO deposition.

The solution processing method for a-TCO thin films is more economical compared to the conventional physical vapour deposition methods. More importantly, unlike the isotropic nature of the PVDs, this method opens up the possibility of fabrication of 3D structured aTCO materials. Only recently, Banger et al.^[22] successfully fabricated thin films of I(G)ZO by solution processing methods using metal alkoxides as sol gel precursors which for the first time lead to stable, high-performing TFT devices.

1.6 Nanostructured TCOs

The current trends in TCO research seeks to introduce additional properties to the TCO materials on top of the conventional optical and electrical properties exhibited in their thin film form. The main important properties include controllable work function, reflectivity, lengthscale of the TCO structure. Being able to process TCOs into nanostructure is particularly important because it means that we can design novel heterostructures catered to the nano-scale diffusion lengths of the excitons, carriers, and chemical diffusion within the device. This can lead to new device designs of organic light emitting diodes (OLEDs), fuel cells, displays and solar cells. Moreover, the ability to incorporate other various functional materials to form a hybrid with the nanostructured TCO allows possibilities to sensors and other active devices in biological fields.^[23]

Efforts to realise 3D nanostructures of TCO have recently started. Mesoporous ITO^[24-26] and Sb:SnO₂^[27] have been fabricated using block-copolymer as a structural guiding agent resulting in 10-50nm pore sized nanostructures. Such advances can be complemented by increased number of studies on effective and tunable doping and conductivity of TCO materials, further development of amorphous TCO materials.

Nanostructured TCO for building applications

Nano-structured TCOs can be utilised in applications in functional coating of buildings- both on the outside and inside, which can be efficient use of their surface area. Numerous patents^[28-32] and limited publications already exist on coating of multi-functional films on buildings and windows surface^[33-35] The functionalities of coating can include photocatalytic, superhydrophobic, electrochromic, tunable optical and electrical properties, which can contribute to energy harvesting, air purifying (in-

doors), reducing of cleaning loads, and so on. Therefore, nanostructured TCOs has potentials for high impact applications for multifunctional buildings and windows.

As a good example of the concept, such potential has already been demonstrated through superhydrophobic windows using sputtered TiO_2 (anatase) films, which are both superhydrophilic (contact angle of zero) and photocatalytic.^[23] These coatings have been enthusiastically endorsed in Japan and Europe, and numerous patents and a few review articles on this topics are available. This technology was also employed for applications such as self-cleaning windows, anti-soiling coatings, anti-static coatings, etc. for both fabric and windows.^[36-41]

However, ZnO and SnO_2 based films not only possess many of aforementioned properties, but also are more conducting compared to TiO_2 . This can add another important variable for the functional coating applications. In the recent years, the efforts to dope TiO_2 with Nb or Ta, in order to increase its conductivity, have indeed been started, indicating the interest in this avenue of research.^[42,43]

Nanostructured TCO for Organic Solar Cells applications

Organic photovoltaics carries tremendous potentials in the field of photovoltaics technology due to their comparable theoretical efficiency to conventional semiconductor devices^[44] yet a much more economical cost structure^[45] viable for large-scale production. In addition, the processing techniques (solution processing) involved in this technology easily allows a large scaled production.^[46]

In a standard bulk heterojunction device, a donor and acceptor materials (both polymers) are blended, which results in a large interfacial area between them. As long as the blends are intimately mixed in 10nm lengthscale, which is shorter than the diffusion lengths for excitons in the acceptor material, efficient exciton dissociation can take place leading to charge generation. An example of heterojunction device can be poly[3-hexylthiophene](P3HT)/C61-butyric acid methyl ester (PCBM)

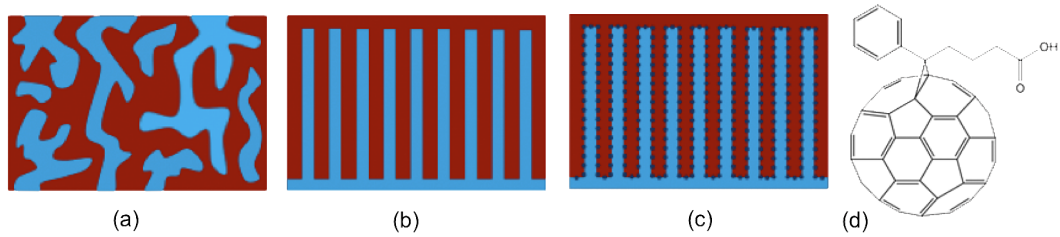


Figure 1.5: Schematic illustrations of organic solar cells (a) Bulk Heterojunction architecture (e.g. P3HT/PCBM) (b) Polymer/Metal Oxide hybrid device (e.g. P3HT/ZnO) (c) Polymer/Metal Oxide hybrid device (e.g. P3HT/ZnO) with SAM modification. The black dots indicate the SAM. e.g. PCBA (d) A type of SAM called Phenyl-C61-butyric acid (PCBA) Modified from reference^[47]

based device where P3HT is the donor and PCBM is the acceptor. The schematics of the bulk heterojunction is illustrated in **Fig1.5a**.

Due to their high optical absorption coefficients, only a few hundreds of nanometers of polymer film is required for these devices. Excitons generated by photoexcitation must be dissociated into charge carriers and then collected at the cathode and anode. Here, it is crucial to provide a continuous percolation pathway of both acceptor and donor for the charges to reach the electrodes. Otherwise, the charges can be trapped or need to hop through the unconnected network of donors/acceptors. This also effectively limits the thickness of the device to $\sim 300\text{nm}$, consequently limiting the efficiency due to limited amount of light absorbed.^[48,49]

Therefore, the morphology and the interface of the polymer blend is crucial for solar cell performance. However, controlling the morphology of the blend can be limited because it relies on phase separation and change of temperature of the surroundings can lead to unwanted morphological transitions. A device architecture that provides direct and ordered paths for photogenerated carriers to the collecting electrodes can resolve many of the transport issues of bulk heterojunction photovoltaic devices.

Metal oxides such as SnO_2 , TiO_2 and ZnO are able to act as a replacing ac-

ceptor material to the polymer acceptor.^[50,51] Building a device by incorporation of conjugated polymer into a rigid nanoporous metal oxide active layer^[52–54] offers a key advantage of improved structural control of the inorganic material. For example P3HT/ZnO nanowires devices have attracted a great interest due to its ease of fabrication and low temperature processing conditions.^[55,56] The schematics of this type of device architecture, called inverted hybrid architecture is shown in **Fig1.5b**.

Due to their much improved thermal stability, the mesoporous metal oxides provide structural stability. In addition, the metal oxide active layer can be first prepared before incorporating the polymeric donor material. This allows chemical/physical treatments which can be damaging to polymers, to realise a well defined nanostructure with continuous transport pathways.

Having good control over the donor/acceptor morphology is a promising way to optimise charge transport through connected pathways while maintaining efficient exciton dissociation in the composite. Using the inverted hybrid architecture also can exploit the superior electron mobility of metal oxides to those of organic semiconductors (by several orders of magnitude), which creates more efficient electron pathways for charge collection.

Two crucial factors for further improving device performance include optimising exciton dissociation into free carriers at the polymer/oxide interface and minimising recombination losses. To address these issues, molecular surface modification using a self-assembled monolayer(SAM) can be employed for the energy level alignment^[57,58], which has demonstrated to improve charge collection efficiency.^[59,60] For example, recently a ZnO/P3HT device with PCBA(a type of SAM) surface modification demonstrated enhanced solar cell performance.

Bibliography

- [1] Exarhos, G.J. and Zhou, X.D. (2007) Discovery-based design of transparent conducting oxide films. *Thin Solid Films*, **515** (18), 7025–7052, doi:10.1016/j.tsf.2007.03.014. [1](#), [2](#), [5](#)
- [2] Minami, T. (2005) Transparent conducting oxide semiconductors for transparent electrodes. *Semiconductor Science and Technology*, **20** (4), S35. [1](#), [7](#), [8](#)
- [3] Jiang, X., Wong, F., Fung, M., and Lee, S. (2003) Aluminum-doped zinc oxide films as transparent conductive electrode for organic light-emitting devices. *Applied Physics Letters*, **83** (9), 1875–1877. [2](#)
- [4] Coutts, T.J., Young, D.L., and Gessert, T.A. (2010) Modeling, characterization, and properties of transparent conducting oxides, in *Handbook of Transparent Conductors* (ed. D.S. Ginley), Springer US, pp. 51–110. [2](#), [3](#), [4](#), [5](#)
- [5] Castañeda, L. (2011) Present status of the development and application of transparent conductors oxide thin solid films. *MSA*, **02** (09), 1233–1242, doi:10.4236/msa.2011.29167. [3](#), [4](#), [6](#)
- [6] Kılıç, Ç. and Zunger, A. (2002) Origins of coexistence of conductivity and transparency in SnO_2 . *Physical Review Letters*, **88** (9), 95501. [4](#)
- [7] Van de Walle, C. (2000) Hydrogen as a cause of doping in zinc oxide. *Physical Review Letters*, **85** (5), 1012–1015. [4](#)
- [8] Frank, G. and Köstlin, H. (1982) Electrical properties and defect model of tin-doped indium oxide layers. *Applied Physics A: Materials Science & Processing*, **27** (4), 197–206. [4](#)
- [9] Ellmer, K. (2000) Magnetron sputtering of transparent conductive zinc oxide: relation between the sputtering parameters and the electronic properties. *Journal of Physics D: Applied Physics*, **33** (4), R17. [4](#)
- [10] Ellmer, K. (2001) Resistivity of polycrystalline zinc oxide films: current status and physical limit. *Journal of Physics D: Applied Physics*, **34** (21), 3097. [4](#)

- [11] Minami, T. (2000) New n-type transparent conducting oxides. *Mrs Bulletin*, **25** (8), 38–44. [7](#)
- [12] Minami, T. (1999) Transparent and conductive multicomponent oxide films prepared by magnetron sputtering. *Journal of Vacuum Science & Technology A: Vacuum, Surfaces, and Films*, **17** (4), 1765–1772.
- [13] Ko, J., Kim, I., Kim, D., Lee, K., Lee, T., Cheong, B., and Kim, W. (2007) Transparent and conducting zn-sn-o thin films prepared by combinatorial approach. *Applied surface science*, **253** (18), 7398–7403. [7](#)
- [14] Phillips, J., Kwo, J., Thomas, G., Carter, S., Cava, R., Hou, S., Krajewski, J., Marshall, J., Peck, W., Rapkine, D. *et al.* (1994) Transparent conducting thin films of gaino; inf_i 3_i/inf_i. *Applied physics letters*, **65** (1), 115–117. [9](#)
- [15] Nomura, K., Ohta, H., Takagi, A., Kamiya, T., Hirano, M., and Hosono, H. (2004) Room-temperature fabrication of transparent flexible thin-film transistors using amorphous oxide semiconductors. *Nature*, **432** (7016), 488–492. [9](#), [11](#)
- [16] Hosono, H. (2010) Handbook of transparent conductors. *Transparent Amorphous Oxide Semiconductors for Flexible Electronics*, pp. 459–487, doi:10.1007/978-1-4419-1638-9_13. [9](#)
- [17] Elliott, S. (1990) *Physics of Amorphous Materials*, Wiley, New York, 2nd edn.. [11](#)
- [18] Galca, A., Socol, G., and Craciun, V. (2011) Optical properties of amorphous-like indium zinc oxide and indium gallium zinc oxide thin films. *Thin Solid Films*. [11](#)
- [19] Kim, T., Yoon, J., Ghong, T., Barange, N., Kim, J., Hwang, S., Kim, Y., Hwang, S., Choi, J., and Joo, J. (2011) Effect of the ga ratio on the dielectric function of solution-processed ingazno films. *Journal of the Korean Physical Society*, **59** (6), 3396–3400.
- [20] (2008) General mobility and carrier concentration relationship in transparent amorphous indium zinc oxide films. *Physical Review B*, **77** (11), 115215.
- [21] Barquinha, P., Pereira, L., Goncalves, G., Martins, R., and Fortunato, E. (2009) Toward high-performance amorphous gizo tfts. *Journal of the Electrochemical Society*, **156** (3), H161–H168. [11](#)
- [22] Banger, K.K., Yamashita, Y., Mori, K., Peterson, R.L., Leedham, T., Rickard, J., and Sirringhaus, H. (2010) Low-temperature, high-performance solution-processed metal oxide thin-film transistors formed by a ‘sol–gel on chip’ process. *Nat Mater*, **10** (1), 45–50, doi:10.1038/nmat2914. URL <http://dx.doi.org/10.1038/nmat2914>. [11](#)
- [23] Olson, D.C. and Ginley, D.S. (2010) Handbook of transparent conductors. *Nanostructured TCOs*, pp. 425–457, doi:10.1007/978-1-4419-1638-9_12. [12](#), [13](#)

-
- [24] Buonsanti, R., Pick, T., Krins, N., Richardson, T., Helms, B., and Milliron, D. (2012) Assembly of ligand-stripped nanocrystals into precisely controlled mesoporous architectures. *Nano Letters*, **12** (7), 3872–3877. [12](#)
- [25] Fattakhova-Rohlfing, D., Brezesinski, T., Rathouský, J., Feldhoff, A., Oekermann, T., Wark, M., and Smarsly, B. (2006) Transparent conducting films of indium tin oxide with 3d mesopore architecture. *Advanced Materials*, **18** (22), 2980–2983.
- [26] von Graberg, T., Hartmann, P., Rein, A., Gross, S., Seelandt, B., Röger, C., Zieba, R., Traut, A., Wark, M., Janek, J. *et al.* (2011) Mesoporous tin-doped indium oxide thin films: effect of mesostructure on electrical conductivity. *Science and Technology of Advanced Materials*, **12** (2), 025 005. [12](#)
- [27] Müller, V., Rasp, M., Rathouský, J., Schütz, B., Niederberger, M., and Fattakhova-Rohlfing, D. (2010) Transparent conducting films of antimony-doped tin oxide with uniform mesostructure assembled from preformed nanocrystals. *Small*, **6** (5), 633–637, doi:10.1002/smll.200901887. [12](#)
- [28] Chen, H. Zhou, Y. Application: Cn. cn patent no. 1009-955, 1888342 (20060705. 2007). [12](#)
- [29] Doi, K. Application: Jp. jp patent no. 98-234737, 2000073276 (19980820. 2000).
- [30] Fukuwatari, I. Mizuta, K. Application: Jp. jp patent no. 99-59670, 2000254043 (19990308. 2000).
- [31] Jonschker, G. Application: De. de patent no. 2001-10116198, 10116198 (20010330. 2002).
- [32] Kitamura, A. Hayakawa, M. Application: Jp. jp patent no. 97-31159, 10212139 (19970130. 1998). [12](#)
- [33] Arbab, M., Shelestak, L., and Harris, C. (2005) Value-added flat-glass products for the building, transportation markets, part 1. *American Ceramic Society Bulletin*, **84** (1), 30–35. [12](#)
- [34] Arbab, M., Shelestak, L., and Harris, C. (2005) Value-added flat-glass products for the building, transportation markets, part 2. *Am. Ceram. Soc. Bull.*, **84** (4), 34–8.
- [35] Sanderson, K., Mills, A., Hurst, S., Lepre, A., McKittrick, T., Rimmer, D., and Ye, L. (2003) Svc 46th annual technical conference proceedings. *Publishers: Society of Vacuum Coaters, Albuquerque, Nm, Usa*, pp. 203–208. [12](#)
- [36] Paz, Y., Luo, Z., Rabenberg, L., and Heller, A. (1995) Photooxidative self-cleaning transparent titanium dioxide films on glass. *Journal of Materials Research*, **10** (11), 2842–2848. [13](#)

- [37] Azzopardi, M.J. Application: Wo. wo patent no. 2003-fr1219, 2003087005 (20030416. 2003).
- [38] Harris, C.S., S.C..W.S. Application: Us. us patent no. 2005-85328, 2006210810 (20050321. 2006).
- [39] Kiribayashi, T., Y.N.K.T..M.T. Application: Jp. jp patent no. 2000-101093, 2001287970 (20000403. 2001).
- [40] Nakabayashi, A. Ota, K. Application: Jp. jp patent no. 2002-271882, 2004106348 (20020918. 2004).
- [41] Yoshimoto, T., A.S.N.T.S.E..A.O. Application: Jp. jp patent no. 98-18430, 11207871 (19980130. 1999). [13](#)
- [42] Hitosugi, T., Yamada, N., Nakao, S., Hirose, Y., and Hasegawa, T. (2010) Properties of tio₂-based transparent conducting oxides. *physica status solidi (a)*, **207** (7), 1529–1537. [13](#)
- [43] Khomutov, G., Kislov, V., Antipina, M., Gainutdinov, R., Gubin, S., Obydenov, A., Pavlov, S., Rakhnyanskaya, A., Sergeev-Cherenkov, A., Soldatov, E. *et al.* (2003) Interfacial nanofabrication strategies in development of new functional nanomaterials and planar supramolecular nanostructures for nanoelectronics and nanotechnology. *Microelectronic Engineering*, **69** (2), 373–383. [13](#)
- [44] Shockley, W. and Queisser, H. (1961) Detailed balance limit of efficiency of p-n junction solar cells. *Journal of Applied Physics*, **32** (3), 510–519. [13](#)
- [45] Shaheen, S., Ginley, D., and Jabbour, G. (2005) Organic-based photovoltaics: toward low-cost power generation. *MRS bull*, **30** (10). [13](#)
- [46] Shaheen, S., Radspinner, R., Peyghambarian, N., and Jabbour, G. (2001) Fabrication of bulk heterojunction plastic solar cells by screen printing. *Applied Physics Letters*, **79** (18), 2996–2998. [13](#)
- [47] Vaynzof, Y. *PhD Dissertation*. [14](#)
- [48] Shaheen, S., Brabec, C., Sariciftci, N., Padinger, F., Fromherz, T., and Hummelen, J. (2001) 2.5% efficient organic plastic solar cells. *Applied Physics Letters*, **78** (6), 841–843. [14](#)
- [49] Hoppe, H., Niggemann, M., Winder, C., Kraut, J., Hiesgen, R., Hinsch, A., Meissner, D., and Sariciftci, N. (2004) Nanoscale morphology of conjugated polymer/fullerene-based bulk-heterojunction solar cells. *Advanced Functional Materials*, **14** (10), 1005–1011. [14](#)

- [50] Anderson, N., Hao, E., Ai, X., Hastings, G., and Lian, T. (2001) Ultrafast and long-lived photoinduced charge separation in meh-ppv/nanoporous semiconductor thin film composites. *Chemical physics letters*, **347** (4), 304–310. [15](#)
- [51] Savenije, T., Warman, J., and Goossens, A. (1998) Visible light sensitisation of titanium dioxide using a phenylene vinylene polymer. *Chemical physics letters*, **287** (1), 148–153. [15](#)
- [52] Olson, D., Shaheen, S., Collins, R., and Ginley, D. (2007) The effect of atmosphere and zno morphology on the performance of hybrid poly (3-hexylthiophene)/zno nanofiber photovoltaic devices. *The Journal of Physical Chemistry C*, **111** (44), 16 670–16 678. [15](#)
- [53] Kroeze, J., Savenije, T., Vermeulen, M., and Warman, J. (2003) Contactless determination of the photoconductivity action spectrum, exciton diffusion length, and charge separation efficiency in polythiophene-sensitized tio2 bilayers. *The Journal of Physical Chemistry B*, **107** (31), 7696–7705.
- [54] Beek, W., Wienk, M., Kemerink, M., Yang, X., and Janssen, R. (2005) Hybrid zinc oxide conjugated polymer bulk heterojunction solar cells. *The Journal of Physical Chemistry B*, **109** (19), 9505–9516. [15](#)
- [55] Olson, D., Piris, J., Collins, R., Shaheen, S., and Ginley, D. (2006) Hybrid photovoltaic devices of polymer and zno nanofiber composites. *Thin Solid Films*, **496** (1), 26–29. [15](#)
- [56] Takanezawa, K., Hirota, K., Wei, Q., Tajima, K., and Hashimoto, K. (2007) Efficient charge collection with zno nanorod array in hybrid photovoltaic devices. *The Journal of Physical Chemistry C*, **111** (19), 7218–7223. [15](#)
- [57] Goh, C., Scully, S., and McGehee, M. (2007) Effects of molecular interface modification in hybrid organic-inorganic photovoltaic cells. *Journal of applied physics*, **101** (11), 114 503–114 503. [15](#)
- [58] Lin, Y., Lee, Y., Chang, L., Wu, J., and Chen, C. (2009) The influence of interface modifier on the performance of nanostructured zno/polymer hybrid solar cells. *Applied Physics Letters*, **94** (6), 063 308–063 308. [15](#)
- [59] Khodabakhsh, S., Sanderson, B., Nelson, J., and Jones, T. (2005) Using self-assembling dipole molecules to improve charge collection in molecular solar cells. *Advanced Functional Materials*, **16** (1), 95–100. [15](#)
- [60] Hau, S., Yip, H., Ma, H., and Jen, A. (2008) High performance ambient processed inverted polymer solar cells through interfacial modification with a fullerene self-assembled monolayer. *Applied Physics Letters*, **93** (23), 233 304–233 304. [15](#)

Chapter 2

Blockcopolymer Self Assembly and Its Use in Nanotechnology

2.1 Phase separation in block copolymers

2.1.1 Macrophase separation of Polymer Blends

Polymers are a class of organic compounds which are long chains composed of covalently linked repeated units called monomers. Homopolymer refers to a polymer which consists of one type of monomer whereas copolymers refer to those which have more than one monomer. Chemically different polymer chains in a melt are often immiscible and have a tendency to macrophase separate. The thermodynamics of polymer blends is described by Flory Huggins using mean free approach starting from Gibbs free energy equation which comprises two competing terms, each accounting for enthalpy and entropy.

$$\Delta G_{mix} = \Delta H_{mix} - T\Delta S_{mix} \quad (2.1)$$

The equation can be further described by using specific terms related to poly-

2.1 Phase separation in block copolymers

mers. The enthalpy of mixing is based on the enthalpy contributions from the interactions between neighbouring monomers, and thus is proportional to the number of monomers present. The entropy of mixing, on the other hand, favours homogeneous mixing and therefore is inversely proportional to the degree of polymerisation (N). Finally, the free energy of mixing per monomer (G_{mix}) for a blend of polymers A and B with degree of polymerization N at temperature T is given by:

$$\frac{\Delta G_{mix}}{k_B T} = \chi f_A f_B + \frac{f_A}{N_A} \ln f_A + \frac{f_B}{N_B} \ln f_B \quad (2.2)$$

where f_a and f_b correspond to the volume fraction of each polymer. The dimensionless parameter χ can be described as

$$\chi = \chi_{AB} = \frac{Z}{k_B T} (w_{AB} - \frac{1}{2}(w_{AA} + w_{BB})) \quad (2.3)$$

based on the classical theory of polymer-polymer interfaces where Z is the number of nearest-neighbour contacts, and the w are the mutual interaction energies per monomer. Therefore, unlike monomer blends where the mixing behaviour is governed by χ , polymer phase behaviour is governed by χ . A critical value of $\chi=2$ divides the case into homogeneous mixing ($\chi < 2$) or phase separation ($\chi \geq 2$). As the value of Z is usually a large number, only a small value of χ would lead to phase separation, and using the equation for the free energy (*Eq.2.2*), the phase diagram of the polymer blend can be derived.^[1]

2.1.2 Microphase Separation of BCP

Block copolymer, a subclass of copolymer, is made of nominally immiscible polymers that have been covalently bonded together in moderately-sized chains called blocks. Block copolymers constitute a class of polymer blends distinguished by the covalent linkage of heterogeneous monomer chains. A variety of distinct architectures are

2.1 Phase separation in block copolymers

possible, determined by the arrangement of the constituent homopolymers. These include diblock (A-b-B), triblock (A-b-B-b-A) and starblock copolymers. While homopolymer mixtures are known to phase separate into macroscopic domains, the covalent bonding of the heterogeneous blocks limits the BCP domain size. These domains typically have dimensions of 5 to 100 nanometers, constrained by the length of the distinct polymer chains.

In the Flory-Huggins formulation of polymer phase separation, minimisation of the Gibbs free energy is achieved by equilibrium between competing enthalpic (interfacial) and entropic (conformational) terms. The balance is between weak monomer-monomer repulsion, which tends to drive phase separation by minimising the interfacial area, and the elasticity of the polymer chains, which tends to resist conformational changes. Similar to that of homopolymer blends, there exists a critical value of χ where a homogeneous melt of copolymer chains transitions into the chemically heterogeneous ordered microdomains occurs. This is known as the order-disorder transition (ODT). The term χ indicates how immiscible the two blocks are, which plays an important role in the phase separation kinetics.

The resulting morphology from microphase separation and the ODT temperature are governed by the volume fractions of the blocks, f_A and $f_B (=1- f_A)$. Based on the extent to which the blocks like to segregate due to incompatibility, the block segregation can be divided to three regimes: weak ($\chi \sim 10$), intermediate ($\chi \sim 10?100$) and strong ($\chi \geq 100$). In the weak segregation regime, the entropic terms dominate leading to a disordered state, whereas as χ becomes ≥ 10 , enthalpic terms start to dominate resulting in an order-to-disorder transition (ODT), where the unlike segments segregate into a variety of ordered periodic microstructures. Application of the unified mean-field theory^[2] allows calculation of full phase diagrams in terms of volume fraction and molecular weight of BCP(**Fig.2.1 a**) which are in good agreement with experimental measurements of BCP model systems such

2.1 Phase separation in block copolymers

as poly(isoprene-*b*-styrene) by Khandpur et al.^[3](**Fig.2.1 b**,) It is worth mentioning that the strong dependence of χ on temperature (inversely proportional) allows inducing morphology transitions by varying the temperature of the system, in practice. A phase diagram of a diblock copolymer, plotted with respect to χ and f_A , is

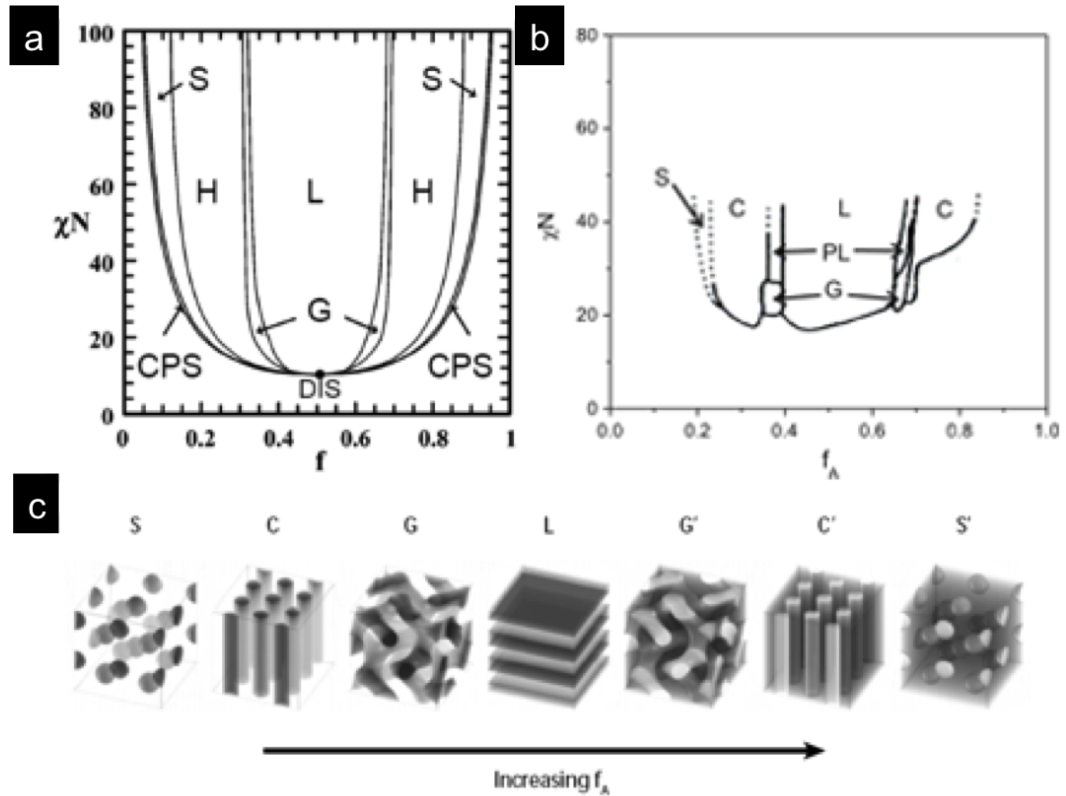


Figure 2.1: (a) A phase diagram of diblock copolymer plotted with respect to χ and f_A .^[4] (b) Experimentally measured phase diagram of PS-*b*-PI^[5] (c) Visualisation of the phases labeled in the phase diagrams in (a) and (b).

shown in **Fig. 2.2**. The planar interface of the lamellar structure is enforced by the enthalpic energy cost associated with a curved surface. Shifting the BCP volume fraction away from the $f_A = f_B$ symmetry imposes an energy cost associated with retaining the flat lamellar structure. Eventually, curvature of the interface towards the smaller block leads to a net decrease in free energy, and the system undergoes a

phase change, shifting from lamellae to a bicontinuous gyroid morphology. As the ratio of volume fractions is driven even further away from 1, other phase transitions appear. The gyroid morphology is followed by a shift to cylindrical domains arranged in a hexagonal lattice, spherical domains in a body-centred cubic lattice, close-packed spheres, and finally at the extremes of relative composition, a fully disordered structure. Other long-lived phases have also been experimentally observed, such as perforated lamellae and double diamond structures. These morphologies are metastable, but represent non-equilibrium polymer systems.^[3] Extending this notion to include triblock copolymer systems leads to an even wider variety of structures, with more than a dozen equilibrium morphologies exhibited on a ternary phase diagram.^[5-7]

2.1.3 The Gyroid (G) Phase

The gyroid phase was first correctly identified in block copolymer in 1994 by Hajduk et al and Schulz et al independently.^[? ?] Precisely speaking, the morphology of gyroid phase is a double gyroid, which comprises a minority block segregated into a network of two intertwined yet separately running channels, referred as a bicontinuous network, surrounded by a matrix of majority phase occupying $\sim 65\%$ of space. A unit cell of double gyroid morphology, as shown in **Fig2.2**, has a cubic symmetry (Ia3d). Gyroid phase only corresponds to a narrow area in the phase diagram and thus is difficult to experimentally realise. Synthesising a gyroid-forming block copolymer, thereby fixing volume fractions of the blocks, limits the chances of reaching gyroid phase. Therefore, although possible, this route is too delicate and costly to realise. Alternate experimental approach to gyroid phase is to use homopolymer(hA)/BCP(cAB) blends where the homopolymer A becomes incorporated into block A of the copolymer (cA), forming a newly formed, two-phase-system (A'B) with altered volume fractions. However, this method also entails complex and

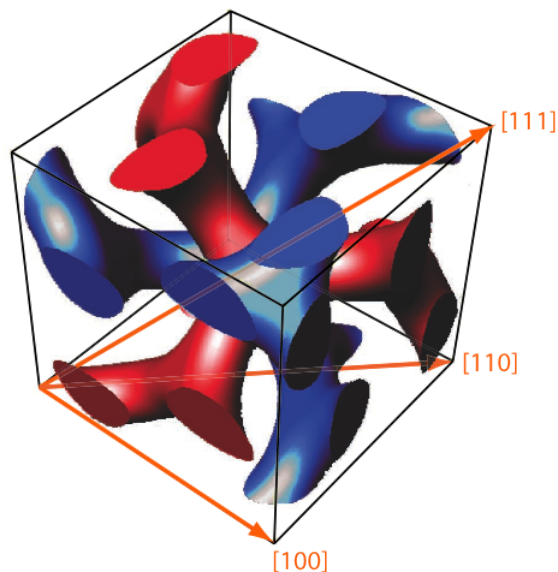


Figure 2.2: A unit cell of gyroid morphology. This diagram only shows the bicontinuous network which is formed by the minority phase with the matrix (majority phase) removed. (Modified from reference^[9])

delicate kinetics, which is an interplay between the microphase separation of the diblock copolymer and the macrophase separation of the homopolymer. Studies on the phase behaviour of various hP/BCP binary blends are available in literature^[10-13]

The chain length of hA in comparison to that of cA was found to be a deciding factor for solubilisation of hA into the cA micro domain.^[14,15] The phase separation behaviours with respect to N_{hA} relative to N_{cA} can be visualised as shown in **Fig2.3**. When $N_{hA} < N_{cA}$, the chains of hA can be uniformly incorporated into cA, leading to increase of the domain size as well as the interfacial area between hA/cA and cB. (**Fig2.3 a**). Such increase in interfacial area leads to morphology transition. However, when the chain length of hA and cA are comparable ($N_{hA} \sim N_{cA}$), the chemical compatibility allows them to assemble into the same region, but incorporation of hA into cA resulting in separate localisation of hA. In this case, selective swelling of cA

2.1 Phase separation in block copolymers

fails to occur, thus neither does morphology transition. (Fig2.3 b) Finally, when $N_{hA} > N_{cA}$, the repulsive forces between cA and hA becomes significant, which leads to macrophage separation of hA from the BCP. (Fig2.3 c)^[10]

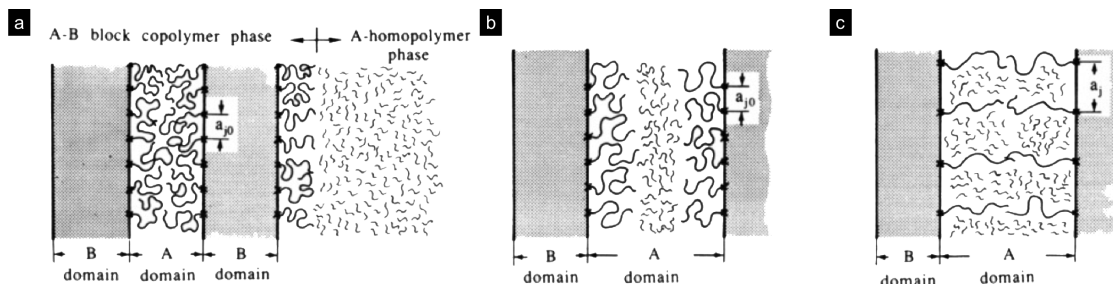


Figure 2.3: Visualisation of possible resulting structures of hA/BCP (AB) blend according to N_{hA} relative to N_{cA} . (a) $N_{hA} > N_{cA}$ Macrophase separation between hA and BCP (AB). The BCP micro phase separates on its own. (b) $N_{hA} < N_{cA}$: A homopolymer is locally solubilized in the middle of A microdomains; (c) $N_{hA} < N_{cA}$: Uniform solubilisation of hA into cA the uniform microdomain structure composed of A-B and A^[10]

The phase behaviour studies on blends using polystyrene have been reported by Winey et al.^[13,16] where resulting morphologies of the blended-BCP like structure were studied with respect to N_{hA} and overall concentration of homopolymer. Such results were summarised in constant copolymer composition diagrams, one of which is shown in Fig2.4 . In addition, it was discovered that use of lamellar forming BCP in a blend is more favourable compared to using a cylinder forming BCP. The former system exhibited a larger window of gyroid phase in the constant copolymer composition diagram, and was found to incorporate the homopolymer without macrophage separation.

2.2 Application of Blockcopolymer Patterning in Nanotechnology

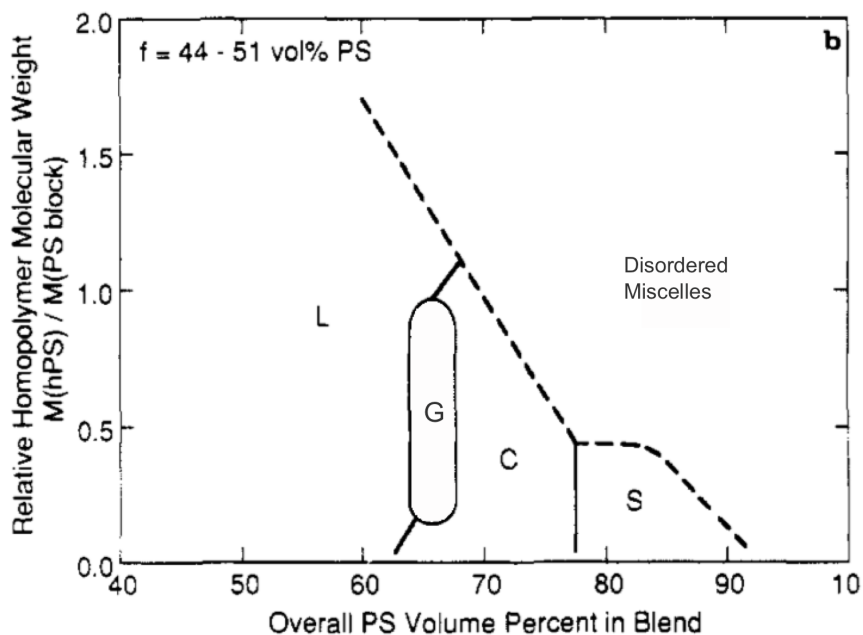


Figure 2.4: Constant copolymer composition morphology diagram of homopolystyrene blended with lamellar diblock copolymers of $f_{PS} = 44-51$ vol % polystyrene. (Modified from Winey et al.^[16])

2.2 Application of Blockcopolymer Patterning in Nanotechnology

The major challenge in the application of BCP materials is that most of the polymer systems in wide use polystyrene (PS), polyisoprene (PI), polyethylene oxide (PEG), polymethyl methacrylate (PMMA) or polylactic acid (PLA) lack the useful chemical or electrical properties needed in functional devices. Active conjugated polymers are typically brittle, and their low molecular weight poses a significant obstacle to their use as microphase-separated block copolymer.

Alternatively, self-assembled BCP materials can also be used in creating a mesoporous functional material, which hold great promise in application to a variety

2.2 Application of Blockcopolymer Patterning in Nanotechnology

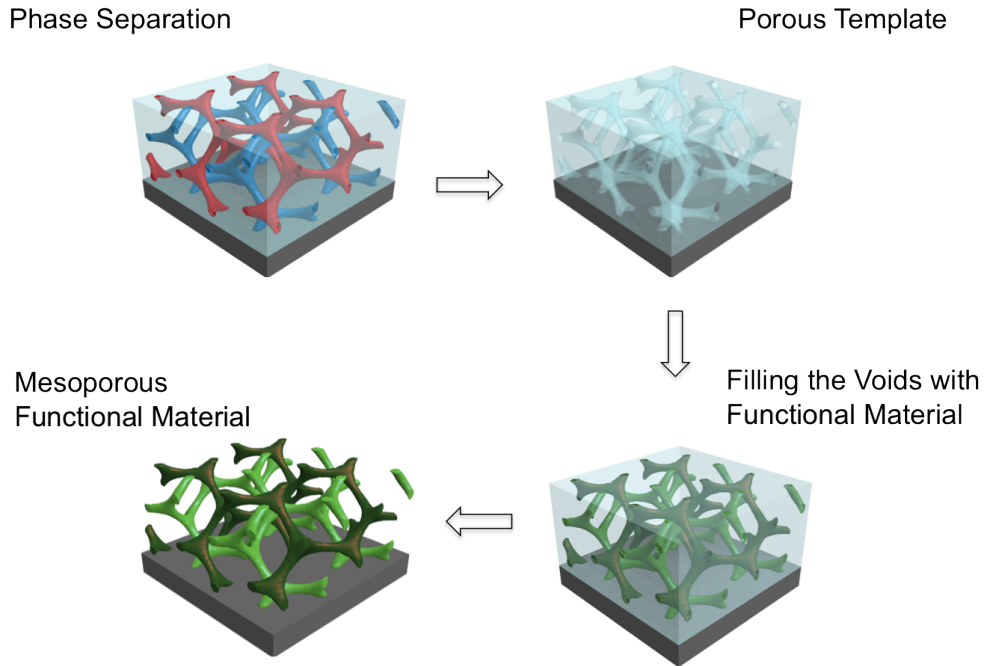


Figure 2.5: Fabrication of functional material using sacrificial polymeric template obtained by BCP self-assembly

of technologies from photonics to biotechnology. For example, many electronic devices such as super capacitors, fuel cells, photovoltaics and so on, are limited by surface charge- or reactant-transport phenomena. The nanometer-scale structures formed by typical BCP systems have large relative surface areas, and their use in controlling the structure of these devices can lead to significant improvements in efficiency. Block copolymer-derived patterning of inorganic materials has been a popular method for creating mesoporous metal oxides such as aluminosilicates, WO_3 , TiO_2 , V_2O_5 for applications in photocatalysis^[17,18], super capacitor^[19], electrochromism^[19?], and photovoltaics^[20]. Fabrication of such mesoporous functional materials using BCP phase separation can be realised via two routes- 1) by utilising them as a sacrificial template and 2) by co-assembling the functional material with a BCP, which plays a role of structure guiding agent. The first approach can be

2.2 Application of Blockcopolymer Patterning in Nanotechnology

visualised as shown in **Fig.2.5**. The functional inorganic material of choice can fill the voids created by removing the minority phase of the self assembled BCP via various infiltration methods such as solution impregnation^[18], electrodeposition^[19? ,20], atomic layer deposition.^[21] Upon selective removal of the polymer template, the remaining inorganic material retains the morphology realised by BCP self-assembly. The second approach is the BCP-directed co-assembly method, which provides a

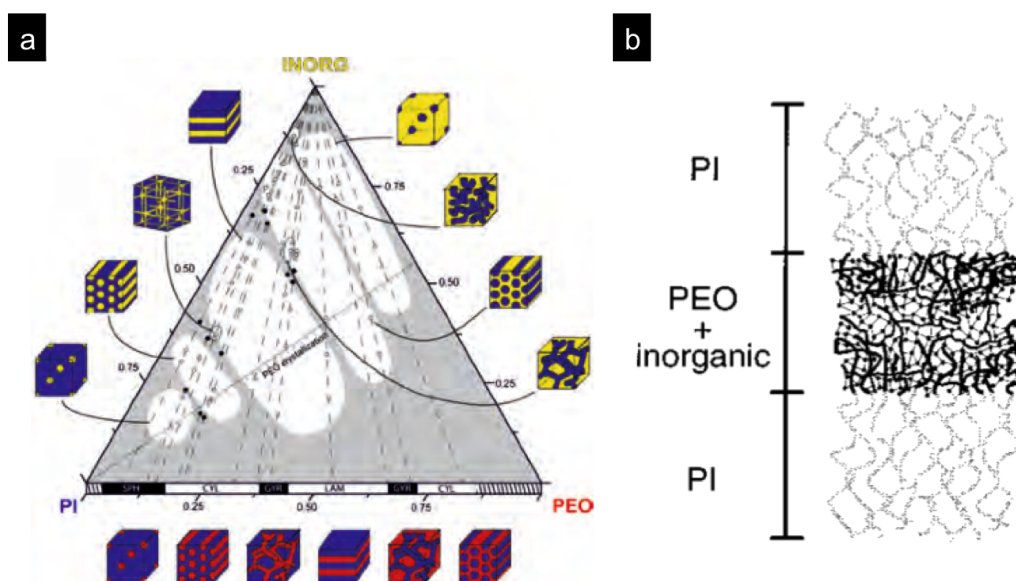


Figure 2.6: (a) Phase diagram obtained by aluminosilicate/PI-b-PEO co-assembly. The aluminosilicate is labels as INORG in the diagram^[22](b) Illustration of micro phase separation upon successful incorporation of aluminosilicate into the PEO block^[23]

more direct route to fabrication of mesoporous inorganic materials. Essentially, BCP acts as a structure directing material, just like other organic surfactants such as PEG.^[24,25] The inorganic precursors have higher affinity to the hydrophilic ends of the surfactant, and, following the polymer self-assembly process, are incorporated as part of the hydrophilic block of the self assembled BCP. Once the surfactant is removed by plasma etching or high temperature calcination, voids within the inorganic

2.2 Application of Blockcopolymer Patterning in Nanotechnology

structure remain, resulting in a porous inorganic structure.

The inorganic-BCP system is analogous to the selective incorporation of homopolymer into a BCP block discussed in the previous section. In principle, the hydrophilicity of metal oxide sol particles can fully mix with the hydrophilic block^[23] (**Fig.2.6 a**) resulting in a BCP-like system with an increased volume fraction of the hydrophilic component. Similarly to the effect of relative molecular weight homopolymer on the phase behaviour of the polymer blend, the size of inorganic particles in comparison to the chain length of the polymer block plays an important role. Therefore, in order to fully incorporate the inorganic particles into the BCP microdomain, their size in comparison to the polymer chain length of the incorporating block has to be significantly small.^[26] In the case of metal oxides, the inorganic particles can be prepared via sol-gel method or synthesis of nano crystals.^[27,28]

However, incorporation of inorganic material into BCP also means combining of two different systems- chemical synthesis of metal oxides and phase separation of block copolymer. Therefore, this system entails additional complexity and requirements compared to the binary polymer blend system. Here, it is important for the inorganic particle to have selective affinity, via intermolecular forces, to only one of the block of the BCP.^[29] Additionally, the kinetics of micro phase separation must be faster than gelation (or aggregation) kinetics of inorganic particles.^[30] Therefore, using a BCP with a sufficiently large χ is preferable, and the inorganic particles must be relatively stable. Finally, a solvent dissolving all of the components (the polymer blocks and the inorganic) equally well is required in order to ensure that the solvent is uniformly evaporated throughout the components.

Successful co-assembly can lead to various morphologies by tuning of the inorganic component as well as the volume ratio of the BCP. For example, in the study of De Paul et al.^[23], employing aluminosilicate/PI-b-PEO, a phase diagram of quasi-binary, BCP-like system was prepared as shown in **Fig.2.6 b**.

2.2 Application of Blockcopolymer Patterning in Nanotechnology

However, the controlled and well-understood phase separation mechanisms described above for both sacrificial template and coassembly approach are only valid under conditions of thermodynamic equilibrium. Many of the potential application areas rely on thin-film processing techniques. These processing conditions bring additional complications, such as increased evaporation kinetics and unbalanced interactions with the atmosphere or substrate. While these issues may be mitigated somewhat by surface treatment of the substrate, atmospheric control and external guidance via electromagnetic fields, efficient and reproducible processing remains a challenge.

Bibliography

- [1] M. Rubinstei, R.H.C. (2003) *Polymern Physics*, Oxford University Press. [22](#)
- [2] Matsen, M. and Bates, F. (1996) Unifying weak-and strong-segregation block copolymer theories. *Macromolecules*, **29** (4), 1091–1098. [23](#)
- [3] Khandpur, A., Foerster, S., Bates, F., Hamley, I., Ryan, A., Bras, W., Almdal, K., and Mortensen, K. (1995) Polyisoprene-polystyrene diblock copolymer phase diagram near the order-disorder transition. *Macromolecules*, **28** (26), 8796–8806. [24](#), [25](#)
- [4] Cochran, E., Garcia-Cervera, C., and Fredrickson, G. (2006) Stability of the gyroid phase in diblock copolymers at strong segregation. *Macromolecules*, **39** (7), 2449–2451. [24](#)
- [5] Bates, F. and Fredrickson, G. (2000) Block copolymers-designer soft materials. *Phys. Today. February 1999, 32*, **38**. [24](#), [25](#)
- [6] Zheng, W. and Wang, Z. (1995) Morphology of abc triblock copolymers. *Macromolecules*, **28** (21), 7215–7223.
- [7] Epps III, T., Cochran, E., Bailey, T., Waletzko, R., Hardy, C., and Bates, F. (2004) Ordered network phases in linear poly (isoprene-b-styrene-b-ethylene oxide) triblock copolymers. *Macromolecules*, **37** (22), 8325–8341. [25](#)
- [8] Hajduk, D., Harper, P., Gruner, S., Honeker, C., Kim, G., Thomas, E., and Fetters, L. (1994) The gyroid: A new equilibrium morphology in weakly segregated diblock copolymers. *Macromolecules*, **27** (15), 4063–4075.
- [9] Crossland, E.J.W. (2008) *Block Copolymer Patterning of Functional Materials*, PhD Dissertation. [26](#)
- [10] Tanaka, H., Hasegawa, H., and Hashimoto, T. (1991) Ordered structure in mixtures of a block copolymer and homopolymers. 1. solubilization of low molecular weight homopolymers. *Macromolecules*, **24** (1), 240–251. [26](#), [27](#)
- [11] Tanaka, H. and Hashimoto, T. (1991) Ordered structures of block polymer/homopolymer mixtures. 3. temperature dependence. *Macromolecules*, **24** (20), 5713–5720.

- [12] Hashimoto, T., Tanaka, H., and Hasegawa, H. (1990) Ordered structure in mixtures of a block copolymer and homopolymers. 2. effects of molecular weights of homopolymers. *Macromolecules*, **23** (20), 4378–4386.
- [13] Winey, K., Thomas, E., and Fetters, L. (1991) Swelling of lamellar diblock copolymer by homopolymer: influences of homopolymer concentration and molecular weight. *Macromolecules*, **24** (23), 6182–6188. [26](#), [27](#)
- [14] Dair, B., Honeker, C., Alward, D., Avgeropoulos, A., Hadjichristidis, N., Fetters, L., Capel, M., and Thomas, E. (1999) Mechanical properties and deformation behavior of the double gyroid phase in unoriented thermoplastic elastomers. *Macromolecules*, **32** (24), 8145–8152. [26](#)
- [15] Dimitrov, A. and Nagayama, K. (1996) Continuous convective assembling of fine particles into two-dimensional arrays on solid surfaces. *Langmuir*, **12** (5), 1303–1311. [26](#)
- [16] Winey, K.I., Thomas, E., and Fetters, L.J. (1992) Isothermal morphology diagrams for binary blends of diblock copolymer and homopolymer. *Macromolecules*, **25**, 2645–2650. [27](#), [28](#)
- [17] Li, L., Krissanasaeranee, M., Pattinson, S.W., Stefik, M., Wiesner, U., Steiner, U., and Eder, D. (2010) Enhanced photocatalytic properties in well-ordered mesoporous wo3. *Chem. Commun.*, **46**, 7620–7622. [29](#)
- [18] Hsueh, H. and Ho, R. (2012) Bicontinuous ceramics with high surface area from block copolymer templates. *Langmuir*, **28** (22), 8518–8529. [29](#), [30](#)
- [19] Wei, D., Scherer, M., Bower, C., Andrew, P., Ryhnen, T., and Steiner, U. (2012) A nanostructured electrochromic supercapacitor. *Nano letters*, **12** (4), 1857–1862. [29](#), [30](#)
- [20] Crossland, E., Kamperman, M., Nedelcu, M., Ducati, C., Wiesner, U., Smilgies, D., Toombes, G., Hillmyer, M., Ludwigs, S., and Steiner, U. (2008) A bicontinuous double gyroid hybrid solar cell. *Nano letters*, **9** (8), 2807–2812. [29](#), [30](#)
- [21] Li, F., Yao, X., Wang, Z., Xing, W., Jin, W., Huang, J., and Wang, Y. (2012) Highly porous metal oxide networks of interconnected nanotubes by atomic layer deposition. *Nano letters*. [30](#)
- [22] Garcia, B., Kamperman, M., Ulrich, R., Jain, A., Gruner, S., and Wiesner, U. (2009) Morphology diagram of a diblock copolymer- aluminosilicate nanoparticle system. *Chemistry of Materials*, **21** (22), 5397–5405. [30](#)
- [23] De Paul, S., Zwanziger, J., Ulrich, R., Wiesner, U., and Spiess, H. (1999) Structure, mobility, and interface characterization of self-organized organic-inorganic hybrid materials by solid-state nmr. *Journal of the American Chemical Society*, **121** (24), 5727–5736. [30](#), [31](#)

- [24] Kresge, C., Leonowicz, M., Roth, W., Vartuli, J., and Beck, J. (1992) Ordered mesoporous molecular sieves synthesized by a liquid-crystal template mechanism. *nature*, **359** (6397), 710–712. [30](#)
- [25] Beck, J., Vartuli, J., Roth, W., Leonowicz, M., Kresge, C., Schmitt, K., Chu, C., Olson, D., and Sheppard, E. (1992) A new family of mesoporous molecular sieves prepared with liquid crystal templates. *Journal of the American Chemical Society*, **114** (27), 10 834–10 843. [30](#)
- [26] Warren, S., DiSalvo, F., and Wiesner, U. (2007) Nanoparticle-tuned assembly and disassembly of mesostructured silica hybrids. *Nature materials*, **6** (2), 156–161. [31](#)
- [27] Yang, P., Zhao, D., Margolese, D.I., Chmelka, B.F., and Stucky, G.D. (1999) Block copolymer templating syntheses of mesoporous metal oxides with large ordering lengths and semicrystalline framework. *Chem. Mater.*, **11**, 2813–2826. [31](#)
- [28] Buonsanti, R., Pick, T., Krins, N., Richardson, T., Helms, B., and Milliron, D. (2012) Assembly of ligand-stripped nanocrystals into precisely controlled mesoporous architectures. *Nano Letters*, **12** (7), 3872–3877. [31](#)
- [29] Simon, P., Ulrich, R., Spiess, H., and Wiesner, U. (2001) Block copolymer-ceramic hybrid materials from organically modified ceramic precursors. *Chemistry of materials*, **13** (10), 3464–3486. [31](#)
- [30] Stefik, M., Wang, S., Hovden, R., Sai, H., Tate, M., Muller, D., Steiner, U., Gruner, S., and Wiesner, U. (2012) Networked and chiral nanocomposites from abc triblock terpolymer coassembly with transition metal oxide nanoparticles. *Journal of Materials Chemistry*, **22** (3), 1078–1087. [31](#)

Chapter 3

Techniques and Instrumentation

3.1 Fabrication Techniques

3.1.1 Thin Film Deposition

Blade Coating

Blade coating allows the deposition of single films with thicknesses ranging from several hundred nm to microns. In this approach, a drop of the solution is placed on the substrate to be coated, and a sharp blade is drawn across the surface, spreading the solution into a thin layer that is subsequently dried, forming a thin solid film. As illustrated in **Fig 3.1**, varying the blade height (t) controls the film thickness, as does the solution concentration, drying atmosphere, surface preparation and blade draw speed. Upon evaporation of solvent, film thickness of t_f is formed, which depends largely on the solution concentration and the initial blade height (t). In this work, because the fabrication process required oxygen/water free environment, blade coating was carried out manually, inside Bell glovebox under N₂ environment, using a commercially available blade from RK Print Coat Instruments of blade heights variable between 30 μ m and 120 μ m.

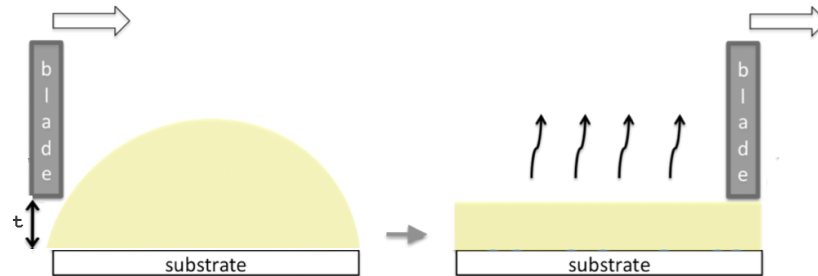


Figure 3.1: Schematic illustration of blade coating

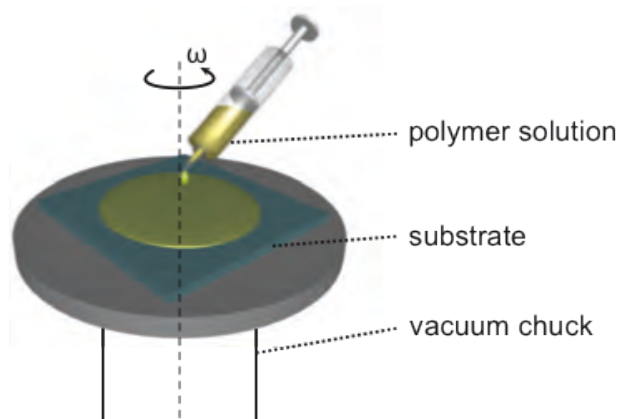


Figure 3.2: Schematic illustration of thin film preparation using spin coating. ^[1]

Spin Coating

In this technique, the substrate is mounted by vacuum chuck to a motorised stage, a droplet of solution is placed on the substrate, and the stage is spun up to a speed as high as several thousand revolutions per minute. Initially, most solution is thrown off of the substrate due to centrifugal force, which then spreads the droplet across the surface to form an intermediate film of t_0 of concentration c_0 . The subsequent outward flow carries most of the solution off the edge of the substrate unto the point of critical film thickness, t_c , which is determined by factors such as solution con-

centration and viscosity, as well as spin acceleration, rate, and time.^[2] Evaporation of the remaining solvent quickly follows, leaving behind a dry film of well-defined thickness.

3.1.2 Atomic Layer Deposition

Unlike conventional CVD which allows the reactants to mix before adsorption of the substrate, [26] Atomic layer deposition (ALD) is a CVD-like epitaxial process based on self-limiting reactions at the deposition surface where each reactant is introduced sequentially. This allows for conformal coverage on features at the nanoscale. However, the additional control afforded by ALD comes at a price in terms of deposition speed and area. They are both reported to produce films with high crystallinity and low defect density.^[3]

A typical ALD growth cycle (Figure 6.) consists of four essential steps summarised as follows:

- 1) precursor exposure of the first reactant for a self-terminating reaction (pulse)
- 2) evacuation or purging of the non-reacted precursors and any byproducts from the chamber (purge)
- 3) exposure of the second reactant for a self-terminating reaction or additional surface treatment reaction to deposit the first reactant (pulse)
- 4) evacuation or purging of the non-reacted reactants and byproduct molecules from the chamber. (purge)

The result is a monolayer-thickness film of the reaction product on the substrate. This process is repeated multiple times to gradually build up a thicker film. The main advantage of ALD is that the self-limiting reaction between the reactants and the surface of the substrate inherently allows uniform and conformal surface coverage. This allows deposition onto substrates of complex shapes and small feature

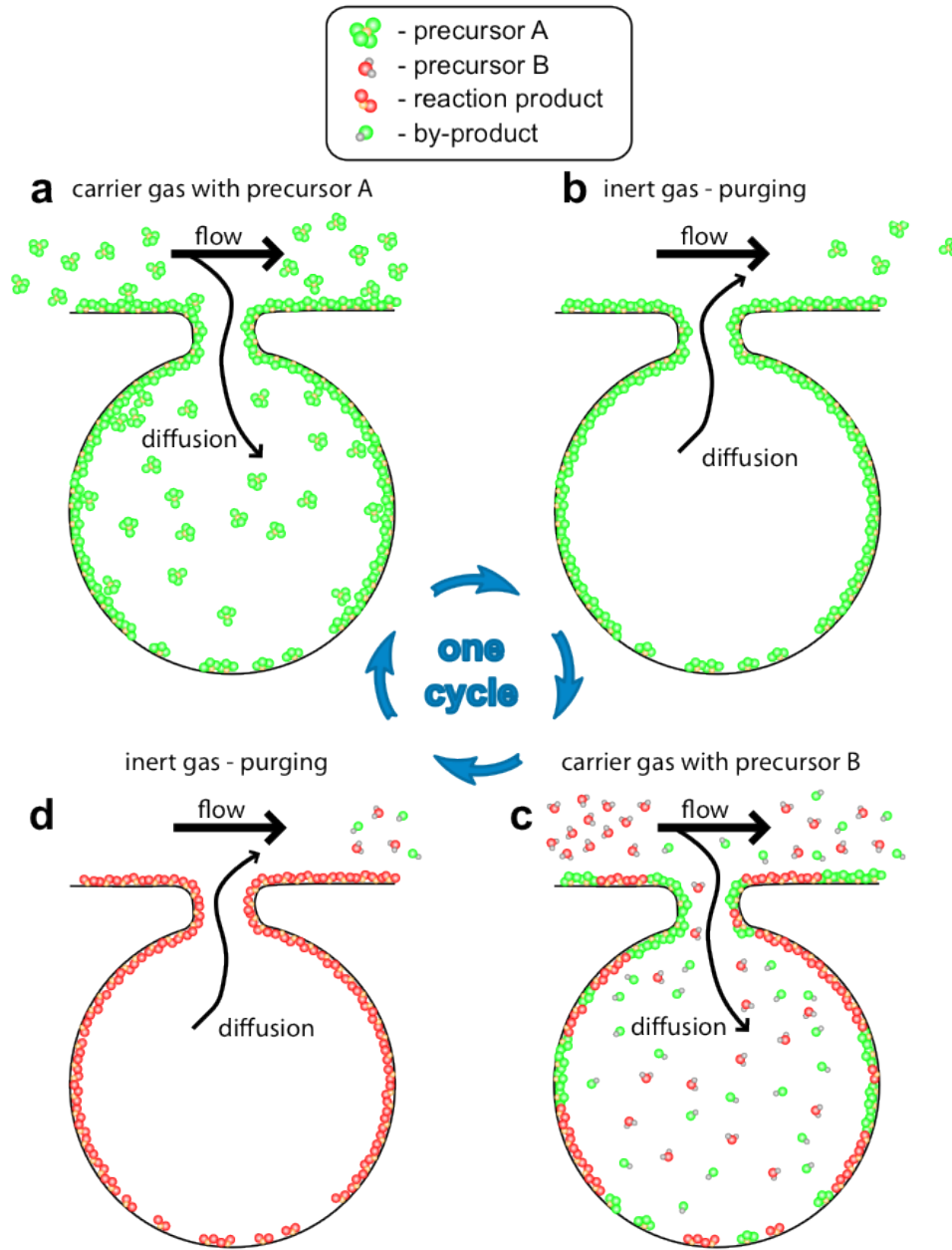


Figure 3.3: One full cycle of ALD onto a porous substrate^[?]], including a) introduction of first precursor species(A) into the chamber leading to deposition of the precursor via surface-limited reaction b) purging of chamber to remove the non-reacted precursors and reaction byproducts. The next two steps- c), d) -repeat the steps a) and b) with the second precursor (B) . The purging step for porous substrates requires a longer duration compared to the flat substrates, due to limited accessibility of the area through which the molecules can travel.

sizes, though successful deposition onto such substrates would require considerable control over the parameters such as molecular flux, adsorption probability and surface diffusion for different types of surfaces (e.g. wall, hole, or a flat top surface).

Beneq was used for ALD deposition, and the precursors for ZnO deposition were diethyl zinc $(C_2H_5)_2Zn$, purchased from ABCR GmbH Co. KG, and deionized water (H_2O). Deposition cycles ranged from 65 to 250 cycles. Though numerous variations of recipes were tried, a typical Pulse/Purge times for continuous flow method were 30s for the first 30 cycles, 1 minute for the second 40 cycle, and 2 minutes for the third 30 cycles. A typical half cycle of stop-flow recipe included 10s pulse, 1 minute hold time with the vacuum and nitrogen flow off, purge for 1 minute. Deposition was normally carried out at 80 °C, but for depositions at 100 °C and 120 °C were made for comparison.

3.1.3 Sol-Gel

Sol-gel chemistry allows formation of inorganic matrix by first forming nanoparticles (sol) and then through gelation of such particles, a liquid phase (gel). For transitional metal oxides, non-hydrolytic route using metal alkoxides and alcoholic solvents to undergo a slow reaction, forming oxide networks. The initial pH of the reaction often needs to be controlled and sometimes addition of acid or base is required. Gelation is a transition process between the sol state to the gel state and at gelation point, there is a sharp increase in viscosity of the mixture. From this point on, the solution undergoes aging, which entails stiffening and condensation of the network. The prepared solutions are deposited onto substrates using appropriate deposition methods such as spin coating, drop casting, and blade coating. When all the solvents in the solution is dried, the prepared sample undergo heat treatment at high temperatures where the network transforms into a metal oxide.^[4]

The reason that metal alkoxides present themselves as ideal candidates for a solu-

tion sol-gel process is due to the ease of M-O-M bond formation via the energetically favorable extrusion of organics via a condensation mechanism. This is attributed to the large difference in the Pauling electro-negativity between the electropositive cation and electronegative oxygen forming the ionic bonding RO-M. Additionally the ability of the organic ligand moiety to undergo a beta hydride elimination mechanism can stimulate the decomposition of the parent alkoxides to their respective metal oxide component upon pyrolysis.

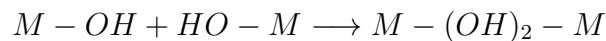
The general step involved in the sol-gel polymerisation reactions proceed through a set of hydrolysis and condensation reaction between the metal alkoxides $M(OR)_x$, where M is a metal (e.g. Zn, In, Ga) and OR is an alkoxy group, (R) is $CH(Me)_2$ and CH_2CH_2OMe). This can begin with hydroxylation upon the hydrolysis of alkoxy groups;



This is followed by polycondensation step leading to the formation of oligomers and/or polymers with a metal oxo based skeleton framework with and reactive residual hydroxo and alkoxy groups. There are two competitive mechanisms, oxolation : which is the formation of oxygen bridges :



Which generally occur when the hydrolysis ratio $h = H_2O/M \gg 2$, or $X = R$, when $h = H_2O/M < 2$. The second competing condensation mechanism is called ololation, which occurs through the formation of hydroxo bridges when the coordination of the metallic center is not fully satisfied,



The kinetics of olation are usually faster than those of oxolation, which is the desired mechanistic route towards mixed metal oxide with high electrical performing properties such as conductivity for TCOs and mobility for Semiconducting oxides. Another added benefit of the alkoxides is their ability to form mixed metal alkoxide molecular chemical precursors.

3.2 Characterisation Techniques

3.2.1 Electron Microscopy

Scanning Electron Microscopy

In scanning electron microscopy (SEM), a beam of electrons is accelerated in vacuum to tens of keV, focused onto a sample, and then raster scanned across the surface. An image is formed by mapping the signal from one of several detectors to the location of the primary electron beam. For resolving surface details, the most common approach is to detect low-energy (< 50 eV) secondary electrons that are produced by inelastic scattering from the surface atoms of the sample material (< 10 nm). In the in-lens detection technique, these secondary electrons are accelerated and focused to a detector made of a scintillator material placed in front of a photomultiplier tube. The scintillator generates visible light, which is converted to a voltage signal by the photomultiplier. In this mode, commercial instruments are capable of approximately 5 nm image resolution.

In this work, SEM characterisation was undertaken with a commercial electron microscope (LEO Ultra 55) working with in-lens detection of secondary electrons. For non-conducting materials, in order to prevent contrast artefacts from electrostatic charging, samples were coated with a thin (< 2 nm) film of Au/Pd deposited from a sputter coating system (Emitech K575X, 10 s, 70 mA).

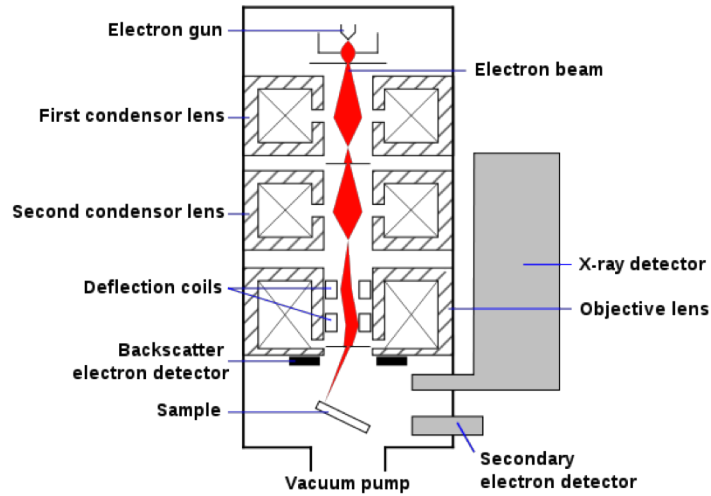


Figure 3.4: Schematic illustration of scanning electron microscope (SEM) ^[5]

Transmission Electron Microscopy

Transmission electron microscopy (TEM) is distinguished from SEM by the detector placement behind the sample, and so detecting electrons that pass through the material. In this approach, electron beam energy is considerably higher (hundreds of kV) and the image resolution can be better than 1 nm in commercial instruments.

Electrons that pass directly through the sample without scattering (or only weakly so) are detected in the bright-field imaging mode. Image contrast then represents scattering contrast, which reveals information about morphology, composition, and crystallinity. Those electrons scattered at large angles may be detected in so-called diffraction mode, which picks up electrons scattered coherently via Bragg diffraction. This diffracted electron beam provides information on crystalline structure such as unit cell size, crystal orientation, and polycrystallinity.

The TEM characterisation was carried out through Dr. Caterina DuCati at the Department of Materials Science, University of Cambridge using FEI TEcnai F20-G2 FEG TEM and Dr. Doohyun Ko with JEOL 100CX II TEM at the University

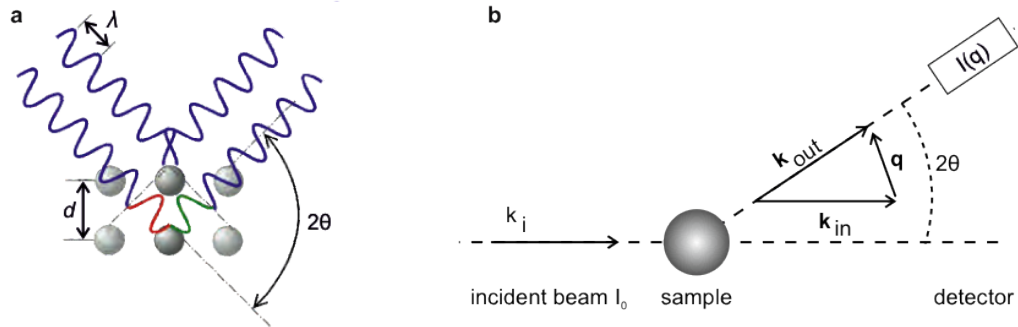


Figure 3.5: Principles of XRD a) Scattering of incident waves from crystal lattice. b) Schematic of a scattering experiment^[7]

of North Carolina, USA.

3.2.2 X-ray Diffraction

X-ray diffraction (XRD) is a well-known elastic x-ray scattering technique for studying the crystalline structure of many classes of materials. The constructive interference of x-rays diffracted from a periodic lattice is used to determine the lattice structure by imaging in reciprocal space.^[6] This may be an atomic lattice, crystallised organic molecules, or even larger structures such as phase-separated block copolymers.

The constructive interference of diffracted waves is described by the Bragg diffraction condition for lattices with inter-plane spacing d :

$$n\lambda = 2d \sin \theta \quad (3.1)$$

Here n is the integer diffraction order, λ is the x-ray wavelength, and θ is the angle between the incident x-ray beam and the lattice plane. The intensity of the diffracted radiation is often measured as a function of scattering angle, on a diffractometer instrument typically comprised of x-ray source and monochromator,

goniometer for sample rotation, and x-ray detector. The characteristic K_α x-rays of copper ($\lambda = 1.54 \text{ \AA}$) are often used for probing the atomic lattices of solid-state materials. The comparable lattice dimension diffracts the x-rays through a wide angle ($2\theta = 10\text{-}80^\circ$), giving name to this technique known as wide-angle x-ray scattering (WAXS). By contrast, small-angle x-ray scattering (SAXS), which implies $d \gg \lambda$, may be used to study larger-scale structures and features. Only the lattice spacing between scattering centers is determined by the Bragg analysis. Further information about their size, and the finite size of the crystal or crystallite may be learned by describing the scattered intensity $I(\mathbf{q})$ as given in **Eq.3.2**.^[8]

$$I(\mathbf{q}) \propto |F(q)|^2 \cdot |Z(\mathbf{q}) * \sum(\mathbf{q})|^2 \quad (3.2)$$

Here $q = k_{out} - k_{in}$ is the scattering vector in reciprocal space, $F(q)$ is a form factor that describes the dimensions of the scattering object, and the final term is a convolution of the reciprocal lattice $Z(q)$ and a Fourier-transformed step function $\sum(\mathbf{q})$ representing the finite crystal size. In this work, WAXS studies of ZnO and I(G)ZO crystal structures were carried out with a commercially available Bruker D8 Advance diffractometer.

3.2.3 Dynamic Light Scattering

Dynamic light scattering (DLS) is a form of photon correlation spectroscopy which can be used to determine various properties of particles suspended in solution, such as particle size distribution, zeta potential, or polymer molecular weight. In this technique, intensity fluctuations of the characteristic speckle pattern arising from quasi-elastic laser light scattering are used to determine the diffusion rate of the suspended particles.^[9,10] These particles may be colloidal suspensions, hydrolysed sols, or synthesised nanocrystals. The experimental set-up of DLS is depicted in

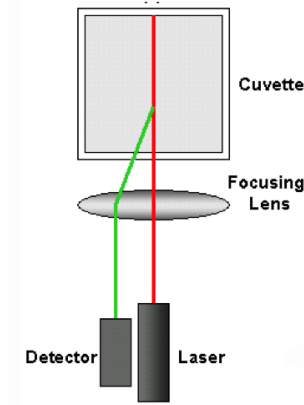


Figure 3.6: Schematics of DLS measurement set-up. Depending on the opacity of the sample, the position of focusing lens can be altered. ^[10]

Fig. 3.6.

The time-varying intensity $I(t)$ of the speckle pattern can be measured and, with some assumptions, the properties of the suspension can be found from the autocorrelation function $G(\tau)$, defined as

$$G(\tau) = \frac{\langle I(t)I(t + \tau) \rangle}{\langle I(\tau) \rangle} \quad (3.3)$$

For a large number of monodisperse particles such as in a colloidal suspension, the autocorrelation can be modelled as a single exponential decay:

$$g_1(\tau) = A[1 + B \exp(-2\Gamma\tau)] \quad (3.4)$$

Here A and B are constants for amplitude and intercept, while the exponential decay rate Γ is given by

$$\Gamma = Dq^2 \quad (3.5)$$

In this equation, $D = kT/6\pi\eta r$ is the translational diffusion coefficient given by the Stokes-Einstein equation, and is determined by the effective hydrodynamic radius r of the particle. The optical properties of the laser, solution and detector

system are encapsulated in q :

$$q = \frac{4\pi n}{\lambda_0} \sin\left(\frac{\theta}{2}\right) \quad (3.6)$$

Here n is the refractive index of the dispersant, λ_0 is the laser wavelength and θ is the detector scattering angle. Thus, the particle size r can be determined by fitting the exponential decay in the autocorrelation measurement. Polydisperse samples may be modelled similarly, but by treating the autocorrelation data as a sum of many exponentials, resulting in a particle size distribution. Typically, a samples particle size distribution is derived by fitting the sum of multiple exponential curves using non-negative least squares fitting or specialised algorithms such as CONTIN.^[10] Further application of e.g Rayleigh scattering theory allows determination of other properties of the suspension such as volume fraction, though for particles much smaller than the laser wavelength these calculations become highly error-prone. In this study, DLS measurements were carried out using a Malvern Zetasizer ZS.

3.2.4 X-ray Photoelectron Spectroscopy

Photoelectron Spectroscopy is based on collection of photoelectrons emitted upon illumination of either ultraviolet or X-rays onto the samples. 1980quantitative The kinetic energy of emitted photoelectrons, measured in terms of the number of detected electrons in the analyser, are plotted with respect to the binding energy of electrons. Ultraviolet Photoelectron Spectroscopy (UPS) and X-ray Photoelectron Spectroscopy (XPS). The energy of ultraviolet rays (<41 eV) is sufficient to only eject electrons from valence orbitals, whereas the high energy of X-rays (1000-1500ev) can probe the core levels. The binding energies of electron indicates the core energy levels of specific chemical elements. Therefore, XPS allows elemental analysis of a given material. In addition, deviation of binding energy from those of

isolated elements can provide information on the chemical environment in which the element is found. The collected plots provide information on the electronic structure as well as the chemical bonding and composition of the molecules.

The XPS in this work was carried out by Dr. Yana Vaynzof at the department of physics, University of Cambridge X-ray photoemission spectroscopy measurements: The Gyroid ZnO samples were fabricated on SiOx.Si and transferred to the ultrahigh vacuum (UHV) chamber (ESCALAB 250Xi) for XPS measurements. The measurements were carried out using a XR6 monochromated Alk α X-ray source ($h\nu = 1486.6$ eV) with a 650 μ m spot size. For the XPS depth profiling, the Ar $^{+}$ ion gun etching was performed using ion energy of 3000 eV.

3.2.5 Ellipsometry

Ellipsometry is an optical characterisation technique used to measure a variety of thin film optical properties, including dielectric constant/refractive index, thickness, and film uniformity. The name belies the basic approach, where visible light is elliptically polarised by means of a compensator or birefringent wave plate, reflected at an angle off the sample, and analysed with another linear polariser. Rotating the analyser allows a measurement of the ratio and phase relationship between parallel (P) and perpendicular (S) components.^[11,12] The amplitude ratio and phase shift between these components, introduced by the sample, are described by the so-called ellipsometric angles Ψ and Δ , where the complex reflectivity is

$$\rho = \tan(\psi)e^{i\Delta} \quad (3.7)$$

$$\tan \Psi = \frac{|r_p|}{|r_s|} \quad (3.8)$$

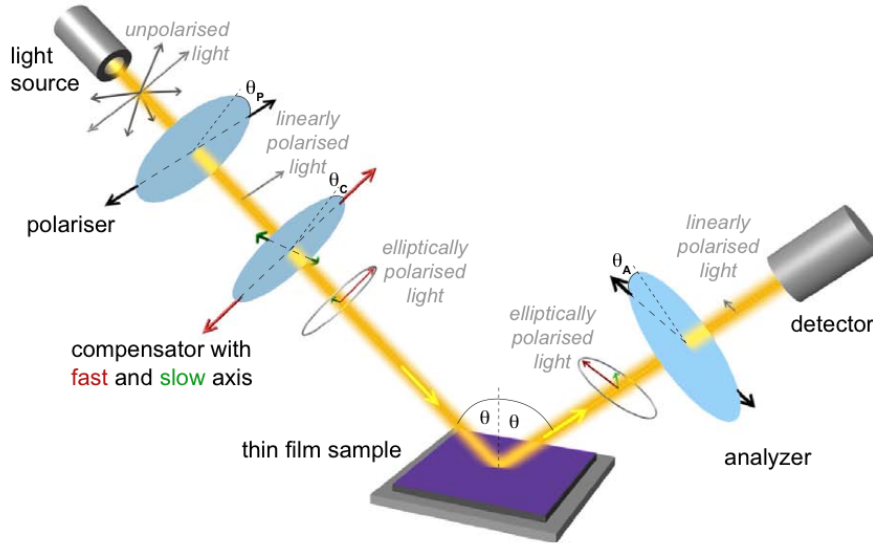


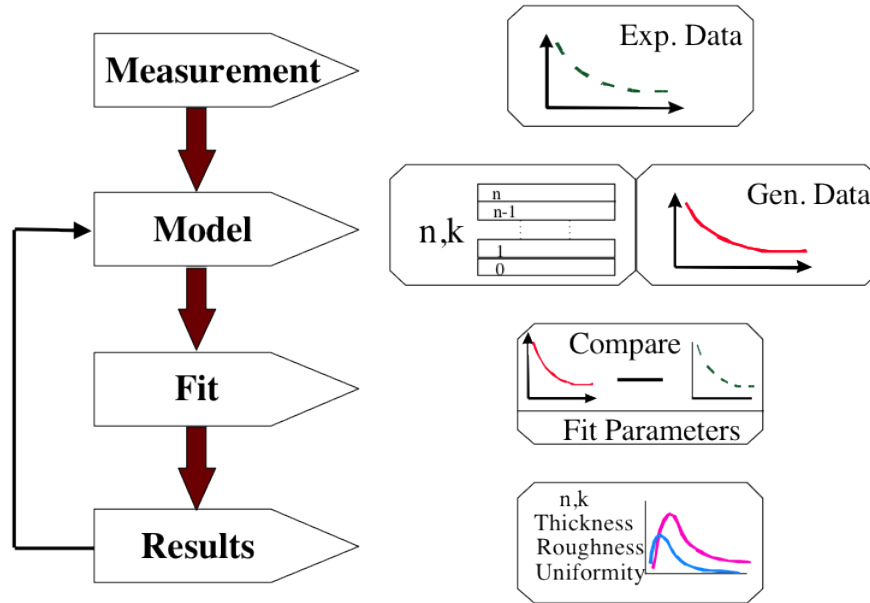
Figure 3.7: Illustration of thin film characterisation of ellipsometry using a polariser - compensator - sample - analyser (p-c-s-a) configuration^[1]

$$\Delta = \delta_p - \delta_s \quad (3.9)$$

The reflection of the incident light wave is described in terms of the Fresnel reflection coefficients r_p and r_s , which transform the incident parallel and perpendicular electric field components E_p and E_s :

$$\begin{pmatrix} E_{p,out} \\ E_{s,out} \end{pmatrix} = \begin{pmatrix} r_{pp} & r_{sp} \\ r_{ps} & r_{ss} \end{pmatrix} \cdot \begin{pmatrix} E_{p,in} \\ E_{s,in} \end{pmatrix} \quad (3.10)$$

This matrix may be expanded by use of the Jones matrices for each component of the ellipsometer configuration. The system described above is a so-called polarizer-compensator-sample-analyzer configuration, where each component has a simple Jones matrix along with simple rotation matrices with respect to the plane of incidence:


 Figure 3.8: Procedure for analysis using the data obtained by ellipsometry^[13]

$$R(\theta_a) \begin{pmatrix} 1 & 0 \\ 1 & 0 \end{pmatrix} R(-\theta_a) \begin{pmatrix} r_p & 0 \\ 0 & r_s \end{pmatrix} R(\theta_c) \begin{pmatrix} 1 & 0 \\ 0 & i \end{pmatrix} R(-\theta_c) R(\theta_p) \begin{pmatrix} 1 & 0 \\ 1 & 0 \end{pmatrix} R(-\theta_p)$$

analyser (a) sample (s) compensator (c) polariser (p)

The ellipsometric angles are only an indirect measurement of the dielectric properties of the film. Once known, they must be converted into useful quantities by regression analysis with a model that includes a reasonable description of the physical characteristics of the material.^[13] (**Fig 3.8**)

Spectroscopic ellipsometry is an extension of the basic principle, where instead of a fixed wavelength light source, a broad spectrum source is used and monochromated and scanned across a range of wavelengths. In this work, ellipsometry was used to determine the thickness as well as the refractive index of the film. J.A. Wollan alpha-SE spectroscopic ellipsometer was used ($\lambda = 380\text{-}900$ nm), and fitting of the data was carried out using the models, which were available in the software.

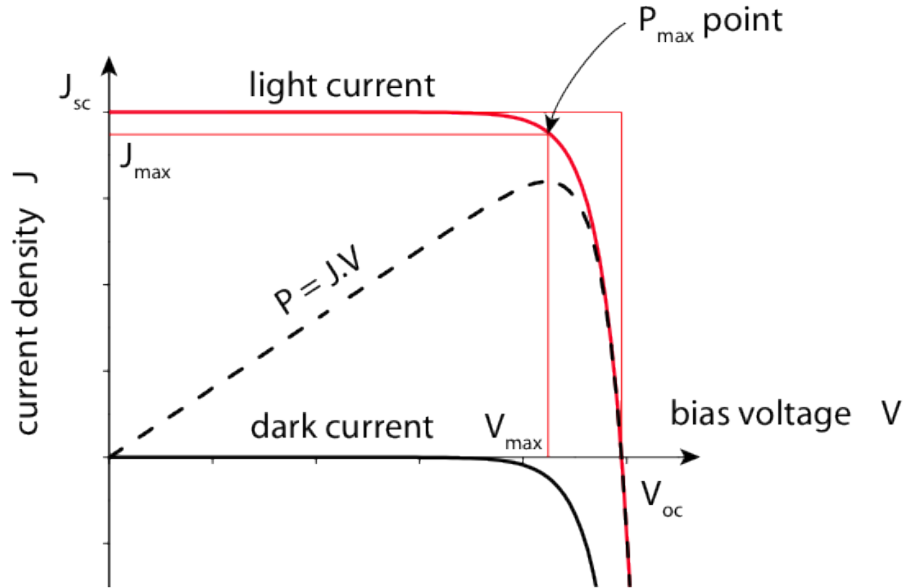


Figure 3.9: A typical $J - V$ curve measured from a solar cell^[14]

3.2.6 Solar Cells Characterisation

The characterisation of solar cell device performance follows a well-established regimen. Most of the electrical characteristics may be understood by examination of the J - V curve of the cell, as illustrated in Figure **Fig 3.9** .

The short-circuit current J_{sc} is the solar cell current density measured under short-circuit conditions; in other words, this is the maximum sustained current output possible from the cell. As a voltage bias is applied, the current flow eventually drops. The open-circuit voltage V_{oc} is defined as the applied bias at which the current drops to zero. V_{oc} is then the maximum voltage possible under infinite load resistance.^[15]

The solar cell may be operated at any point along this curve (including forward bias, in which the current flow is reversed and the cell operates as a light-emitting diode, or reverse bias, in which it acts as a photodiode). The power density of the

cell is simply the current-voltage product, and peaks at P_{max} , the point of maximum power. J_{max} and V_{max} are simply the current and voltage values corresponding to the location of P_{max} on the measured curve. V_{oc} , J_{sc} describe a rectangular region on the current-voltage plane; a similar, smaller rectangle is described by J_{max} and V_{max} ; the fill factor FF is defined as the ratio of the areas of these two rectangles. (Eq. 3.12) Fill factor is a quantitative measure of the actual device behaviours deviation from an ideal square curve.

$$FF = \frac{P_{max}}{J_{oc} \cdot V_{oc}} \quad (3.11)$$

The primary figure of merit for a solar cell is the power conversion efficiency η , which is defined as the ratio of electrical power per unit area to the irradiance (power per unit area) of the incident illumination:

$$\eta = \frac{P_{max}}{P_{in}} = \frac{V_{oc} \cdot J_{sc} \cdot FF}{P_{in}} \quad (3.12)$$

Increasing V_{oc} , J_{sc} , and FF all contribute to improvements in the power conversion efficiency.

A more fundamental measure is the EQE or external quantum efficiency, which is simply the number of charge carriers generated and delivered to the external load per incident photon. The EQE is typically characterised as a function of photon wavelength, as actual device performance is strongly dependent the light sources spectral distribution.

In light of this dependence, the efficiency performance of real devices is typically measured under standardised conditions, called Air Mass 1.5 (AM1.5) illumination. This spectral distribution matches measured solar radiation at the earths surface, modelling the sun as a blackbody radiator at 5760K, and attenuating the spectrum with scattering and absorption features due to atmospheric components. Air Mass 1.0 describes terrestrial illumination with the sun directly overhead, while higher

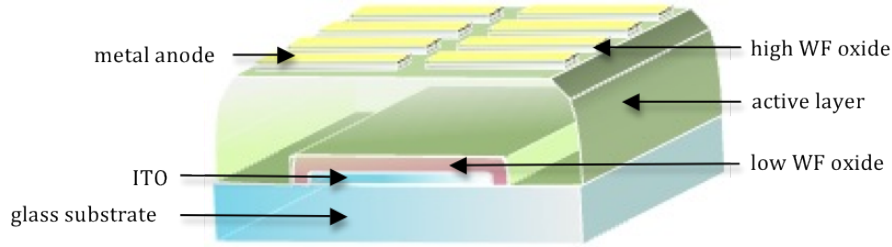


Figure 3.10: Basic configuration of an inverted hybrid solar cell^[5]

air mass numbers correspond to longer atmospheric path lengths at lower angles. Air Mass 1.5 then describes a realistic illumination scenario, with the sun at $\arccos(1/1.5) = 48$ degrees from vertical.

In this work, solar cell fabrication and measurements were carried out in order to demonstrate the functionality of the mesoporous ZnO films fabricated in Chapter 5 and Chapter 7. Inverted P3HT-ZnO hybrid solar cell with an architecture shown in **Fig 3.10** was used. WO_3 was used as a high work function oxide, and Ag was used as the metal anode material. A compact layer of ZnO was deposited by ALD ($\sim 30\text{-}50\text{nm}$) on a conductive prepatterned ITO substrate. On top of the compact layer, a mesoporous ZnO layer was deposited, and infiltrated with a poly(3-hexylthiophene) (P3HT) polymer. Upon preparation of the active mesoporous ZnO layer, the rest of solar cell fabrication as well as the performance measurements were undertaken by Dr. Yana Vaynzof at the Department of Physics, University of Cambridge.

For External Quantum Efficiency (EQE) measurements (in air) a 250 W tungsten halogen lamp and an Oriel Cornerstone 130 monochromator were used. The measurements were performed as a function of wavelength at intensities $\sim 1 \text{ mW}/\text{cm}^2$. To measure the J-V curve of the device under AM1.5 conditions, an ABET Solar 2000 solar simulator was used. In order to obtain reliable data, a spectral mismatch correction is carried out using a calibrated and certified inorganic solar cell.

Bibliography

- [1] Kolle, M. (2011) *Photonic Structures Inspired by Nature*, Springer. [37](#), [49](#)
- [2] Lawrence, C. (1988) The mechanics of spin coating of polymer films. *Physics of Fluids*, **31** (10), 2786–2795. [38](#)
- [3] Kim, H., Lee, H., and Maeng, W. (2009) Applications of atomic layer deposition to nanofabrication and emerging nanodevices. *Thin Solid Films*, **517** (8), 2563–2580. [38](#)
- [4] Brinker, C. and Scherer, G. (1990) *Sol-gel science: the physics and chemistry of sol-gel processing*, Academic Pr. [40](#)
- [5] Vaynzof, Y. (2011) *Improved Photoinduced Charge Carriers Separation in Organic-Inorganic Hybrid Photovoltaic Devices*, PhD Dissertation, University of Cambridge, UK. [43](#), [53](#)
- [6] Bacon, G. (1966) *X-ray and Neutron Diffraction*, Pergamon. [44](#)
- [7] Guldin, S. (2012) *Inorganic Nanoarchitectures by Organic Self-Assembly*, PhD Dissertation, University of Cambridge, UK. [44](#)
- [8] Roe, R. (2000) *Methods of X-Ray and Neutron Scattering in Polymer Science (Topics in Polymer Science)*, Oxford University Press. [45](#)
- [9] Pecora, R. (2000) Dynamic light scattering measurement of nanometer particles in liquids. *Journal of nanoparticle research*, **2** (2), 123–131. [45](#)
- [10] Instruments, M. *Dynamic Light Scattering: An Introduction in 30 Minutes*, mrk656-01 edn.. [45](#), [46](#), [47](#)
- [11] Lee, J., Rovira, P., An, I., and Collins, R. (1998) Rotating-compensator multichannel ellipsometry: Applications for real time stokes vector spectroscopy of thin film growth. *Review of scientific instruments*, **69** (4), 1800–1810. [48](#)
- [12] Woollam, J., Johs, B., Herzinger, C., Hilfiker, J., Synowicki, R., and Bungay, C. (1999) Overview of variable angle spectroscopic ellipsometry (vase), part i: basic theory and typical applications. *Proc. SPIE CR72*, pp. 3–28. [48](#)

BIBLIOGRAPHY

- [13] Woollam, J., Hilfiker, J., Tiwald, T., Bungay, C., Synowicki, R., Meyer, D., Herzinger, C., Pfeiffer, G., Cooney, G., and Green, S. (2000) Variable angle spectroscopic ellipsometry in the vacuum ultraviolet, in *Proc. SPIE*, vol. 4099, pp. 197–205. [50](#)
- [14] Crossland, E. (2008) *Block Copolymer Patterning of Functional Materials*, PhD Dissertation, University of Cambridge, UK. [51](#)
- [15] Nelson, J. (2003) *The physics of solar cells*, vol. 57, World Scientific. [51](#)

1

Chapter 4

Fabrication of Porous Polymer Templates

4.1 Introduction

As discussed in Chapter 2, the microphase separation of block copolymers (BCP) under equilibrium conditions leads to self-assembly into ordered arrays of nanoscopic domains with cylindrical, lamellar, micellar, and double gyroid arrangements. This process is governed mainly by the molecular architecture of the block copolymer, with feature sizes determined by the molecular weight of the BCP on a length scale between 10 nm-100 nm.

The double gyroid morphology, in particular, is an appealing candidate for 3D nanostructured templates. The gyroid structure consists of two interwoven, periodic, continuous networks of the minority block surrounded by a matrix of the majority block. Upon selectively etching the minority phase, a free-standing, porous and highly periodic polymeric templates can be obtained. Realising such a structure with a length scale of < 50 nm is not yet possible using any conventional 3D lithography methods.

Therefore, polymeric templates of gyroid morphology have been exploited to create functional materials for applications in photocatalysis, solar cells, electrochromic devices and super capacitor.^[1-4], where the high surface area to volume ratio of the replicated gyroid structure is beneficial.

However, the gyroid morphology corresponds to a very narrow region of the phase diagram and can only be achieved under conditions of thermodynamic equilibrium. Therefore, fabrication of thin film gyroid polymeric template, let alone the replication of the functional material, is not a straight forward process. So far, the only gyroid system successfully used in aforementioned functional materials has a pore size of < 10 nm, which can be often too small for certain technological applications. Finnemore et al^[5] used a bicontinuous gyroid (in bulk form) for guiding single-crystal calcite growth structured with extreme periodicity on the sub-50 nm length scale.

In addition, processing of gyroid structure can be time-consuming and extremely delicate, which from an industrial point of view is not very versatile. For example, most recently, Yu et al. reported sol-gel fabrication of gyroid TiO_2 using PS-PLLA as a sacrificial template.^[1] However, the gyroid templates, which took over 17 days to fabricate, were again in bulk (≤ 10 m) form.

For many applications, useful templates must be processed into thin films. However, the conditions required to reach equilibrium often conflict with the nature of thin film processing, which entails fast evaporation kinetics and surface interactions between the substrate, film, and air. Still to this date, thin film deposition of self-assembled BCP remains a challenge, as most of the gyroid templates used have been fabricated in bulk, with thicknesses of tens of microns.

Another way to achieve three-dimensional bicontinuous architectures from BCP phase separation is to take advantage of an off-equilibrium system. BCPs of a composition normally corresponding to lamellar or cylindrical phases can result in a

bicontinuous and porous wormlike morphology when spin coated, which freezes the system at a state far from equilibrium.^[6] Although this structure is less periodic than the gyroid structure, processing is easy and quick by comparison, and the resulting film retains many of the desirable properties as a sacrificial porous template. Reports on the film quality or thin film fabrication of both gyroid and wormlike morphologies are limited.

In this chapter, the 3D bicontinuous and self standing polymer template with pore size on the 20-40 nm length scale was fabricated in thin films of controllable thickness between 200 nm and 4 μ m. The aim was to produce a robust, reliable route to porous film fabrication, in order to act as a sacrificial template for a range of functional materials.

The PS-PI BCP system introduced by Finne^{more} *et al.*^[5] was chosen. Two main reasons lead to the choice of system for this study. It leads to phase-separated structures on a length scale (20-40-nm) desirable for solar cell application. In addition, the polymers used are commercially available, which makes this route versatile and easily applicable to other technological systems.

The intended purpose of the porous templates fabricated in this chapter is for use in ALD replication, as well as solution impregnation of metal oxides (Chapters 5 and 6). For the polymer template to be used for creating metal oxide thin films by either of the two routes, it must satisfy four basic criteria:

- The pores must be open and accessible from the top surface of the film.
- The pores must be interconnected so that the resulting film is free-standing.
- The thickness of replicated metal oxide depends on the thickness of the porous template. Therefore, the film thickness of the porous template must be controllable.
- The film quality must be smooth and consistent across a wide area.

Fabrication of gyroid films were carried out by closely following the previous protocols developed by Scherer^[7], using a modified form of drop casting referred as “sandwich casting” method as well as spin coating followed by a post-annealing process. In addition, thin films of the wormlike morphologies were fabricated by spin coating the same solution used to prepare gyroid films. The spin-coated wormlike structured enabled close examination of the elements of the fabrication process, due to its quick fabrication steps and consistency of resulting films. Each preparation process was studied with a focus on understanding the role it plays in the final morphology, which provided control of this system as well as general insights into future template design for other applications.

4.2 Experimental

4.2.1 Materials

Toluene, Analytical grade, 98%, analytical grade, Fischer scientific, UK The polymers used in this study are commercially available, the details of which are summarized in **Table 4.1** and **Fig.4.1**.

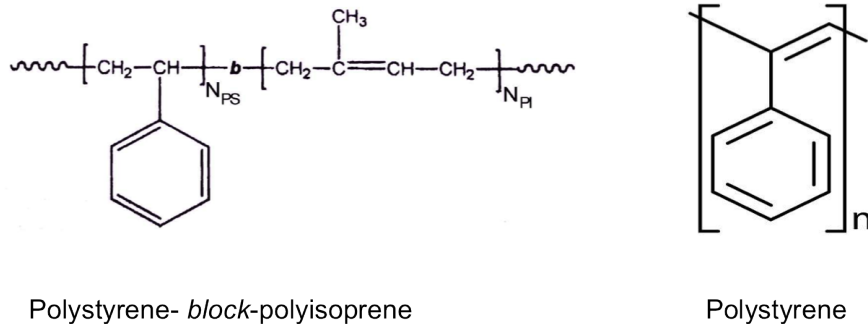


Figure 4.1: Molecular structures of PS-b-PI and PS

Poly(styrene-block-isoprene) BCP was purchased from Polymer Source Inc., Canada

Polymer	$M_{n,PS}$ (kg/mol)	$M_{n,PI}$ (kg/mol)	f_{PS}	Supplier
Polystyrene	45	39	0.49	Sigma Aldrich, UK
PS-b-PI	8.7	N/A	1	Polymer Source, Canada

Table 4.1: Details of the polymers used for fabrication of porous templates

and Polystyrene homopolymer from Sigma Aldrich, UK.

4.2.2 Fabrication Steps

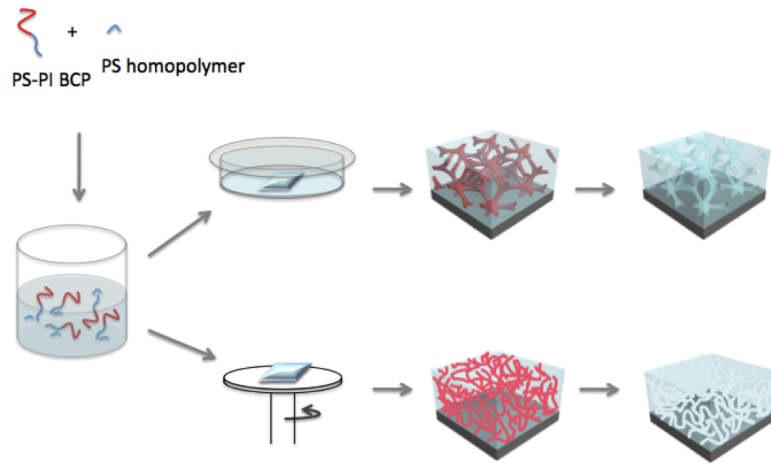


Figure 4.2: Schematics of gyroid and wormlike deposition process

1) Preparation of the polymer solution of the correct composition

As illustrated in **Fig. 4.2**, fabrication of both wormlike and gyroid morphologies starts from the same polymer solution which was carefully mixed based on an empirical compositional study.^[7] Starting with a lamellae-forming fraction of PS-PI block copolymer dissolved in toluene, the PS volume fraction was altered by addition of PS homopolymer, which selectively swells the PS block of PS-PI, forming a BCP-like system with a new volume ratio between PS and PI blocks, with the overall volume fraction of PS increased by the contribution of the homopolymer. (The detailed mechanism of this process is previously discussed in Chapter 2.) Con-

sequently, the change in volume fraction leads to a morphology transition. The composition-morphology relationship of this specific polymer system was previously mapped^[7] and it was found that gyroid morphology was obtained by slowly drying the hPS/PS-b-PI blend with an overall composition of $f_{\text{PS}} = 65\%$ at 4°C . Therefore, the polymers were dissolved in toluene so that the final solution contained 65% volume fraction (f_{PS}) of polystyrene. The concentration of the polymer solution varied from 4.5 % to 17 % by weight.

2) Deposition of the polymer solution

Gyroid formation using sandwich casting

Sandwich casting, as previously reported^[7], was the main deposition method for gyroid fabrication. This technique slows the evaporation of the solvent, which allows the system enough time to reach equilibrium. The polymer solution was drop-casted onto a $1.4\text{ cm} \times 1.4\text{ cm}$ Si substrate, and a PTFE film of $1.2\text{ cm} \times 1.2\text{ cm}$ was placed on top of the droplet. The sample was then placed into an enclosed chamber containing 20 l of toluene, in order to create a solvent-rich atmosphere. The chamber was covered with a glass slide, sealed by vacuum grease, and left uninterrupted for a week in a refrigerator at 4°C . The chamber was taken out of the refrigerator and placed in fume hood at room temperature for an additional 24 hours, for the final drying of the film.

Wormlike structure formation using spin-coating

Since wormlike structures are achieved at an off-equilibrium state, spin coating was used as a deposition method. 50 l of polymer solution was spin coated onto a substrate of $1.4\text{ cm} \times 1.4\text{ cm}$. This quantity normally flooded the substrate. The substrates were spun at various spin speeds of 750-200rpm.

3) Selective chemical etching of polyisoprene

Once the phase separated BCP film was deposited, the films were made porous by selectively removing the polyisoprene block. The films were exposed to UV light at

254 nm for a duration of 2-12 hours. The radiation cleaves the C=C backbone of polyisoprene, which then becomes soluble in ethanol.^[8] The sample was immersed in ethanol for over 12 hours followed by further rinsing in methanol and slowly drying slowly by placing the samples faced down onto a lint-free tissue, leaving behind a porous polystyrene template.

4.3 Results and Discussion

4.3.1 Gyroid structure

Gyroid Fabrication by Sandwich Casting

Fig. 4.3 shows the SEM representation of gyroid templates obtained by the sandwich casting method.

Controlling the thickness of the resulting film using this method proved difficult. The resulting films from 17 wt% solution had a thickness ranging between 6 and 10 μm . By diluting the polymer solution to 10 wt%, the thickness range decreased to 4-7 μm . However, when the concentration was reduced further to 5 wt%, phase separation was often not observed. Similar observations were also reported in Scherer's work^[7] (**Fig. 4.4**). Although the gyroid structure was consistently achieved using sandwich casting, the resulting films often suffered from cracking and peeling, as well as inconsistent thickness throughout the film.

In addition, the majority of the films exhibited a dense, non-porous layer at the top of the film which was not dissolved by the ethanol (**Fig. 4.5 c**). A hypothesised mechanism for the formation of this layer is that part of the homopolymer separates into a macrophase, driven by diffusion of the toluene solvent towards the film surface. Unlike the observations in Scherer's study^[7], a thick compact top layer (up to 1 μm in thickness) was observed for the films prepared by sandwich casting, while a

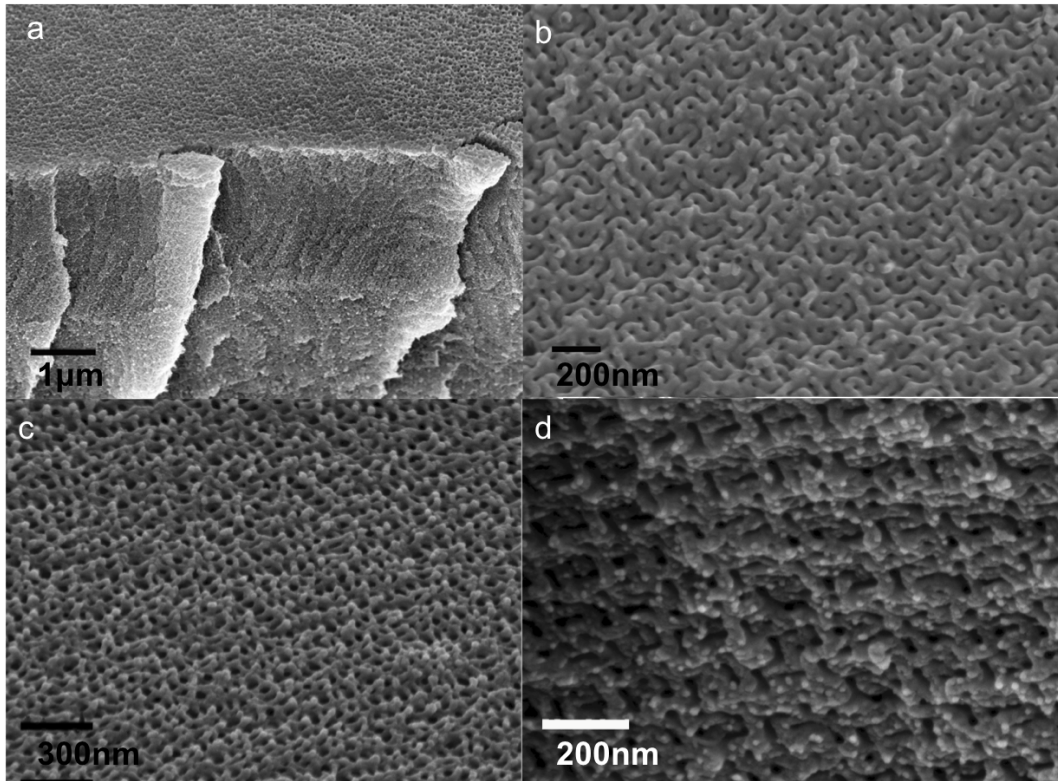


Figure 4.3: Collection of SEM representations of gyroid templates. (a) cross-sectional view (using a substrate holder at 45°) (b)(c)(d) different faces of gyroid structure within the same film.

much thinner films formed for spin-coated samples. (See **Fig. 4.5** and **Fig. 4.6**) The thickness of the top layer varied from sample to sample, but since the total thickness of the film also varied widely using this deposition method, no systematic correlation with the top layer formation was found. Further discussion is presented in Chapter 3.2 using spin-coated films of wormlike morphology. The non-porous top layer was removed by oxygen plasma etching. Depending on the thickness of the layer, up to 2 minutes of plasma etching was required. It was found that even if the starting surface topography was smooth (**Fig. 4.5 c**), O_2 plasma treatment for 1 minute lead to a very rough surface. (**Fig. 4.5 d**).

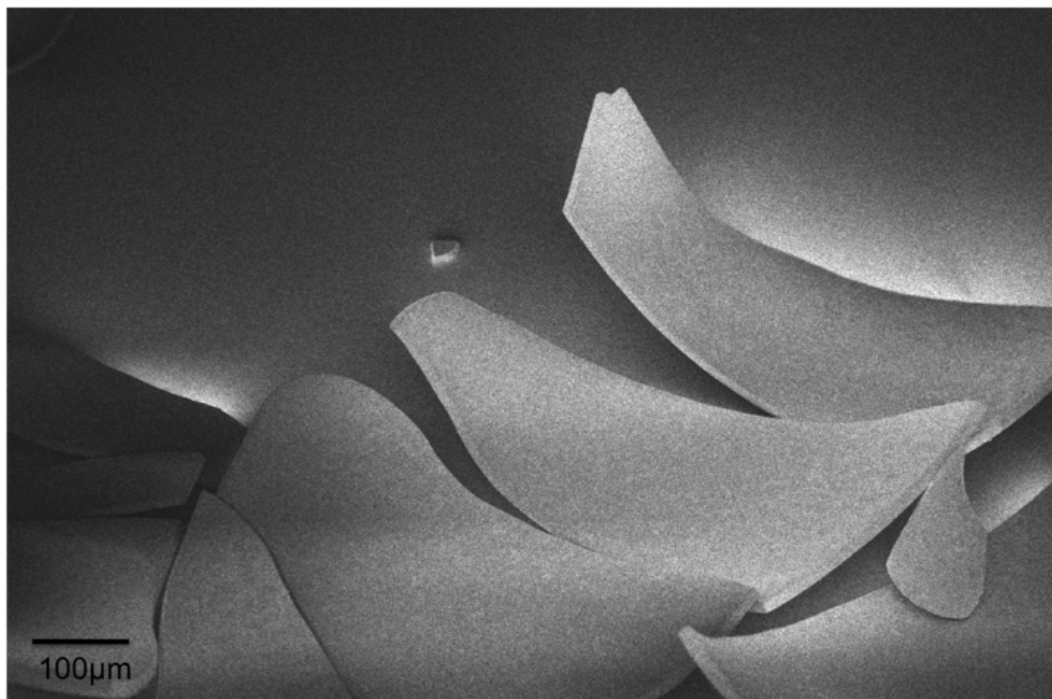


Figure 4.4: SEM representation of peeling and cracking of the gyroid template after EtOH etching of PI block

Gyroid Fabrication by Spin Coating

In an attempt to overcome the challenges of the sandwich casting method (uncontrollable thickness, peeling and cracking), an alternate route was investigated. When optimised, the spin-coating process can generate films with smooth surfaces and highly controllable thickness. The benefits of this deposition method make it ideal for fabrication of polymer templates. However, the fast solvent evaporation kinetics of spin coating is in conflict with the equilibrium nature of gyroid formation. **Fig. 4.6** shows examples of films prepared by spin coating using the same solution as that used for gyroid formation. These films exhibit wormlike morphology with no long-range order, and a smooth film surface over the entire span of the film (1.2cm \times 1.2cm). The surface roughness of the final film (after the etching step) measured by AFM was 15 nm. (**Fig. 4.7**). No peeling or cracking was observed for films as

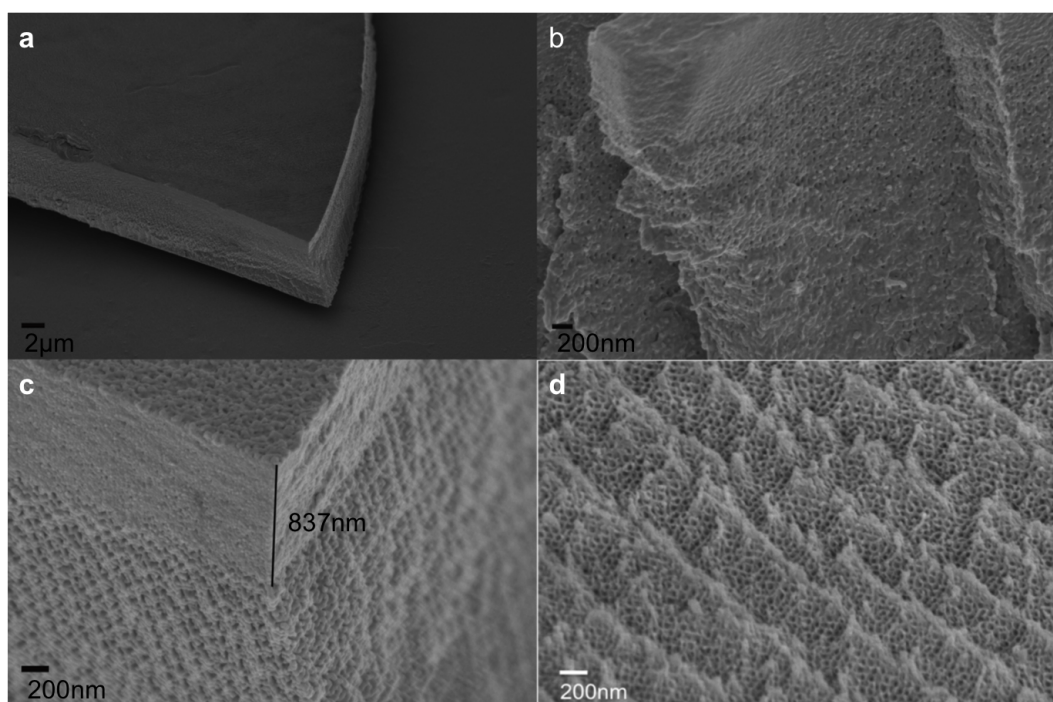


Figure 4.5: (a) Gyroid film with a thick non-porous top layer, (b) both non-porous top layer and blocked pores due to inadequate EtOH etching, (c) zoomed image of (a), (d) top surface of the film after O₂ plasma etch of the top layer

thick as 4 μm. This could be attributed to the fact that the wormlike morphology lacks long-range order, whereas gyroid arranges into multidomain crystals, which makes the film prone to cracking along a certain crystal orientations.

The spin-coated film, which is frozen in at a non-equilibrium state, can be driven into the gyroid phase by a subsequent solvent annealing step. After spin coating, the film was left in a sealed chamber under a solvent-rich environment for up to 7 days, in order to allow the polymer system to rearrange and reach equilibrium. In the film after solvent annealing for 72 hours (**Fig. 4.8 a**), cylindrical and lamellar morphologies appeared, but no gyroid or wormlike morphology was found in sampled areas. After 7 days, cylinder, lamellae, wormlike and gyroid morphologies were all found in different parts of the same film. (**Fig. 4.8 b, c, d**). As a result of the solvent annealing process, film quality in terms of surface roughness and thickness

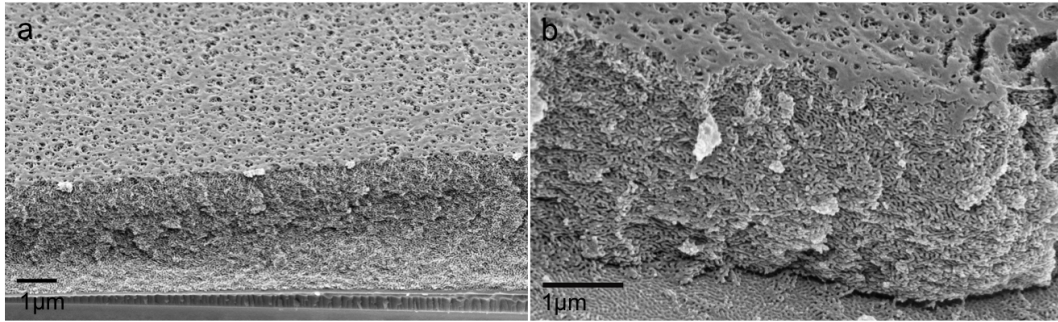


Figure 4.6: (a) SEM image of spin coated film using the gyroid forming mixture used for producing films shown in **Fig. 4.3**, (b) zoomed image of (a). After removal of PI block, a 3D porous wormlike structure was observed.

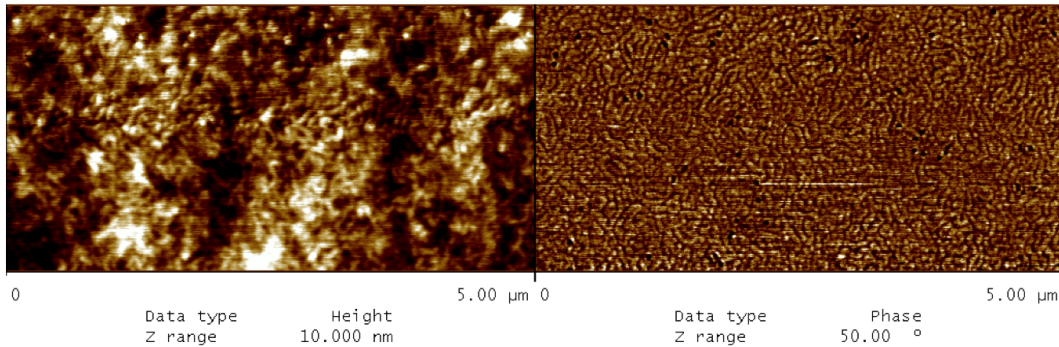


Figure 4.7: AFM image of the top surface of the wormlike film after EtOH etching. Uniformity was significantly degraded. During solvent annealing, the solvent vapour diffuses into the polymer film, mobilising the polymer chains and allowing them to re-arrange into a more thermodynamically favourable state, which might not result in a smooth film surface. It is foreseeable that by increasing the annealing time for even longer or investigating alternative post deposition annealing conditions, gyroid-only thin films can be achieved. However, in the context of developing a versatile route to create porous templates, this might not be very practical in terms of fabrication time and consistency.

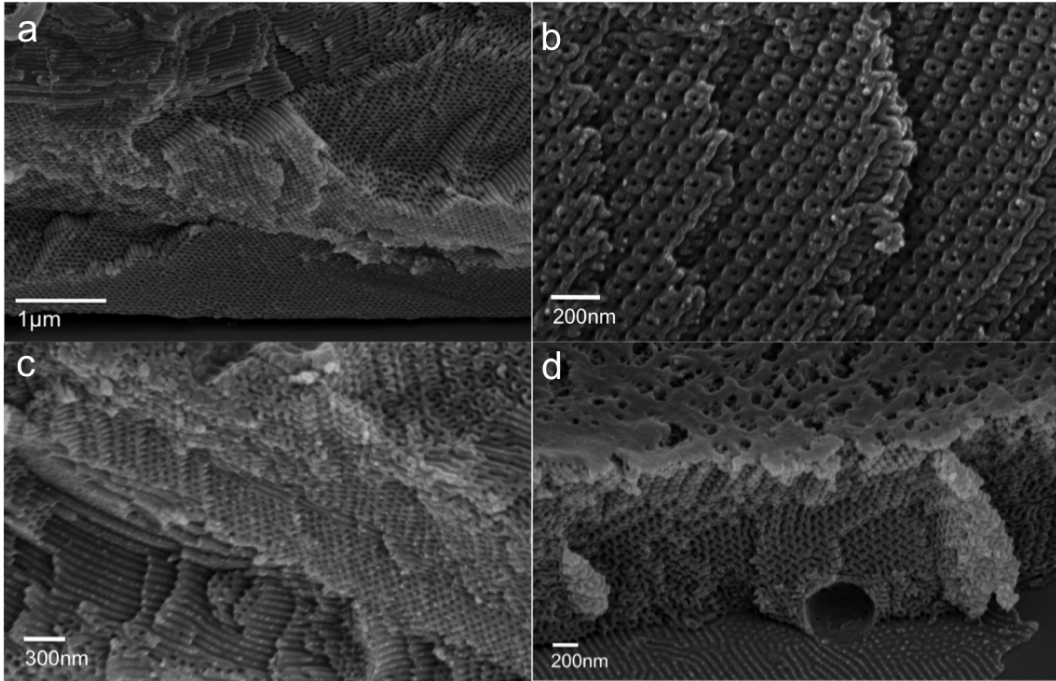


Figure 4.8: Spin coating followed by solvent annealing for 7 days. Combination of cylinder (a) (c) and gyroid morphologies (b)(c)(d) were observed in different parts of the same film.

4.3.2 Wormlike Structure

As discussed in Section 3.1.2, spin coating the gyroid-forming mixture leads to fast evaporation of the solvent, quenching the system in a nonequilibrium state. Under these conditions, the spin coated polymer mixture was found to microphase separate into a wormlike morphology with feature sizes of 25-40 nm. This porous film, while lacking the periodicity of the gyroid morphology, remains suitable for many applications, which require porous structures and/or a high internal surface area to volume ratio, provided that the pores are interconnected throughout the film. This approach provides the benefits of simpler and quicker processing conditions, consistency in film quality, and control over film thickness. In addition, the lack of long-range order makes the films less prone to cracking and peeling.

These kinetically trapped wormlike structures have been found to be bicontin-

uous in different BCP systems.^[9] In order to check that these templates are have interconnected pores, ZnO was deposited by ALD onto the substrates (see Chapter 5), and it was observed that the deposition was conformal throughout the film all the way down to the substrate. (See Chapter 5) This indicates that the pores are interconnected, allowing the ALD precursor molecules to diffuse throughout the film. Upon removal of the polymer by thermal annealing at a temperature above 400°C or oxygen plasma treatment for 20-60 minutes, a self-standing ZnO replica film was obtained.

Controlling the Thickness

The thickness of the polymer template films is primarily dependent on the concentration of the polymer in the solution, and the spin coating parameters such as spin speed, acceleration, and duration. The thicknesses resulting from various experimental conditions are summarised in **Fig. 4.10** . The window of spin speeds for the polymer solutions that resulted in a good film quality was found to range from 750 rpm to 2000 rpm, depending on the polymer concentration. For higher polymer concentrations ($>7\%$), a minimum of 1000 rpm was required to obtain a smooth film. Varying the spin speed at a fixed concentration provided a fine adjustment, altering the thickness by 50 to 100 nm, whereas varying the concentration of the polymer resulted in thickness changes of hundreds of nanometers. **Fig. 4.9** shows the SEM images of the polymer films prepared with 4 different concentrations and spin coated with the same speed, resulting in varying thicknesses. Expectedly, as the film thickness increased, some cracks were found especially close to the edges of the film, but no dramatic peeling as in the case of the gyroid samples was observed.

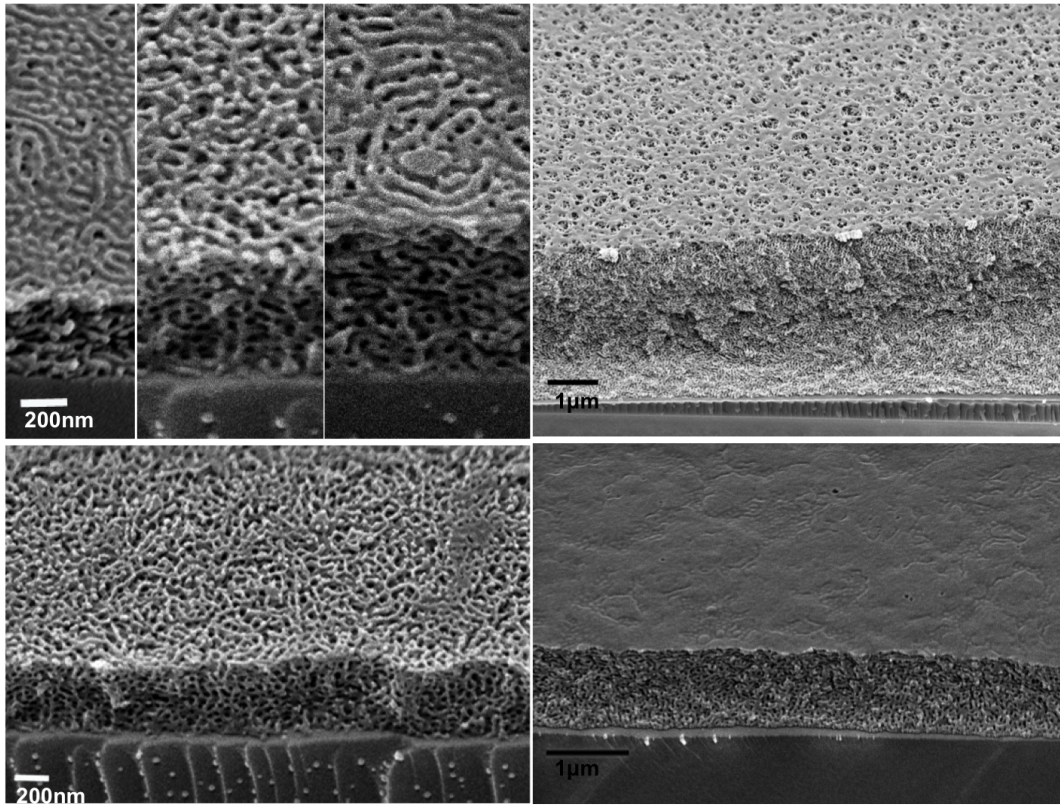


Figure 4.9: SEM image of wormlike morphologies of various thicknesses using the same polymer solution with different concentrations: (a) 5% (b) 7% (c) 8.5% (d) 17%

Effect of UV treatment

Selective etching of the polyisoprene minority block first requires degradation of the PI by UV exposure. Treatment under UV between 12 and 48 hours has been used for degradation of PI in a bulk PS-PI gyroid^[10]. Because the gyroid films fabricated in the previous section had thickness of over a micrometer, similar protocols were appropriate. However, for thin film systems of less than one micron, this duration of UV treatment was found to be excessive. As shown in **Fig. 4.11 e and f**, after 12 hours of UV exposure, the entire film including the polystyrene fraction became etchable by EtOH. Therefore, it was important to find an exposure window where

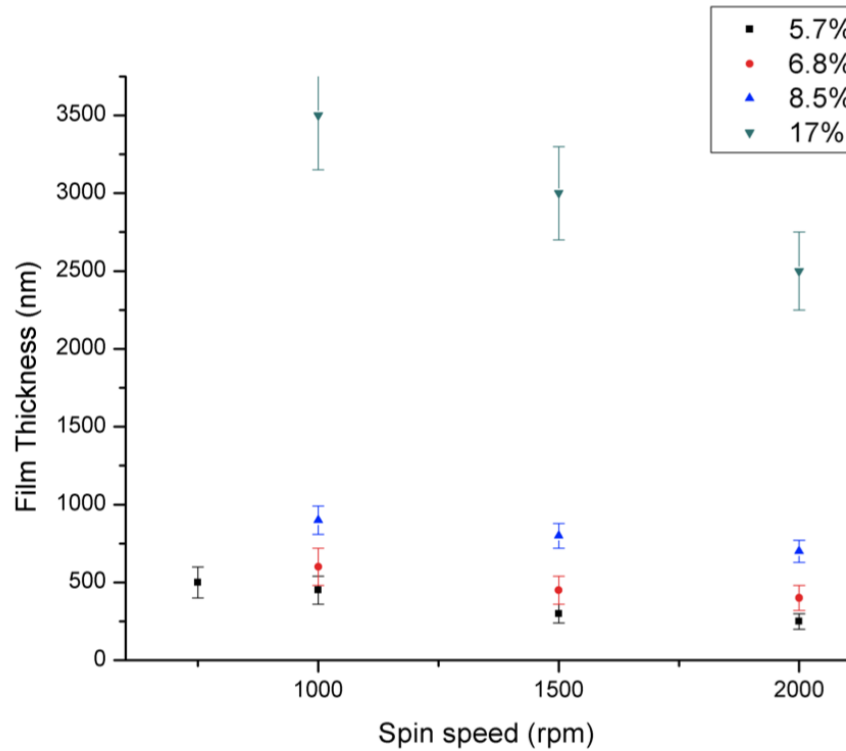


Figure 4.10: Summary of thickness of the films as a function of spin speed

the PI is fully degraded but the PS does not become etchable by ethanol. Intuitively, one might expect that a shorter UV exposure time should be required for thinner films to selectively degrade the PI. This is borne out by the experimental results. For example, 4 hours of UV time appeared insufficient for films thicker than 600nm as the PI backbone did not seem to be fully cleaved, judging by some blocked pores observed from SEM images. As shown in **Fig. 4.11 a, c and e**, for the films of equivalent thickness (400nm) and the same ethanol etching time, the UV exposure of 2, 4, and 12 hours resulted in different films. The same principle could be applied for films of different thickness, and the optimum UV exposure times for different thicknesses based on experimental observations are summarised in **Fig. 4.12**.

The spin-coated films also often exhibited a dense, non-porous layer at the surface

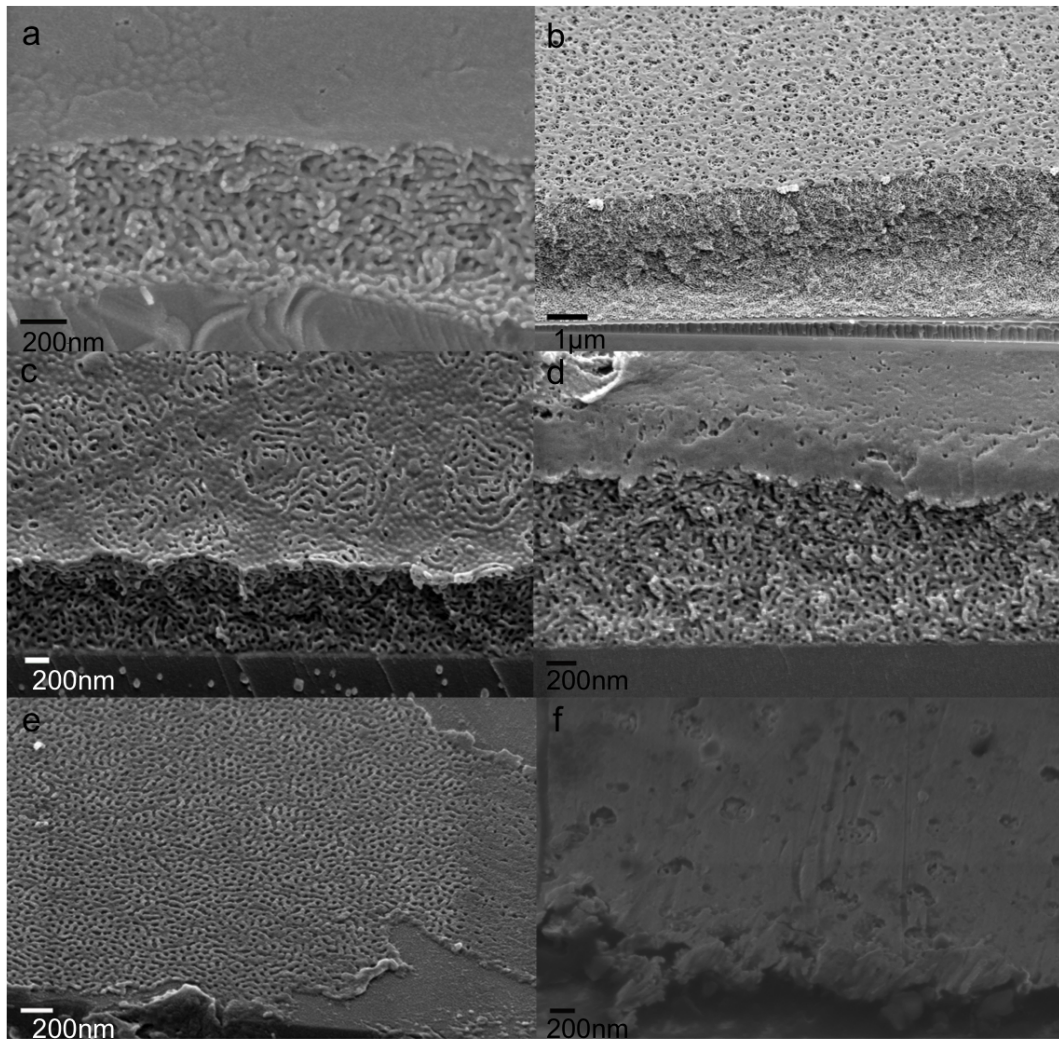


Figure 4.11: Films prepared by different polymer concentration (resulting in different thickness), UV exposure times, after 12 hours of EtOH etching (a) 500 nm-thick film, 2 hrs UV (b) 2 micron-thick film, 12 hrs UV (c) 500 nm film (same as (a)), 4 hrs UV (d) 900 nm film after 4 hrs UV (e) 50 nm film (same as that shown in (a) and (c) after 12 hrs UV (f) 900 nm film after 12 hrs UV.

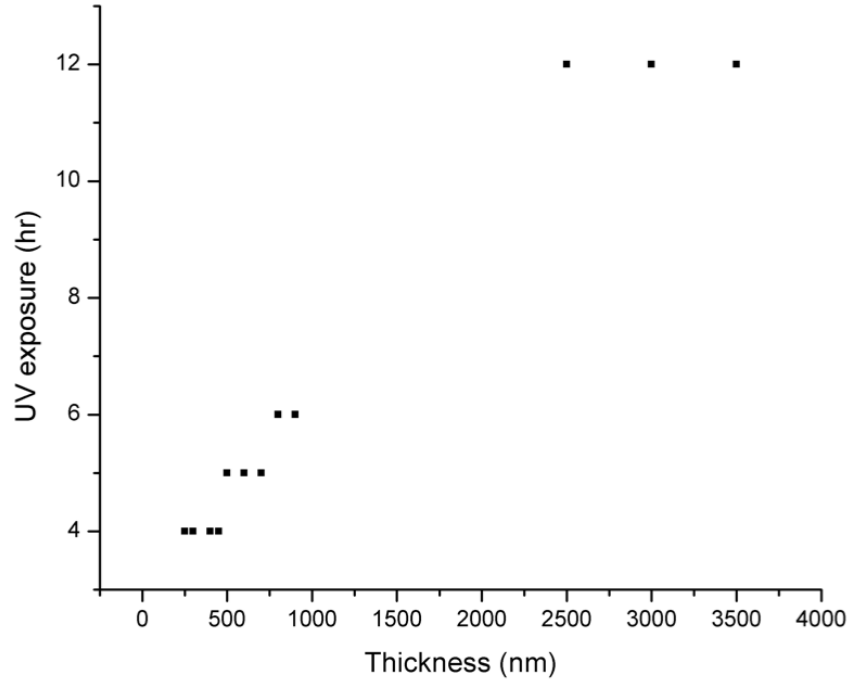


Figure 4.12: Summary of optimal UV exposure time to obtain films with open pores at the substrate surface.

of the film. This layer is qualitatively similar to that of the gyroid films prepared by sandwich casting, but in this case the thickness of the top layer ranged only from a few nm to 100 nm. In general, under equivalent processing conditions, the thickness of the spin-coated top layer was proportional to the overall film thickness. Some thinner films (300-400 nm) already had an open porous surface before plasma etching, as shown in **Fig. 4.12**, while others had a solid layer of varying thickness.

Based on these experiments, the mechanism for the removal of the dense surface layer can be hypothesized as due to UV degradation of the surface PS as well as the interstitial PI. Upon exposing PS to UV, formation of chemical groups associated with hydrophilic nature including hydroxyl (-OH), the carbonyl (C=O) and C-O-

groups has been observed.^[11]^[8]

Therefore, depending on the amount of UV exposure, the PS at the surface is more soluble in EtOH. After an optimal duration of UV irradiation, the dense homopolymer layer at the top, which has thickness for sub-micron samples comparable to the length scale of the film porosity, was degraded, which leads to an open porous surface upon EtOH treatment. In order to confirm this hypothesis, a 350 nm-thick PS homopolymer (M=100K) was prepared by spin coating and subjected to 12 hours of UV exposure followed by 6 hours of EtOH. The thickness of the film, which was measured by spectroscopic ellipsometry, decreased to 28nm. This confirms that UV exposure can cause dissolution of PS in EtOH.

Selective chemical etching of polyisoprene block to create pores

Following the backbone cleavage of the polyisoprene block, it becomes selectively soluble in ethanol. According to the experimental results of fabricating thick gyroid films, an immersion time of typically over 12 hours was needed in order to dissolve all of the polyisoprene. Upon SEM examination of the samples, the same amount of time was also required for films with thicknesses in the sub-micrometer range. For all the films under a thickness of 400 nm, after 6 hours of immersing the film in ethanol, no residual PI was observed from any of the sampled areas. However, for films thicker than 400 nm, undissolved PI was observed in some parts of the film as displayed in **Fig. 4.13**. Wang *et al.* found that immersion of PS in ethanol swells the polymer and results in changes of feature size, to a degree dependent on the duration of immersion. In our case, the PS structure remained unchanged from 6 to as long as 15 hours of immersion.^[9] Therefore, the samples were typically left immersed overnight to ensure that PI was completely etched away and dried before storing for a prolonged period of time.

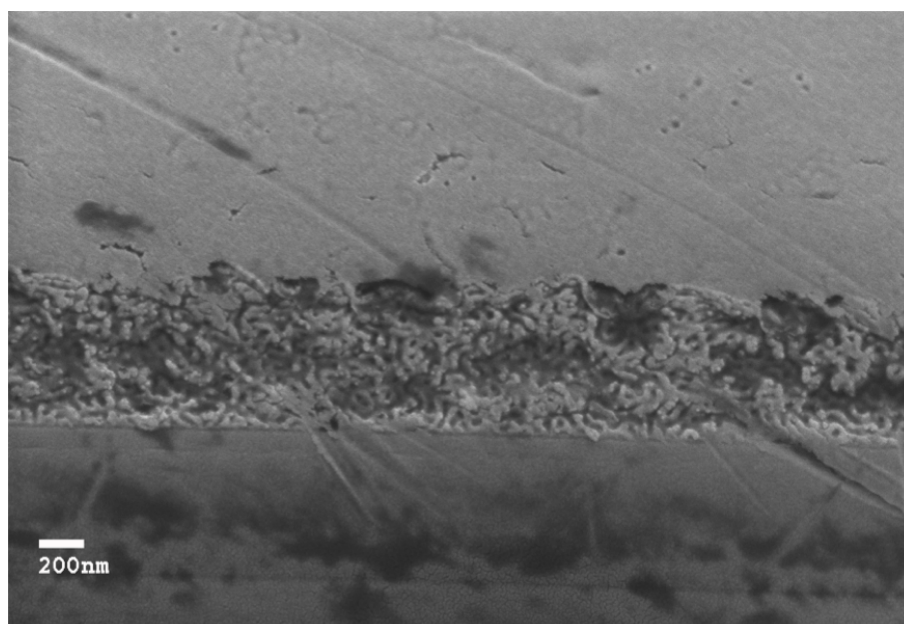


Figure 4.13: Blocked pores due to insufficient UV exposure or EtOH etching

Removal of non-porous top layer of the film

The removal of any top layer that remained after etching simply required a short oxygen plasma treatment of less than 30 seconds. Even for the films with a porous top, 10 to 20 seconds of plasma treatment resulted in complete exposure of the pores (**Fig. 4.14**), which allows easier infiltration of the guest material into the template.

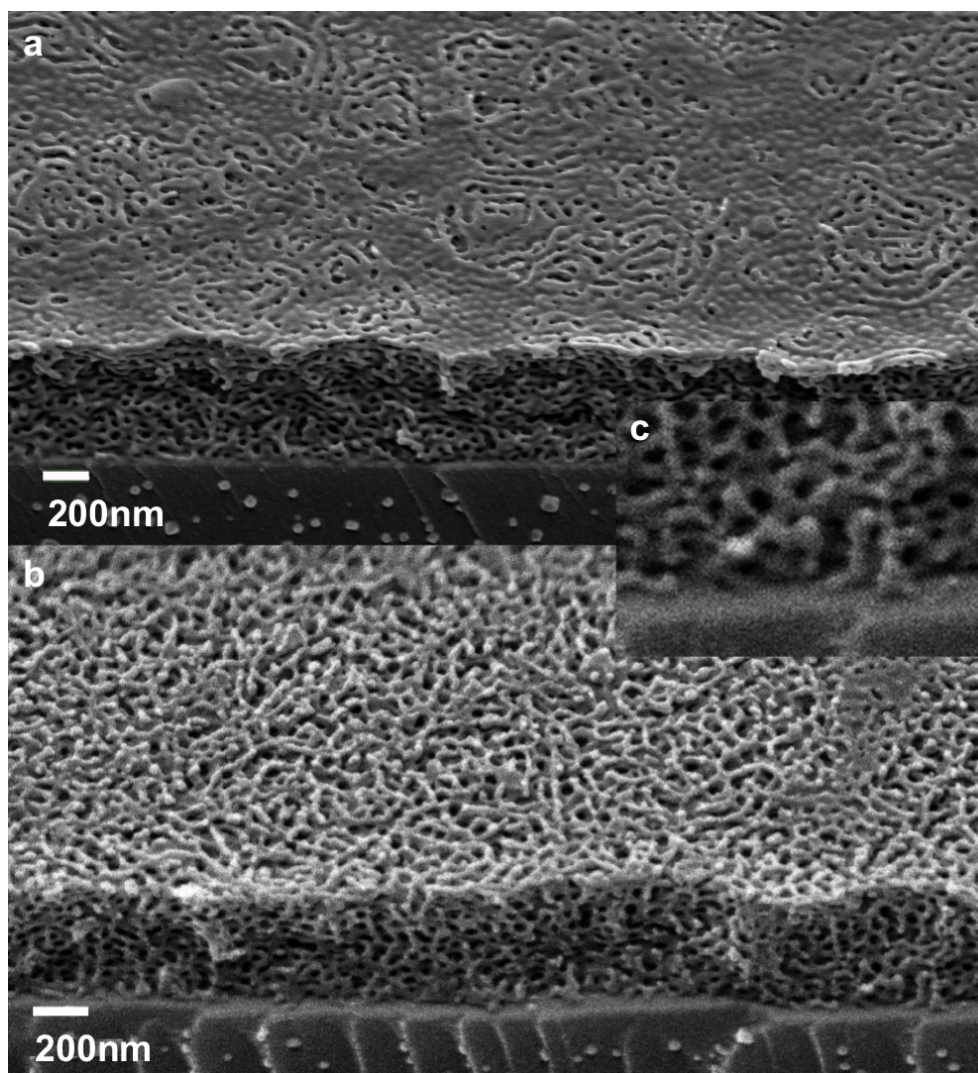


Figure 4.14: (a) a wormlike film prepared using an optimised protocol with some compact top layer present, (b) the same film after 10 s of O₂ plasma etching, (c) zoomed image of (b) showing good porosity at the substrate-film interface

4.4 Conclusions

In this chapter, we have established a systematic, reliable route to fabricating 3D bi-continuous polystyrene film templates with pore sizes of 20 nm under either equilibrium conditions or non-equilibrium conditions with thickness ranging from 250 nm to 4 μ m. Both architectures bear distinct advantages and disadvantages that require careful consideration based on the design requirements of the application. The processing variables used in preparing the porous template were optimized. A few conclusions can be drawn:

- Gyroid thin films were made through sandwich casting and spin coating followed by solvent annealing. However, the resulting film suffered from cracks and peeling. The reason for this could be that a large amount of stress built up during PI etching by EtOH and the crystallinity of the gyroid could make the film more prone to cracks.
- Controlling film thickness while maintaining film quality is achievable by varying the concentration of the polymer solution when changing the thickness by more than 200 nm. However, adjusting the spin-coating parameters, in particular the spin speed provides a useful handle for varying the film thickness by amounts less than 200 nm.
- The UV treatment of the spin-coated films degrades the backbone of PI as well as cross-linking the polystyrene and rendering it hydrophilic at the same time. Overexposure to UV also degraded the polystyrene template and made it soluble in ethanol. The optimal amount of time for UV exposure depended on the thickness of the films and is summarized in **Fig. 4.12**.
- The duration of longer than 12 hours for EtOH etching time was required for completely removing polyisoprene from the film. SEM was utilized to confirm complete removal of polyisoprene block.

Bibliography

- [1] Hsueh, H. and Ho, R. (2012) Bicontinuous ceramics with high surface area from block copolymer templates. *Langmuir*, **28** (22), 8518–8529. [57](#)
- [2] Crossland, E., Kamperman, M., Nedelcu, M., Ducati, C., Wiesner, U., Smilgies, D., Toombes, G., Hillmyer, M., Ludwigs, S., and Steiner, U. (2008) A bicontinuous double gyroid hybrid solar cell. *Nano letters*, **9** (8), 2807–2812.
- [3] Wei, D., Scherer, M., Bower, C., Andrew, P., Ryhnen, T., and Steiner, U. (2012) A nanostructured electrochromic supercapacitor. *Nano letters*, **12** (4), 1857–1862.
- [4] Scherer, M., Li, L., Cunha, P., Scherman, O., and Steiner, U. (2012) Enhanced electrochromism in gyroidstructured vanadium pentoxide. *Adv. Mater.* [57](#)
- [5] Finnemore, A.S., Scherer, M.R.J., Langford, R., Mahajan, S., Ludwigs, S., Meldrum, F.C., and Steiner, U. (2009) Nanostructured calcite single crystals with gyroid morphologies. *Adv. Mater.*, **21** (38â39), 3928–3932. [57](#), [58](#)
- [6] Crossland, E., Cunha, P., Scroggins, S., Moratti, S., Yurchenko, O., Steiner, U., Hillmyer, M., and Ludwigs, S. (2010) Soft-etch mesoporous hole-conducting block copolymer templates. *ACS nano*, **4** (2), 962–966. [58](#)
- [7] Scherer, M. (2008), Nanostructured materials via self-assembled templates. [59](#), [60](#), [61](#), [62](#)

- [8] Blach, J.A., Watson, G.S., Busfield, W.K., and Myhra, S. (2001) Photo-oxidative degradation in polyisoprene: surface characterization and analysis by atomic force microscopy. *Polym. Int.*, **51** (1), 12–20, doi:10.1002/pi.780. [62](#), [73](#)
- [9] Wang, Y., He, C., Xing, W., Li, F., Tong, L., Chen, Z., Liao, X., and Steinhart, M. (2010) Nanoporous metal membranes with bicontinuous morphology from recyclable block-copolymer templates. *Adv. Mater.*, **22** (18), 2068–2072, doi:10.1002/adma.200903655. [68](#), [73](#)
- [10] Urbas, A., Maldovan, M., DeRege, P., and Thomas, E. (2002) Bicontinuous cubic block copolymer photonic crystals. *Adv. Mater.*, **14** (24), 1850–1853. [69](#)
- [11] Zhang, D., Dougal, S., and Yeganeh, M. (2000) Effects of uv irradiation and plasma treatment on a polystyrene surface studied by ir-visible sum frequency generation spectroscopy. *Langmuir*, **16** (10), 4528–4532. [73](#)

Chapter 5

Fabrication of 3D Mesoporous ZnO via Atomic Layer Deposition

5.1 Introduction

ZnO is a direct semiconductor with a wide bandgap of 3.37 eV with piezoelectric, photocatalytic, and gas sensing properties.^[1] In its thin film form, it is used as a transparent (semi)conductive electrode for optoelectronic and solar cell applications.^[2] In addition, three-dimensional, porous structures of ZnO have been of technological interest in emerging areas of nanotechnology as they offer opportunities for applications that require a high surface area or hybrid materials.

Unlike other transition metal oxides such as TiO₂, and SnO₂ and despite equally desirable properties, few reports exist successfully realising well-defined porous ZnO structures on the 20 nm length scale. Instead, 3D structures of ZnO were based on introducing different crystal growth sites and anisotropically growing one-dimensional ZnO demonstrated by the examples of ZnO nanorods, nanowires, nano coils, nano-forests.^[3-5] This is mainly attributed to the difficulties involved in controlling the tendency of ZnO to rapidly crystallise at relatively low temperatures. Therefore,

the conventional sol-gel methods or electrodeposition methods have not been successful for creating a well-defined three dimensional structure of ZnO on the length scale of 20-40 nm. Reports on porous ZnO structures using such methods have pore sizes larger than 200 nm^[6] or have a poorly defined morphology.^[7,8] In this work, the problems of the rapid crystallization behaviour of ZnO was alleviated by combining blockcopolymer (BCP) microphase separation and atomic layer deposition (ALD). We introduce a systematic method of fabricating 3D bicontinuous structures of ZnO with feature sizes on the sub-50 nm length scale and controllable thicknesses ranging from 200 nm to several microns.

As discussed in the previous chapters (Chapter 2 and Chapter 4), due to their desirable self-assembled morphologies, BCPs have been utilised to pattern metal oxides either as a direct structure guiding material^[9] or as a sacrificial template for metal oxide materials via electrodeposition^[10] or solution impregnation^[11].

Alternatively, atomic layer deposition (ALD) allows three dimensional, conformal replication of the polymer substrate in a more controlled manner compared to conventional solution processing methods. Successful 3D deposition requires more careful consideration of processing parameters such as exposure time, precursors partial pressure, deposition temperature and the aspect ratio and surface chemistry of the non-flat substrates. Several models and simulation methods were suggested to describe conformal deposition onto substrates of high aspect ratios (>10000) such as alumina membranes (AAO), nanotubes or inverse opals.^[12-14] Wang *et al.* reported the deposition of ZnO onto a complex polymer structure of tubular shape.^[15]

Despite the fact that both BCP templating, and ALD have been utilized for 3D metal oxide fabrication, it has remained a challenge to establish a simple, reliable 3D ZnO material system which has a systematic, controllable thin film processing route and a demonstrated application. In this study, we report a method for the preparation of highly periodic mesoporous structures of ZnO by replicating a self-

assembled polymer substrate using the ALD, maximally exploiting the advantages of the two systems. Starting with a porous template obtained by self assembly of BCP followed by a selective etching of the minority phase (detailed in Chapter 4), ZnO was conformally coated by exploiting ALDs ability to conformally coat complex 3D surfaces of high aspect ratios, the gyroid morphology of a self- assembled block copolymer template was replicated by ZnO. The application of this material is demonstrated in a solar cell application.

5.2 Experimental

Template fabrication

The polymers used for template fabrication were Polystyrene (45 kg/mol)-*block*-polyisoprene (39 kg/mol), purchased from Polymer Source Inc., Canada, and polystyrene (10 kg/mol), purchased from Sigma Aldrich. PS-*b*-PI and PS were mixed to result in 65% volume fraction of PS and dissolved in toluene. In order to fabricate a self assembled gyroid structure, 20l of solution was drop cast onto a substrate (Si, ITO, or glass) of 1.2cm × 1.2cm. A PTFE film of 1cm × 1cm was placed onto the middle of the drop and the film was placed in a sealed chamber with a toluene-rich atmosphere at 4°C for upto 7 days. For a wormlike structure, 60l of the mixed polymer solution was spin coated onto a substrate at 1000/1000 rpm/acceleration for 90 seconds. The film was then taken out of the chamber and left in the air at room temperature for an additional 24 hours before being exposed to UV (254 nm) for 12 hours in order to degrade the polyisoprene block. The poly isoprene block was then removed by placing the film in ethanol solution for 15 hours. In order to minimise peeling and cracking of the film, the film was placed upside down on a lint-free tissue and dried.

ZnO replication

A Beneq system was used for ALD deposition. The precursors for ZnO deposition

were diethyl zinc ($(C_2H_5)_2Zn$), purchased from ABCR GmbH Co. KG, and deionized water (H_2O). Deposition cycles ranged from 65 to 250 cycles. Although numerous variations of recipes were tried, typical pulse/purge times for continuous flow method were 30 s for the first 30 cycles, 1 minute for the second 40 cycles, and 2 minutes for the third 30 cycles. A typical half cycle of stop-flow recipe included a 10 s pulse, 1 minute hold time with the vacuum and nitrogen flow off, and purging for 1 minute. Deposition was normally carried out at 80 °C, but for depositions at 100 °C and 120 °C were made for comparison.

Removal of PS template

The deposited ZnO- polymer hybrid was then exposed to either oxygen plasma (Diener Plasma Etcher) or calcination at a temperature above 400°C. For sufficient PS removal, a duration between 15 minutes and 45 minutes, of oxygen plasma treatment was required, depending on the thickness of the polystyrene. For a temperature removal of PS, the samples were heated up (ramp: 10 °C/minute) to a temperature above 400°C and annealed for 2 hours in air.

Etching of compact ZnO layer

An inductive coil plasma(ICP) etcher (Oxford Instrument) was used to etch the top nonporous layer of ZnO. 6 minutes of etching removed the 30 nm nonporous layer. The etchant used were CHF_3 (50 ccm) and Ar (25 ccm) using RF power of 100 W and forward power 1550 W.

X-ray Diffraction

Wide angle x-ray scattering (WAXS) measurements, were carried out using a Bruker D8 diffractometer. The samples were prepared on a Si substrate.

X-ray photoemission spectroscopy measurements

The gyroid ZnO samples were fabricated on SiO_2 -coated Si and transferred to the ultrahigh vacuum (UHV) chamber (ESCALAB 250Xi) for XPS measurements. The measurements were carried out using a XR6 monochromated Al α x-ray source ($h\nu$

= 1486.6 eV) with a 650 m spot size. For the XPS depth profiling, the Ar ion gun etching was performed using ion energy of 3000 eV.

Photovoltaic device fabrication

The worm-like ZnO structures were fabricated on prepatterned ITO/glass substrates as described above. The poly(3-hexylthiophene) (P3HT) (from Reike Metals) polymers was dissolved in anhydrous chlorobenzene and spin-coated on the ZnO mesoporous layer. The samples were then transferred to a thermal evaporation chamber for WO₃ (10 nm), Ag (30 nm), and Al (60 nm) deposition under high vacuum (10⁻⁶ mbar). Finally, the devices were post-annealed at 140 °C for 10 mins.

Photovoltaic performance characterization

For External Quantum Efficiency (EQE) measurements (in air) a 250 W tungsten halogen lamp and an Oriel Cornerstone 130 monochromator were used. The measurements were performed as a function of wavelength at intensities ~ 1 mW/cm². To measure the $J - V$ curve of the device under AM1.5 conditions, an ABET Solar 2000 solar simulator was used. In order to obtain reliable data, a spectral mismatch correction was carried out using a calibrated and certified inorganic solar cell.

5.3 Results and Discussion

5.3.1 Mesoporous ZnO structures preparation

5.3.1.1 Polymer templates

Fig. 5.1 demonstrates the sample preparation process. The mesoporous polystyrene templates (gyroid and wormlike) used for ALD replication of ZnO are shown in **Fig. 5.2a** and **Fig. 5.3a**. The UV exposure involved in the preparation process of these templates (as detailed in Chapter 4) not only breaks down the backbone of the PI creating the voids within the film, but also creates carboxylic groups on the PS.^[16]

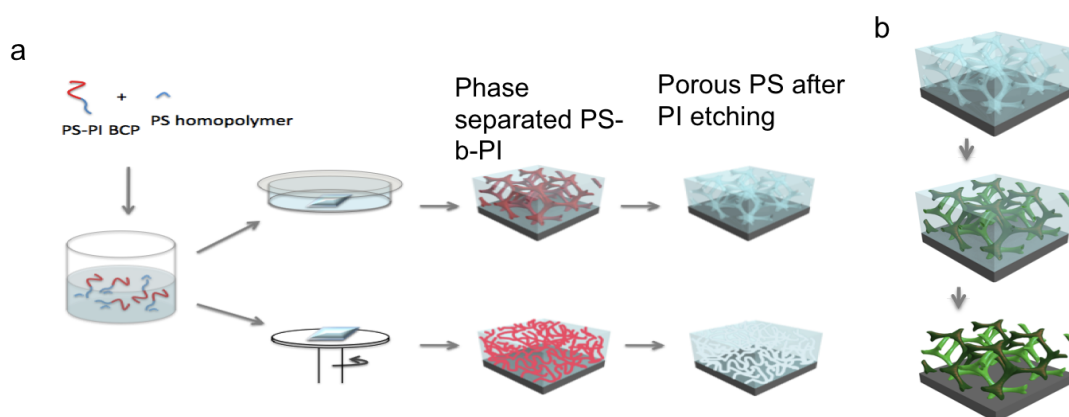


Figure 5.1: Schematic representation of sample preparation procedure. (a) Porous PS template is created via phase separation followed by selective etching polyisoprene block. (b) Replication of the polymer template with ZnO via ALD.

Thus, upon ethanol etching of PI, the polystyrene surface is left rich in OH groups, which is crucial for conformal deposition of ZnO using ALD, which is discussed in more detail later in this chapter.

5.3.1.2 ALD deposition of ZnO onto PS templates

The steps of the replication process illustrated in **Fig. 5.1b** are demonstrated by the scanning electron microscope (SEM) images shown in **Fig. 5.2a, b, c** and **Fig. 5.3a, b, c**. Starting with the template, ZnO was deposited via ALD, followed by removal of the polymer template. The ZnO-polymer hybrid (before removal of the polymer to create a mesoporous ZnO) is shown in **Fig. 5.2b**. The polymer template and the area where insufficient ZnO was deposited appear dark or charging when characterized by scanning electron microscopy (SEM) because the polystyrene template is not conductive.

The diameter of the void channels running through the polymeric template was estimated to be roughly 32 nm for gyroid, and 25-35nm for wormlike structure. Given that the growth rate of ZnO is reported to be approximately 1.5 Å- 2.2 Åper

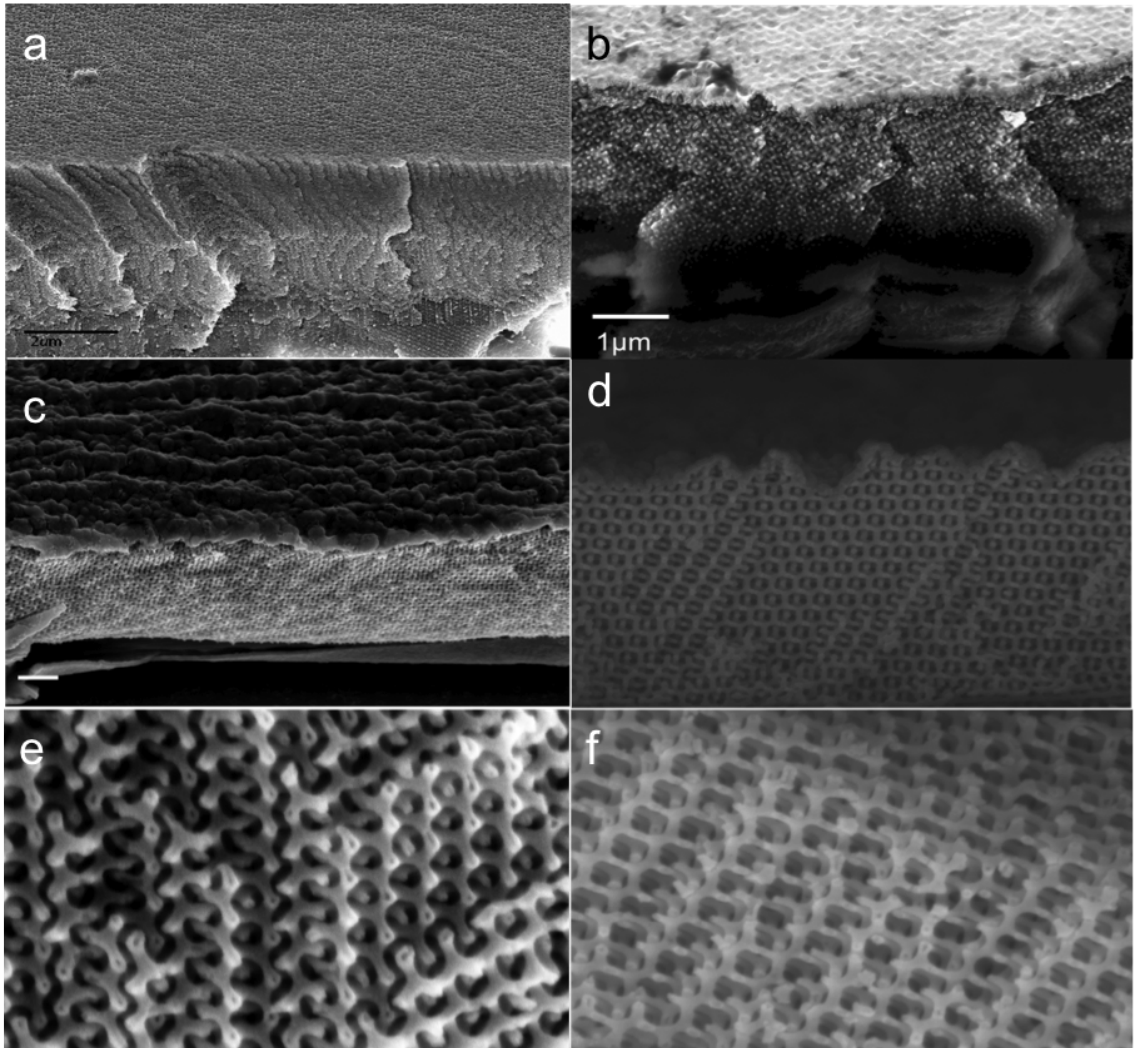


Figure 5.2: SEM representation of gyroid ZnO fabrication process. (a) Gyroid polystyrene template (b) as deposited ZnO-PS hybrid (c) ZnO gyroid film after temperature annealing at 550°C and (d), (e), (f) different faces of ZnO gyroid observed in the films after temperature annealing at 550°C.

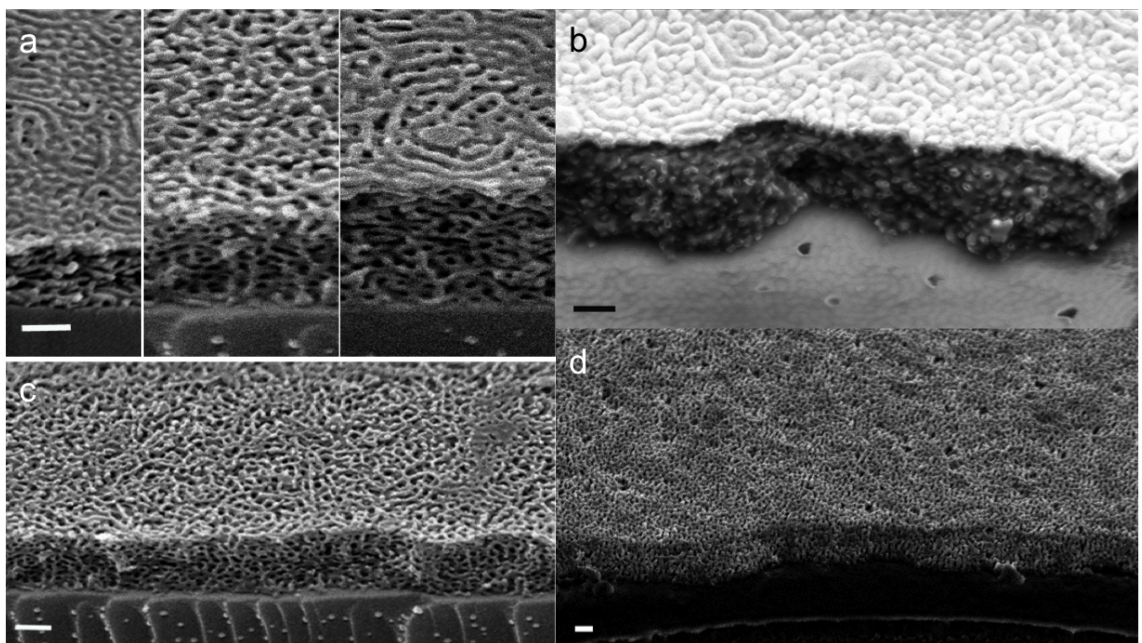


Figure 5.3: SEM representation of gyroid ZnO fabrication process. (a) (c) wormlike polystyrene template (b) as deposited ZnO-PS hybrid (d) ZnO gyroid film after temperature annealing at 400 °C followed by ICP etching of the top compact layer. All scale bars are 200 nm.

cycle^[6,17], 110 cycles of ZnO were deposited in order to aim for a minimum of 16.5 nm deposition on the template surface, which under the assumption of conformal coating would sufficiently fill the void. The thin solid layer on top of the porous film of ~20nm results from the surface limited, conformal deposition, which can easily be removed using dry etching methods such as reactive ion etching (RIE) or inductive coupled plasma (ICP).

The replicated ZnO gyroid film is self-standing and highly periodic with a consistent channel diameter of approximately 30nm. **Fig. 5.2d, e, f** show the gyroid ZnO structure imaged from different angles, thus showing different gyroid faces. Likewise, the wormlike structure is also replicated using the ALD, and using the advantage of being able to control the thickness of the film, 3D bicontinuous ZnO of thin films of thicknesses ranging from 200 nm to 2 μ m were successfully fabricated. (**Fig. 5.3a, c**) This also proves that the wormlike polymer template has interconnected pores. Both types of films were annealed at temperatures between 400°C and 550 °C, and the 3D structures showed stability in this temperature range.

In order to replicate the complex 3D polymer nanostructure into ZnO by ALD, two different types of exposure methods were utilised: the continuous flow method and the stop-flow method, which were closely studied by Karuturi *et al.*^[21]. The exposure times required for successful replication were comparable to what has been reported for high aspect ratio structures: 30 s - 2 minutes for each pulse and purge step and 10 - 20 s exposure with hold times between 1-4 minutes. While both methods have provided a conformal coating of ZnO leading to successful replication of the complex 3D structure, the stop-flow method was proven more practical because pulsing the precursors for up to 2 minutes per cycle would require up to 240 minutes of precursor consumption for each run, whereas the stop-flow method only required between 10-20 seconds of precursor consumption time while the substrate was still exposed to the precursor during the hold period.

Upon subjecting the film to a temperature above 400°C or O₂ plasma treatment, the polymer network within the deposited ZnO was removed, creating a complex 3D ZnO structure, voided gyroid or worm-like. When the deposition did not completely infiltrate through the entire depth of the template (**Fig. 5.2b**), the layer into which ZnO was sufficiently deposited, was observed to settle down onto the substrate upon removal of the polymer without destroying the structure (**Fig. 5.2c**). It is also worth noting that small voids of less than 5nm is observed in the cross section of the ZnO channels **Fig. 5.2e** and **f**, indicating that the precursors did not sufficiently diffuse into the pores because the accessible routes to these pores were closed off.

The incomplete penetration of ZnO through the entire depth of the template could be attributed to several factors. The important factors affecting the conformal coverage include the partial pressure and exposure time of the precursors, aspect ratio of the structure, and the chemistry of the substrate surface.^[12,18] In addition, sufficient purge time of the precursor for each half-cycle is crucial for removing the byproducts as well as the unreacted ones. The unreacted precursor A remaining within the pores can cause chemical vapour deposition (CVD) deposition and block off the pores, preventing the precursor B from further infiltration into the interconnected voids.

Although the deposition kinetics of high aspect ratio systems have been studied both experimentally and theoretically, tube-like substrates with the pore widths >100 nm with the tube length in >10 μ m were normally used, which could provide general insights and guidelines, but cannot be directly applied to our system.^[12-14] Pore blocking and non-uniform coating behaviour when ALD was carried out onto these high aspect ratio substrates has been previously observed.^[19] Even though the aspect ratio of the gyroid is not as high as those in other studies using AAO or inverse opal structures, such problems are not alleviated for several reasons.

Firstly, our 3D bicontinuous substrates have more complex morphologies com-

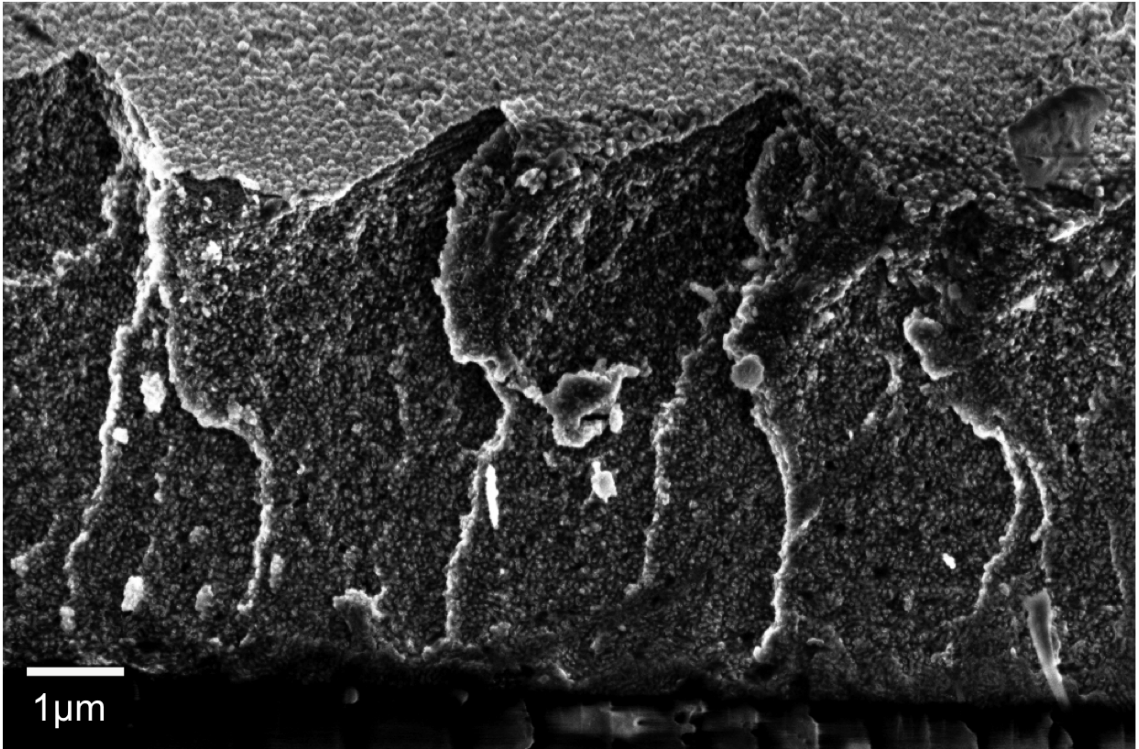


Figure 5.4: Cross sectional SEM image of a wormlike ZnO-PS hybrid. ZnO was deposited conformally onto a $\sim 5 \mu\text{m}$ -thick wormlike structured PS template.

prising numerous interconnected channels. Therefore, this could mean that complete saturation of the substrate surface as well as purging of excess precursors is much more difficult and requires a much longer purging duration despite the lower aspect ratio relative to the ultra-high aspect ratio systems.^[12-14]

In addition, the significantly smaller feature size of this system ($\sim 30 \text{ nm}$) means that unless the deposited material stays either completely amorphous, or extremely fine ($\sim 1\text{-}2 \text{ nm}$) nano-crystalline, throughout the entire deposition cycles, pore blockage due to crystallite formation after ~ 20 cycles (corresponding to $\sim 5 \text{ nm}$ of deposited ZnO). Even if only nano crystalline, this would greatly change the surface roughness within the pores and only amplify as the number of cycles increase. In fact, the XRD results reveal that crystallite formation is observed in ZnO gyroid-

PS, hybrid as deposited without any post treatment, with a crystallite size ~ 8 nm. (**Fig. 5.6**)

In this regard, the abundance of -OH groups on the substrate surface is crucial for creating as many active reaction sites as possible, minimising “cluster formation”.^[20] In our system, during the UV exposure step of the polymer template fabrication, OH, -COOH groups on the polystyrene surface are created^[16], which allows for conformal coating of the polymer surface. According to the SEM image shown in **Fig. 5.5**, uniform initial ZnO coating was observed. However, this does not eliminate the possibility of deposition of multiple layers of precursors, as opposed to a surface terminated process, resulting in over-saturation of the surface caused by prolonged exposure of precursors to the substrate surface. This would be a likely reason for pore blockage.

Increasing the exposure duration by a factor of 2 was tried as an attempt to fill the final few nm of unfilled core of in the gyroid channels, which appears as a void in the SEM image **Fig. 5.2e and f**, but in most of the samples, the unfilled void was observed close to the substrate. The unfilled core of the gyroid channels, suggesting that the pores at the top surface were closed 15-25 cycles earlier than the calculated cycle numbers based on the growth rate. It was observed, as shown in **Fig. 5.5**, that the pores were blocked off after 65 cycles, which corresponds to depositions between 10-15 nm, and the diameter of unfilled voids was roughly between 3-7 nm. By this time, the aspect ratio of the structure has increase by a factor of 10 and further increasing the pulse/purge times became impractical. The substrate closer to the surface is blocked off much too early. There should be a good balance between the precursor amount, exposure time, and partial pressure.

Furthermore, as reported by Urbas *et al.*, removal of PI requires a prolonged period of exposure under UV and ethanol (up to 48 hours for each process).^[21] Therefore, it is a possibility that some residual PI might have remained in the

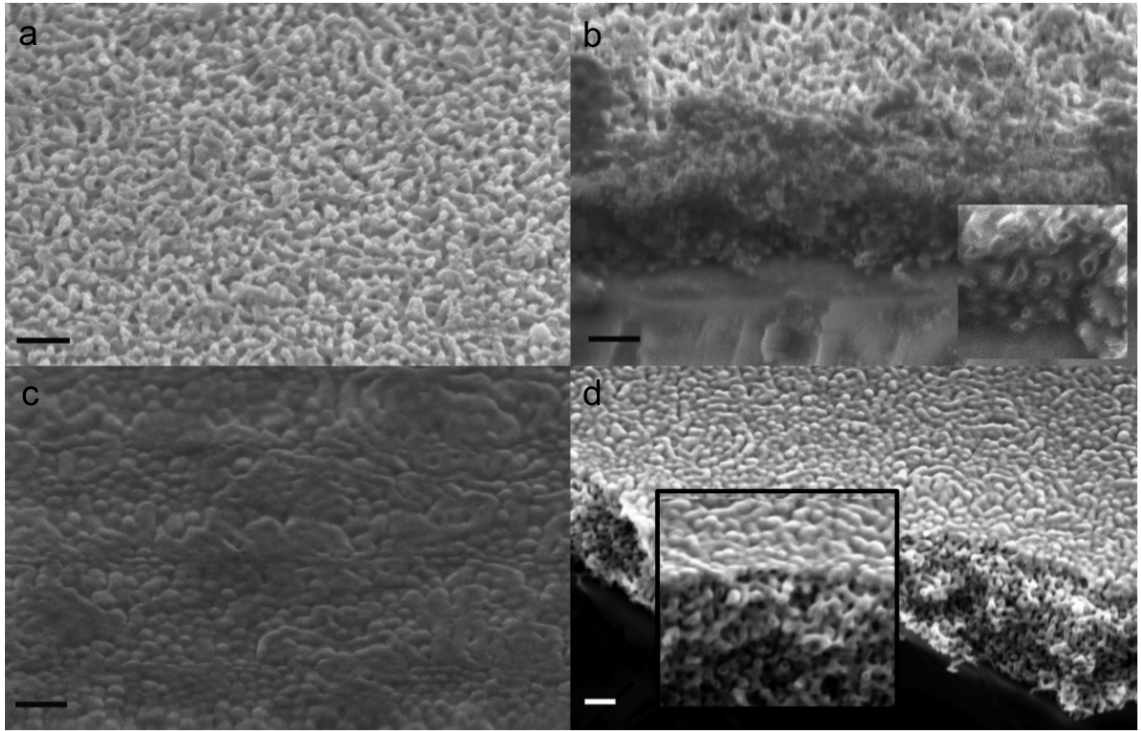


Figure 5.5: ALD of ZnO (a) top layer (b) cross section of ZnO deposited onto the porous template after 30 cycles (c) (d) after 75 cycles. The scale bars are 200 nm.

bottom part of the gyroid substrate, either occupying the void or altering the surface chemistry of the substrate. This is a likely hypothesis, as infiltration up to 5 m depth has been observed (**Fig. 5.4**) using a wormlike structured template under the same deposition conditions. In the thinner polymer template systems ($< 2\text{m}$), such incomplete infiltration leading to settling of entire films was not witnessed, although the few nm-wide unfilled voids still were observed.

5.3.1.3 Deposition temperature

Due to a prolonged deposition time, the template has to withstand the temperature up to 24 hours depending on the thickness and the exposure methods. In order to assess its temperature stability, the templates were left in vacuum for up to 24 hours in temperatures up to 120°C . The crosslinked polymer template was found to

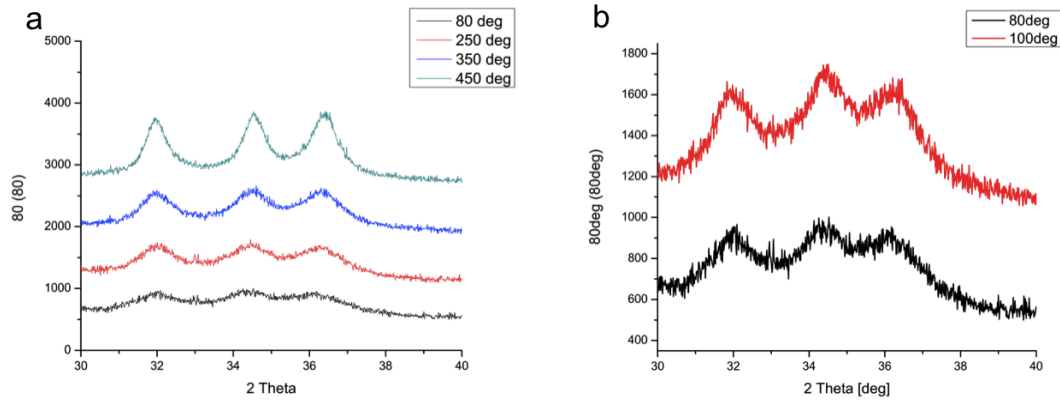


Figure 5.6: XRD characterization of mesoporous ZnO (a) based on annealing at various temperatures after ALD at 80 °C and (b) different deposition temperatures without further annealing

withstand temperatures up to 110 °C, above which deformation of morphology and collapse of the polymer structure was observed. The deposition temperature window for ALD of ZnO was reported to be 80 °C-150 °C.^[22] Outside this window, a perfect deposition cycle might be hindered due to the temperature not being high enough for the surface reaction to start, or being too high to cause precursor dissociation. The temperature stability of the cross linked PS template was found to be around 110 °C, in order to keep this method applicable for other different types of polymer templates, the default deposition temperature was kept at 80 °C, the lowest possible of the conformal deposition window. Deposition at 100 °C was later investigated to explore the deposition temperature dependence of crystallite size of deposited ZnO, but the crystallite size did not differ from that of 80 °C deposition (**Fig. 5.6 b**).

5.3.1.4 Mesoporous ZnO characterization

5.3.1.5 X-ray diffraction (XRD)

The replicated ZnO was characterized using XRD under various fabrication conditions. In order to examine the crystallization behaviour with respect to annealing

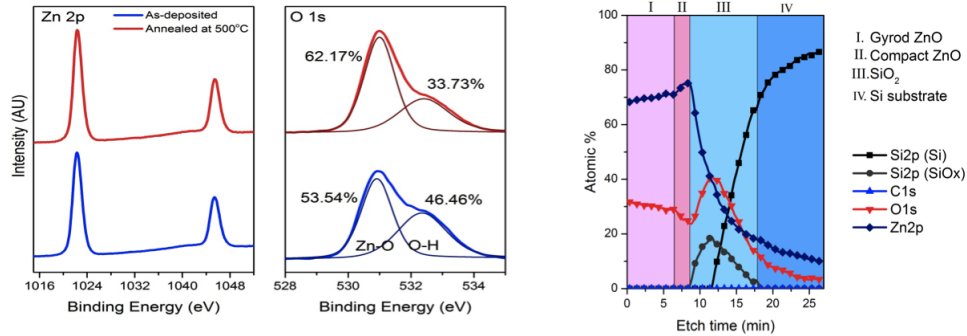


Figure 5.7: XPS spectra of (a) Zn2p and O1s on as-deposited and annealed films. (b) depth profiling of annealed film

temperature, the film was annealed at 250 °C, 350 °C and 450 °C. (**Fig. 5.6 a**) Before the heat treatment, the polymer was removed by O₂ plasma treatment. The peaks corresponding to [100], [001], [002] of wurtzite ZnO^[23] were observed. This smooth coating mechanism was once more supported by the XRD data. The as-deposited ZnO film, after the removal of polymer by O₂ plasma, appears to have very small crystallite sizes. The as-deposited ZnO, without further annealing, was nanocrystalline (or amorphous) as demonstrated by the broad peaks. Upon annealing, the peaks sharpen, indicating growth of crystallites. Using Scherrer equation, the crystallite sizes were calculated for each deposition temperature to be 13 nm for 250 °C and 350 °C, 25 nm for 450 °C and 550 °C. According to previous studies for solar cells crystallite sizes of 20 nm were reported to be optimal for solar cell performance.^[24] The deposition temperature was increased to 100 °C to check whether this would affect the crystallite size. As shown in **Fig. 5.6 b**, the higher deposition temperature did not alter the crystallinity of the as deposited film.

5.3.1.6 X-ray photoemission spectroscopy (XPS)

The chemical composition of the film was probed by means of x-ray photoemission spectroscopy. **Fig. 5.7a** shows the Zn2p and O1s spectra of as deposited and

400 °C annealed films. The Zn2p₃ peak appears at 1022.3 eV, in good agreement with previous reports for ZnO.^[25] The O1s peak is deconvolved into a low binding energy peak at 530.9 eV and a high binding energy peak at 532.4 eV. The low binding energy peak is assigned to fully coordinated Zn-O-Zn oxygen atoms, while the high binding energy peak is due to partly coordinated Zn-O-H atoms. The percentages represent the relative contribution to the O1s peak by each species. It is clear that annealing increases the percentage of fully coordinated O atoms in the film. The surface scan also revealed the existence of adventitious carbon (not shown here) which accounted for 10% of the atomic composition. To probe the mesoporous layer composition below the surface, an XPS depth profile was obtained. **Fig. 5.7b** shows the evolution of Zn2p, O1s, C1 and Si2p (Si and SiO₂) with etching time. The top surface scan **Fig. 5.7a** was not included in the depth profile due to the 10% contamination C layer on top of the surface. The depth profile demonstrates that the composition of the ZnO gyroid (I) is uniform up to the ZnO compact layer (II) on the SiO_x/Si substrate (III and IV). Additionally, it demonstrates that no carbon remains inside the gyroid structure consistent with full removal of the polymer template. Throughout the gyroid, the ZnO composition is not stoichiometric, but highly oxygen deficient, as expected from ZnO layer.

5.3.1.7 Potential application in hybrid photovoltaics

To demonstrate the potential of application of the mesoporous ZnO layer for hybrid photovoltaics, a polymer/mesoZnO solar cells was fabricated. For this purpose, a wormlike mesoporous layer was deposited on conductive pre-patterned ITO substrate and infiltrated with a poly(3-hexylthiophene) (P3HT) polymer. The wormlike ZnO structure was chosen due to the increased degree of control over the film thickness and uniformity it offers. **Fig. 5.8 a and b** present the external quantum efficiency of the photovoltaic device and its $J - V$ characteristics under solar simulator conditions, respectively. The device performance parameters are shown in the

inset of Fig. 5.8 b .

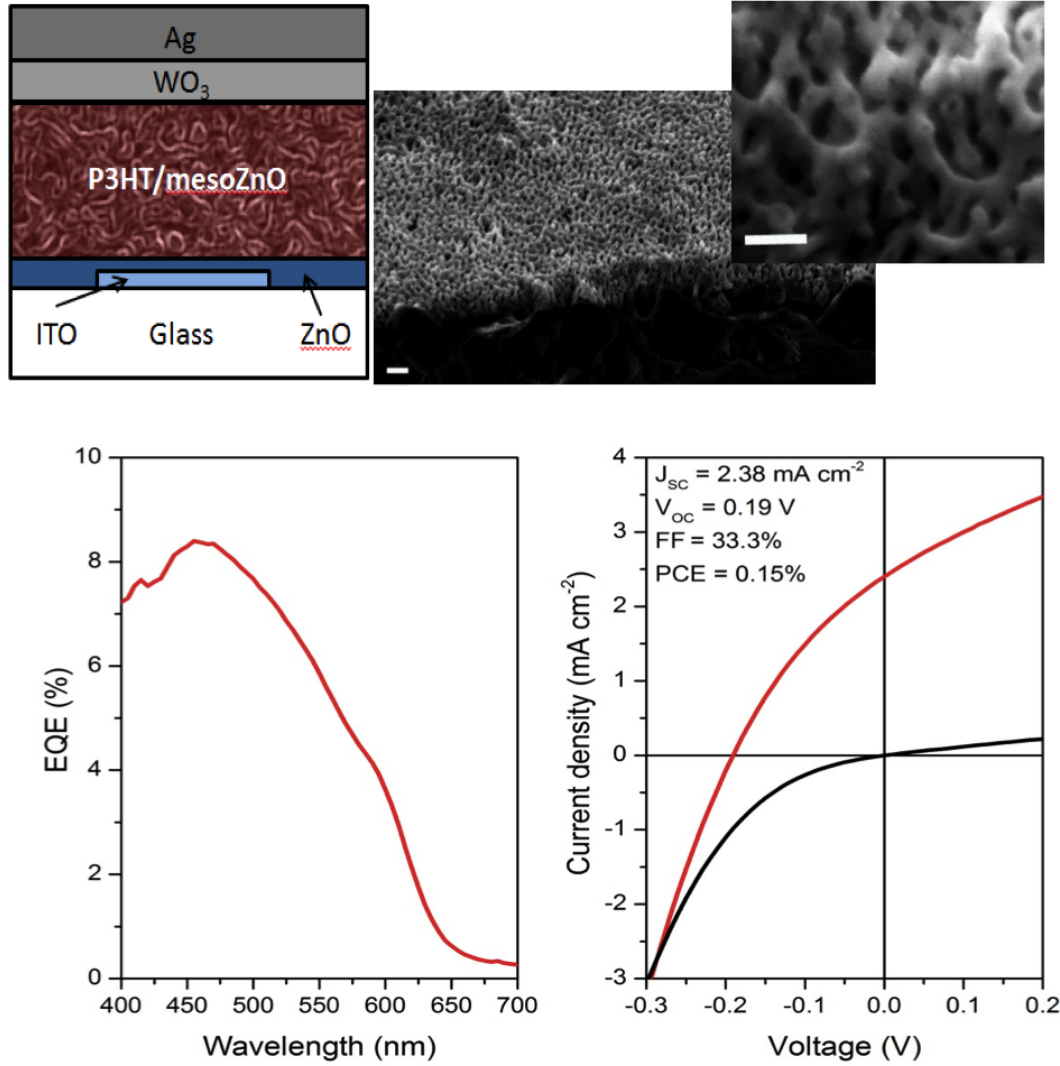


Figure 5.8: Summary of the architecture and performance of ZnO/P3HT device built using a wormlike ZnO film of 250nm thickness

The short circuit current of the device (2.38 mA/cm^2) is significantly improved over that of a bilayer ZnO/P3HT device (0.47 mA/cm^2) fabricated in the same device architecture^[25]. This is consistent with the much increased interfacial area of the P3HT/ZnO at which excitons can dissociate into charges and contribute

to photocurrent. The open circuit voltage (V_{oc}) of the device is measured to be ~ 0.2 V. The work function and the bandgap of the ZnO, which depend on the exact processing conditions, would affect the V_{oc} .^[26] This suggests that altering the mesoporous ZnO layer fabrication procedure is required to increase the V_{oc} to match that of P3HT/ZnO nanowire devices in which V_{oc} of up to 0.43 V was reported.^[23] Finally, the poor fill factor (FF) of the device suggests that charges were not extracted efficiently from the device. This is likely to result from the variations in film thickness and surface roughness which limit charge transport and extraction. We find that the limiting factor for optimisation remains controlling the surface roughness during the ICP etching of the compact layer and further studies to resolve this are ongoing. We note that the performance of the photovoltaic device is moderate, but promising as it is comparable to previous reports of P3HT/ZnO nanocrystal mesoporous layers.^[24]

5.4 Conclusions

We have presented two routes to fabricating a well-defined, 3 dimensional mesoporous nanostructures of ZnO on the 20-40nm length scale, by atomic layer deposition of ZnO onto a sacrificial porous template. One route leads to highly periodic double gyroid morphology, and the other results in a wormlike morphology, which still offers a well-defined structure with interconnected pores. While gyroid ZnO offers an extremely periodic morphology, it requires delicate processing conditions and long preparation times. On the other hand, the wormlike structure, was achieved by a more controllable and simpler route, which could be beneficial for large-scale production. The key to realising these structures was to bypass the rapid crystallisation behaviour of ZnO. Theoretically, ALD offers a surface limited reaction which leads to conformal coating of a 3D surface. However, in a system like ours where the

channel width is around 30 nm, ensuring that the surface of our polymer template was rich in OH group was important because -OH groups initially act as reaction sites for the first precursors, which would influence the size of ZnO crystallites.

The fabricated films were characterised using XPS, XRD and SEM, which confirmed deposition of wurzite ZnO throughout the film. It was also shown that the as-deposited ZnO (at 80°C) onto the polymer substrate was nanocrystalline, and the size of crystallites showed growth as the post annealing temperature increased. The structure also showed thermal stability at 550°C. The average pore dimension in these structures was approximately 30 nm, based on the SEM characterisation, demonstrating high potentials for hybrid photovoltaic application. Preliminary results were presented on using the wormlike structure to build a poly (3-hexylthiophene)/wormlike ZnO structure solar cell, demonstrating its application potential.

Bibliography

- [1] Djurišić, A.B., Chen, X., Leung, Y.H., and Ng, A.M.C. (2012) ZnO nanostructures: growth, properties and applications. *J. Mater. Chem.*, **22** (14), 6526, doi:10.1039/c2jm15548f. [80](#)
- [2] Gwinner, M.C., Vaynzof, Y., Banger, K.K., Ho, P.K.H., Friend, R.H., and Sirringhaus, H. (2010) Solution-processed zinc oxide as high-performance air-stable electron injector in organic ambipolar light-emitting field-effect transistors. *Adv. Funct. Mater.*, **20** (20), 3457–3465, doi:10.1002/adfm.201000785. [80](#)
- [3] Zhang, Q., Dandeneau, C.S., Zhou, X., and Cao, G. (2009) ZnO nanostructures for dye-sensitized solar cells. *Adv. Mater.*, **21** (41), 4087–4108, doi:10.1002/adma.200803827. [80](#)
- [4] Qiu, J., Guo, M., and Wang, X. (2011) Electrodeposition of hierarchical ZnO nanorod-nanosheet structures and their applications in dye-sensitized solar cells. *ACS Applied Materials & Interfaces*, **3** (7), 2358–2367.
- [5] Ko, S., Lee, D., Kang, H., Nam, K., Yeo, J., Hong, S., Grigoropoulos, C., and Sung, H. (2011) Nanoforest of hydrothermally grown hierarchical ZnO nanowires for a high efficiency dye-sensitized solar cell. *Nano Letters*, **11** (2), 666–671. [80](#)
- [6] Scharrer, M., Wu, X., Yamilov, A., and Cao, H. (2005) Fabrication of inverted opal ZnO photonic crystals by atomic layer deposition. *Applied Physics . . .* URL <http://link.aip.org/link/?APPLAB/86/151113/1>. [81](#), [88](#)
- [7] Wagner, T., Waitz, T., Roggenbuck, J., Fröba, M., Kohl, C.D., and Tiemann, M. (2007) Ordered mesoporous ZnO for gas sensing. *Thin Solid Films*, **515** (23), 8360–8363, doi:10.1016/j.tsf.2007.03.021. [81](#)
- [8] Lepoutre, S., Julián-López, B., Sanchez, C., Amenitsch, H., Linden, M., and Grosso, D. (2010) Nanocasted mesoporous nanocrystalline ZnO thin films. *J. Mater. Chem.*, **20** (3), 537, doi:10.1039/b912613a. [81](#)
- [9] Yang, P., Zhao, D., Margolese, D.I., Chmelka, B.F., and Stucky, G.D. (1999) Block copolymer templating syntheses of mesoporous metal oxides with large ordering lengths and semicrystalline framework. *Chem. Mater.*, **11**, 2813–2826. [81](#)

-
- [10] Crossland, E., Kamperman, M., Nedelcu, M., Ducati, C., Wiesner, U., Smilgies, D., Toombes, G., Hillmyer, M., Ludwigs, S., and Steiner, U. (2008) A bicontinuous double gyroid hybrid solar cell. *Nano letters*, **9** (8), 2807–2812. [81](#)
- [11] Hsueh, H. and Ho, R. (2012) Bicontinuous ceramics with high surface area from block copolymer templates. *Langmuir*, **28** (22), 8518–8529. [81](#)
- [12] Gordon, R., Hausmann, D., Kim, E., and Shepard, J. (2003) A kinetic model for step coverage by atomic layer deposition in narrow holes or trenches. *Chemical Vapor Deposition*, **9** (2), 73–78. [81](#), [89](#), [90](#)
- [13] Karuturi, S.K., Liu, L., Su, L.T., Chutinan, A., Kherani, N.P., Chan, T.K., Osipowicz, T., and Tok, A.I.Y. (2011) Gradient inverse opal photonic crystals via spatially controlled template replication of self-assembled opals. *Nanoscale*, **3** (12), 4951, doi:10.1039/c1nr11248a.
- [14] Elam, J., Routkevitch, D., Mardilovich, P., and George, S. (2003) Conformal coating on ultrahigh-aspect-ratio nanopores of anodic alumina by atomic layer deposition. *Chem. Mater.*, **15** (18), 3507–3517. [81](#), [89](#), [90](#)
- [15] Wang, Y., Qin, Y., Berger, A., Yau, E., He, C., Zhang, L., Gösele, U., Knez, M., and Steinhart, M. (2009) Nanoscopic morphologies in block copolymer nanorods as templates for atomic-layer deposition of semiconductors. *Adv. Mater.*, **21** (27), 2763–2766, doi:10.1002/adma.200900136. [81](#)
- [16] Ndoni, S., Li, L., Schulte, L., Szewczykowski, P.P., Hansen, T.W., Guo, F., Berg, R.H., and Vigild, M.E. (2009) Controlled photooxidation of nanoporous polymers. *Macromolecules*, **42** (12), 3877–3880, doi:10.1021/ma900485q. [84](#), [91](#)
- [17] Grigoras, K., Airaksinen, V., and Franssila, S. (2009) Coating of nanoporous membranes: atomic layer deposition versus sputtering. *Journal of nanoscience and nanotechnology*, **9** (6), 3763–3770. [88](#)
- [18] George, S. (2010) Atomic layer deposition: an overview. *Polymer*, **1550**, 125. [89](#)
- [19] Skoog, S., Bayati, M., Petrochenko, P., Stafslie, S., Daniels, J., Cilz, N., Comstock, D., Elam, J., and Narayan, R. (2012) Antibacterial activity of zinc oxide-coated nanoporous alumina. *Materials Science and Engineering: B*. [89](#)
- [20] Alessandri, I., Zucca, M., Ferroni, M., Bontempi, E., and Depero, L. (2009) Growing zno nanocrystals on polystyrene nanospheres by extra-low-temperature atomic layer deposition. *Crystal Growth and Design*, **9** (3), 1258–1259. [91](#)
- [21] Urbas, A., Maldovan, M., DeRege, P., and Thomas, E. (2002) Bicontinuous cubic block copolymer photonic crystals. *Adv. Mater.*, **14** (24), 1850–1853. [91](#)

- [22] Yamada, A., Sang, B., and Konagai, M. (1997) Atomic layer deposition of zno transparent conducting oxides. *Applied surface science*, **112**, 216–222. [93](#)
- [23] Olson, D., Shaheen, S., Collins, R., and Ginley, D. (2007) The effect of atmosphere and zno morphology on the performance of hybrid poly (3-hexylthiophene)/zno nanofiber photovoltaic devices. *The Journal of Physical Chemistry C*, **111** (44), 16 670–16 678. [94](#), [97](#)
- [24] Bouclé, J., Snaith, H., and Greenham, N. (2010) Simple approach to hybrid polymer/porous metal oxide solar cells from solution-processed zno nanocrystals. *The Journal of Physical Chemistry C*, **114** (8), 3664–3674. [94](#), [97](#)
- [25] Vaynzof, Y., Kabra, D., Zhao, L., Ho, P., Wee, A., and Friend, R. (2010) Improved photoinduced charge carriers separation in organic-inorganic hybrid photovoltaic devices. *Applied Physics Letters*, **97** (3), 033 309–033 309. [95](#), [96](#)
- [26] Lee, Y., Davis, R., Lloyd, M., Provencio, P., Prasankumar, R., and Hsu, J. (2010) Open-circuit voltage improvement in hybrid zno–polymer photovoltaic devices with oxide engineering. *Selected Topics in Quantum Electronics, IEEE Journal of*, **16** (6), 1587–1594. [97](#)

Chapter 6

Fabrication of 3D Amorphous I(G)ZO via Solution-Impregnation

Chapter Overview

In this chapter, we present a novel fabrication route to a mesoporous amorphous transparent conducting oxide (a-TCO) film of well-defined, 3D morphology obtained by self assembly and block copolymer (BCP) phase-separation at an off-equilibrium state. Indium Gallium Zinc Oxide (IGZO) precursor solution was impregnated into a mesoporous polystyrene template fabricated by phase separation of a BCP. While the gyroid structure provides a potential application for structural studies, a worm-like template can provide a simple and controlled route to fabricating a 3D porous material. Upon removal of the sacrificial template, amorphous IGZO of the replicated 3D structure was accomplished. The system is presented with various dimensions of control and variability, which implies potential for many future applications. The conductivity of the material can be tuned via chemical composition of the metal oxide, and the thickness of the material can be controlled by varying the thickness of the substrate.

6.1 Introduction

Amorphous oxides, compared to the conventional polycrystalline (or nanocrystalline) TCOs, are favourable in terms of uniformity of thin film characteristics, absence of grain boundaries, which could cause unwanted brittleness and scattering, as well as processing temperature. These characteristics not only improve the current electronic applications but also can serve as a platform for the development of new device technologies. Numerous studies have recently been reported on an effective thin film deposition method, compositional studies, and properties of amorphous ternary oxides such as InZnO (IZO), InGaZnO(IGZO), and ZnSnO(ZTO).^[1-5] These films were deposited mainly via physical vapour deposition methods such as magnetron sputtering or pulse laser deposition (PLD), as they are currently the methods conventionally used for thin film TCO deposition.

The solution processing method for amorphous TCO (a-TCO) thin films is more economical compared to the conventional physical vapour deposition methods. More importantly, unlike the isotropic nature of the PVDs, this method opens up the possibility of fabrication of 3D structured aTCO materials. Only recently, Banger *et al.* successfully fabricated thin films of I(G)ZO by solution processing methods using metal alkoxides as sol gel precursors which for the first time lead to stable, high-performing TFT devices.^[6]

As discussed in Chapter 3, the current trend in various areas of nanotechnology can benefit from engineering a new class of material which has extra properties in addition to transparency and conductivity. In this regard, fabricating a mesoporous, transparent conductive electrode can open up various new device architecture and application by providing a TCO with a high surface area as well small feature size (20-40nm) allowing a shorter electron percolation path. Currently, only a limited number of studies have reported techniques for fabrication of mesoporous structured TCOs using antimony doped tin oxide and indium doped tin oxide.^[7-9] The common

challenges of such studies include gaining control over the crystallisation kinetics while maintaining the conditions for blockcopolymer (BCP) self-assembly, which is often challenging. Moreover, due to the difficulty of fully understanding crystallisation behaviour and incorporating such a material into the 3D structure itself, reliable thin film processing of such mesoporous materials has yet to be reported. Therefore, mesoporous a-TCO can be a more reliable and consistent material for applications such as display, and organic solar cells, and flexible electronics.

In this study, we introduce a new method of creating a 3D mesoporous amorphous TCO by solution impregnation of InGaZnO (IGZO) into a sacrificial porous template. Using the metal alkoxide precursors of GIZO/IZO used in Banger et al^[6], we were able to successfully replicated 3D mesoporous BCP templates, resulting in a 3D mesoporous thin film of I(G)ZO.

Replication of porous polymer templates using transition metal oxides via solution impregnation has been reported using sol-gel of TiO₂ and ZnO, and nanocrystals of SnO₂.^[10-12] nanocrystal-based or sol-gel methods were challenged by either rapid hydrolysis and gelation kinetics of the sol solution^[13], or aggregation of nanocrystals^[14] which causes pore blockage preventing uniform infiltration of nanocrystals into the porous template. In addition, drop casting^[13] and dip coating^[11] were used in the previous studies, but limited efforts have been made to process these materials in a controllable manner in thin film form. In a general sol-gel route, a hydrolysis process dominates the metal oxide formation, as condensation would only occur after enough of RO-M species have formed. The hydrolysis kinetics of sol-gel precursors of transition metal oxide are often difficult to control, as they occur too rapidly and cause gelation. Therefore, controlling the hydrolysis kinetics has been the main challenge of sol-gel synthesis of mesoporous metal oxides.

In this regard, the I(G)ZO sol-gel chemistry used in this study is ideal for impregnation into porous templates of such a small feature size (≤ 40 nm). First of all,

metal alkoxides present themselves as ideal candidates for sol-gel precursors due to the ease of M-O-M bond formation by a condensation mechanism. Additionally, the organic ligands used in the precursor solutions can undergo a beta hydride elimination mechanism, allowing the parent alkoxides to form metal oxide upon pyrolysis. Therefore, using this chemical route, formation of metal oxide is possible via condensation mechanisms including ololation and oxolation. In other words, in absence of H₂O and O₂, a hydrolysis process is avoided, and thus the precursors can undergo a controlled I(G)ZO formation, after they were infiltrated into the polymer structure, via condensation route which can be activated by simply heating at ~250°C.

Herein, we present a simple route to fabricating 3D structured I(G)ZO with mesopores on the 20 nm lengthscale. The schematics summarizing the fabrication method is presented in **Fig. 6.1 a and b** and representative images of the templates used (further details in Chapter 4) are in **Fig. 6.1 c and d**. The films are further characterised electrically and optically to demonstrate their potential use as an electrode.

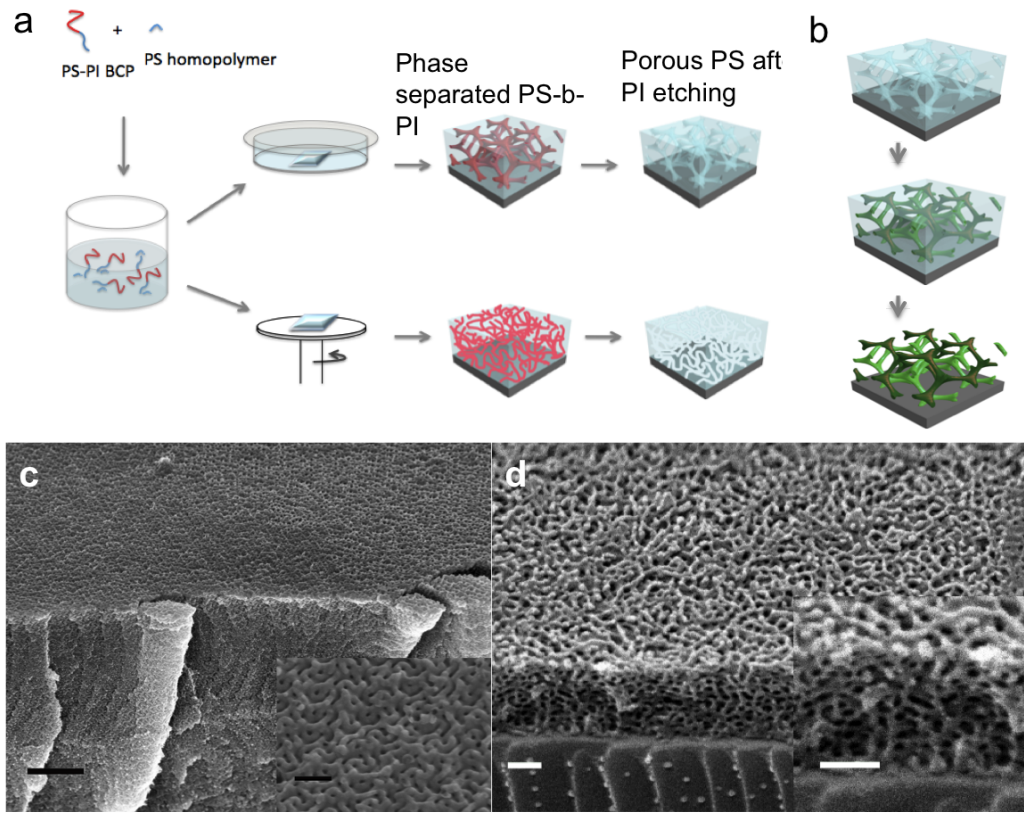


Figure 6.1: Schematics of template fabrication (a) and fabrication of mesoporous IGZO (b) using porous polystyrene (PS) substrates of gyroid (c) and wormlike (d) morphologies

6.2 Experimental

Molecular precursors for formation of I(G)ZO

The indium and gallium molecular precursors were made by the route published by Bradley *et al.*^[15] and then more recently by Leedham *et al.*^[16] whereas the zinc alkoxides were made by the method published by Kageyama *et al.*^[17] In brief, the molecular alkoxides were made via a metathesis reaction between the alkaline/alkaline earth alkoxide and indium/gallium and zinc halide derivatives. The isolated target compound was then dissolved in the parent alcohol solution to achieve the desired molarity. Alternatively the compounds can be purchased commercially. The molec-

ular structures of the precursors are illustrated in **Fig. 6.2**.



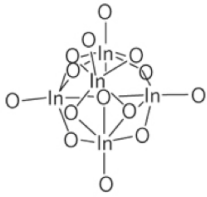
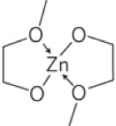
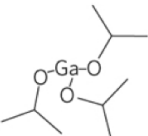
Material	Structure/type	Extrapolated temperature for decomposition (°C/% residue)	Activation energy for onset of decomposition (kJ mol ⁻¹)	Expected oxide and % residue
Indium oxo cluster In ₅ O(OPr) ₄ (OPr) ₄ (OPr) ₅ (Isopropyl groups omitted for clarity)		204 (51%)	119.6	In ₂ O ₃ (51%)
Zinc-bis-methoxyethoxide Zn(OC ₂ H ₄ OCH ₃) ₂		341 (38%)	54.4	ZnO (38%)
Gallium-tris-isopropoxide [Ga(OPr) ₃]		203 (58%) 528 (47%) 775 (41%)	172.4	Ga ₂ O ₃ (38%)

Figure 6.2: Chemical details of the sol gel precursors for IGZO^[6]

Solution processing method for infiltration into mesoporous template

The polymer templates were fabricated in exactly the same manner as that summarised in Chapter 5. Further fabrication details were discussed in Chapter 4. In order to control the condensation process of the sol-gel precursor, which is crucial for uniform pore-filling without blockage, all of the solution processing was carried out in the glovebox without presence of H₂O and O₂. Spin coating and blade coating were utilised for preparing mesoporous IGZO films

Removal of polymer template via thermal calcination

An annealing temperature of 400°C in air was used in order to ensure that the PS template was completely removed. In addition, XPS findings from Banger *et al.* showed that M-O-M bonds significantly increased between 350°C and 450°C, which

resulted in better TFT device performance.

Optical Characterisation

Ellipsometry was used to measure the refractive index of the films, and reflectance and transmittance spectra were measured using an optical microscope.(Olympus BX-51, 20× objective lens)

Electrical Characterisation

Two planar contacts were thermally evaporated through a shadow mask on top of the mesoporous or dense oxide layer fabricated on glass, which defines the contact width (W) and contact separation (l). The area (A), is then defined by using the thickness of the oxide layer (t) and width of the contact (W). Current voltage measurements are then undertaken to determine (R), using an Agilent semiconducting parameter analyser (SPA). The resistivity is then calculated by

$$\rho = R \frac{A}{l}. \quad (6.1)$$

In addition, in order to verify the calculated values from **Eq. 6.1**, the resistivity was also determined by the approximation according to Schroeder,^[18],

$$\rho = \frac{\pi}{\ln 2} \left(\frac{V}{l} \right). \quad (6.2)$$

Metal contacts were thermally evaporated using an Edwards 4-turrent evaporator at 10^{-6} torr. Electrical testing was undertaken using an Agilent SPA 4155 analyser, all current voltage measurements were performed in a Bell glovebox in a N_2 atmosphere. Samples were made and annealed at the same time on a hotplate to allow for comparative analysis before electrical testing.

6.3 Results and Discussion

6.3.1 Chemical compatibility

The sol-gel system was originally developed for TFT applications where the precursor solution concentration was $< 0.1\text{M}$. For this study, concentration of the precursor solution can be an important parameter for successful infiltration. It was determined that 0.1M of precursor solution corresponds to approximately $2\text{wt}\%$ in terms of the resulting metal oxide. In the studies available, precursor solutions from $5\text{ wt}\%$ to $30\text{-}40\text{ wt}\%$ were used.^[13] Precursor solutions of concentrations higher than 0.6M exhibited unwanted precipitation indicating saturation. Therefore, precursor solutions between 0.05M and 0.6M were the variable range for use in this study.

6.3.2 Replication of I(G)ZO by solution impregnation

Essentially, the pore filling mechanism resembles that described in^[19]. Upon initial wetting of the template by the solution, the solution is completely infiltrated, filling the pores of the templates. At this stage, the volume that the metal precursors take up in the pores corresponds to the concentration of the solution multiplied by the volume of the pore. As the solvent evaporates from the top layer, the concentration gradient between the more concentrated region (towards the substrate surface) to that of less causes more precursors to fill up the pore until the top layer dries, stopping the fluid movement into the pores. The main factors governing the degree of pore filling can be listed as follows:

- Concentration and viscosity of precursor solution: The concentration of the precursor solution used in this experiment ranged from 0.05M to 0.6M , where 0.05M corresponded to $1\text{ wt}\%$. The viscosity increased as the concentration increased, and the solutions over 0.3M were visibly more viscous and exhibited faster evaporation kinetics.

- Evaporation kinetics of the solvent: The sol-gel chemistry of IGZO is a delicate system. Although slow drying is more favorable for pore filling process, exchange of solvents to those with slower evaporation kinetics (i.e. higher boiling point) such as toluene or chlorobenzene resulted in precipitation and gelation of the precursor solution. Therefore, the solution was used as is, using isopropanol as a solvent.
- Thickness and porosity of the template (discussed in detail later in this chapter)
- Chemistry of the template surface: The PS template surface is rich in OH groups, as discussed in Chapter 4, after UV treatment and short O₂ plasma etching to completely open up the pores. Based on the SEM images, complete wetting of the template surface was observed as quickly as 1 minute after sample immersion. However, the degree of hydrophilic nature depends on how long after preparation the substrate is used, and initial wetting behaviour differed, observing the spreading of droplet of the solution. Therefore, the templates were immersed in the precursor solution overnight (12+ hours) to ensure complete wetting of the pore surface.
- The amount of precursor solution remaining on the porous template before drying

Although the underlying pore-filling mechanism resembles the one presented by *et al.*^[19], there are several key differences between the two systems which can be summarised as:

- Difference in boiling points of the solvents: The boiling point of isopropanol used in this study (83°C) is significantly lower than chlorobenzene (130°C) used by *et al.*^[19]. This can significantly alter the evaporation kinetics of the solution

- Different chemical nature of the solution and the template This study entails filling of metal oxide precursors into a polymer template whereas the referred study uses organic precursor into a paste of metal oxide particles.

The aim of this study is to fabricate a self standing porous thin film of IGZO, which means that almost complete filling of the pores was required before removal of the polymer template. Based on this comparison, several post infiltration processing methods were investigated both in bulk and thin film forms. Since the gyroid can best be prepared in bulk form, gyroid templates were replicated in bulk by simple impregnation and drying methods. However, in order for this material to be useful in applications, developing a reliable thin film deposition method is crucial. Two forms of film processing methods were investigated: spin coating and blade coating. The templates with wormlike morphologies were used to prepare sub-micron films.

6.3.2.1 Infiltration in bulk (gyroid samples)

Fabrication of gyroid I(G)ZO was carried out by fully immersing the gyroid template, in bulk form, in a 0.6M precursor solution. After overnight (12+ hours) of immersion, complete infiltration was consistently observed for samples of thicknesses > 3 m. Upon taking the sample out of the precursor solution, the samples were immediately dried using a nitrogen gun within 10-20 seconds. This indicates that for bulk samples which have a large exposed area for drying, pore-filling induced by the concentration gradient is relatively quick and therefore using a concentrated yet fast evaporating solution (0.6M) was preferable. The dense top layer (**Fig. 6.3 a**) results from the excess precursor solution dried on top of the porous layer. Formation thick top layer was avoided by removing the liquid on the template surface with non-absorbing object before drying the substrate using a nitrogen gun.

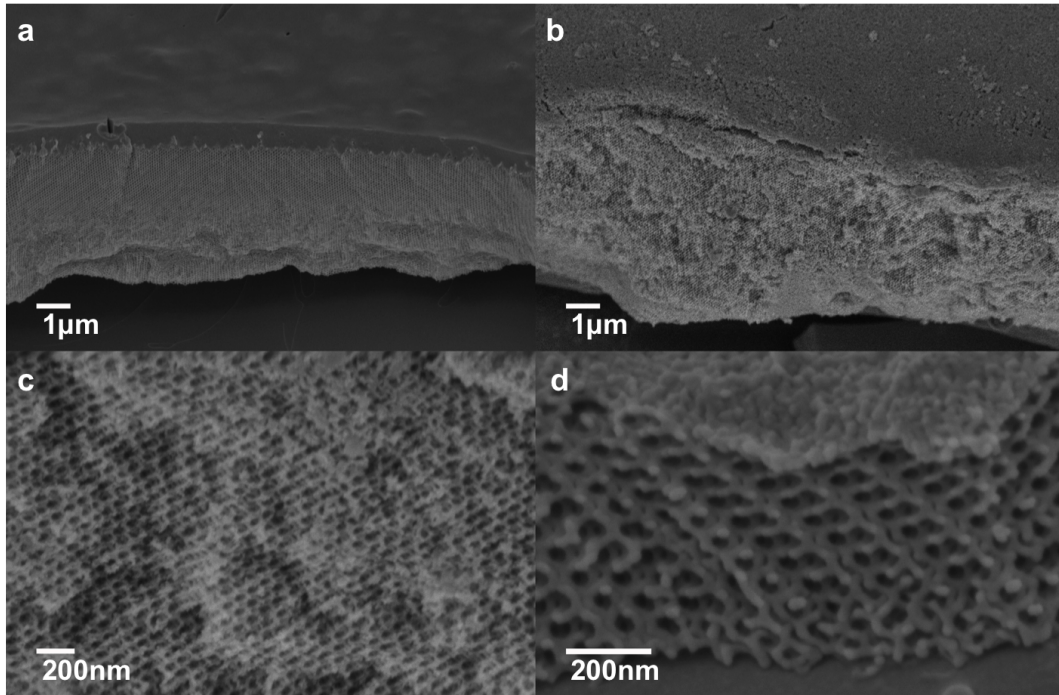


Figure 6.3: SEM images of gyroid IGZO upon removing the PS templates.

6.3.2.2 Preparation of thin films

Differently from the bulk system, the only area through which filling of precursors can occur is the substrate surface, which would significantly decrease the rate of pore filling. This implies that solvent evaporation was required to be as slow as possible.

Spin coating

Spin coating was employed as the method of choice, as it results in the best film quality out of many solution based thin film processing methods. Based on experimental observations, spin speeds between 500-750rpm rpm for longer than 2 minutes and the concentration between 0.05M (equivalent to 1wt%) to 0.1M were required in order to prevent top compact layer forming before infiltration occurs.

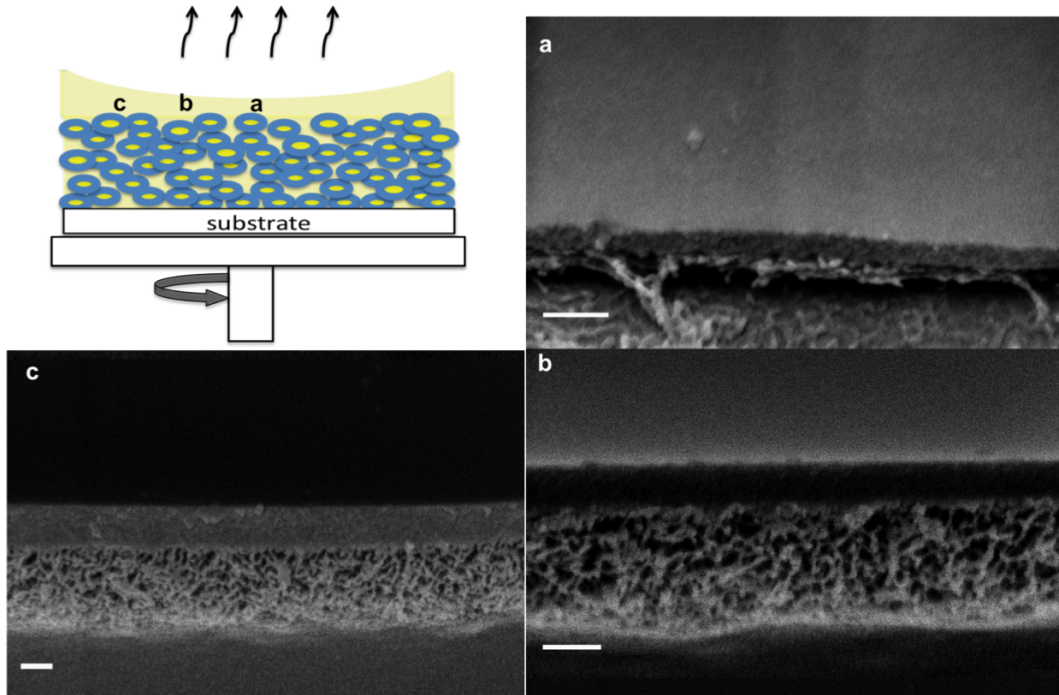


Figure 6.4: A schematic illustration and SEM images of IGZO precursor solution (0.1M) spin coated onto the PS template.

However, as demonstrated in **Fig. 6.4**, at a low slow spin speed, even though solvent evaporation rate is lowered, forming a homogeneous film is difficult. The areas a, b, c shown in **Fig. 6.4** illustrate this challenge. The further from the centre of the film, more complete infiltration was observed and at the same time, the thickness of the compact top layer increased. This is because formation of top layer depends on the amount of dilute precursors remaining on the template as well as the drying kinetics of the solvent. In the center of the film (**Fig. 6.4 a**), precursor solution dried out quicker before sufficient infiltration, which explains the collapsed bits of structure underneath the film. Near the outer edge of the film (**Fig. 6.4 c**), sufficient time was allowed for complete infiltration of the substrate due to larger amount of precursor solution available, but this also lead to a thicker top layer. The formation of a top layer is difficult to avoid, because it mainly depends on

the amount of precursors deposited immediately after the excess solution has been thrown off by initial spinning. Controlling this amount is nearly impossible and the amount required to avoid the top layer formation is too small that it would evaporate quicker than the time required for sufficient infiltration.

Blade Coating

The limitations of using spin coating for our system were overcome by blade coating. Using blade coating, the thickness of the initially deposited precursor film was more accurately controlled. The amount of pore filling can be predicted by an approach proposed by DoCampo *et al.*^[19]

$$PF = c + \frac{D * c}{D * p} \quad (6.3)$$

where D is the thickness of the dilute solution on top of the porous template after blade coating (illustrated in **Fig. 6.5**), c is the concentration of the precursor solution, and p is the pore volume of the template. According to the equation, the volume of the pores of the wormlike structure should equal to that of the minority block, which is 35%. In order to completely fill 35% of a 600 nm-thick template, 20m of 0.05M solution is required to be deposited for complete infiltration without the top layer. Subsequently, the solvent is required to slowly evaporate in order for the precursors to sufficiently evaporate. Therefore, a PTFE film was placed on top of the undried film immediately after blade coating. In order to prevent unwanted solvent evaporation, the blade coating speed was kept rapid (0.5cm/s). Experimental results (**Fig. 6.6**) showed that more precursor than the predicted amount was required to fill the pores. For example, a porous 450 nm-thick film shown in **Fig. 6.4 c** and **d** was obtained by blade coating 60 m of 0.05 M solution or 30 m of 0.1 M solution. This could be explained by the loss of some precursor solutions leaking out of the PTFE film upon placing it onto the samples due to capillary forces, as the coating process involves such a small amount of liquid. Regardless, this demonstrates that

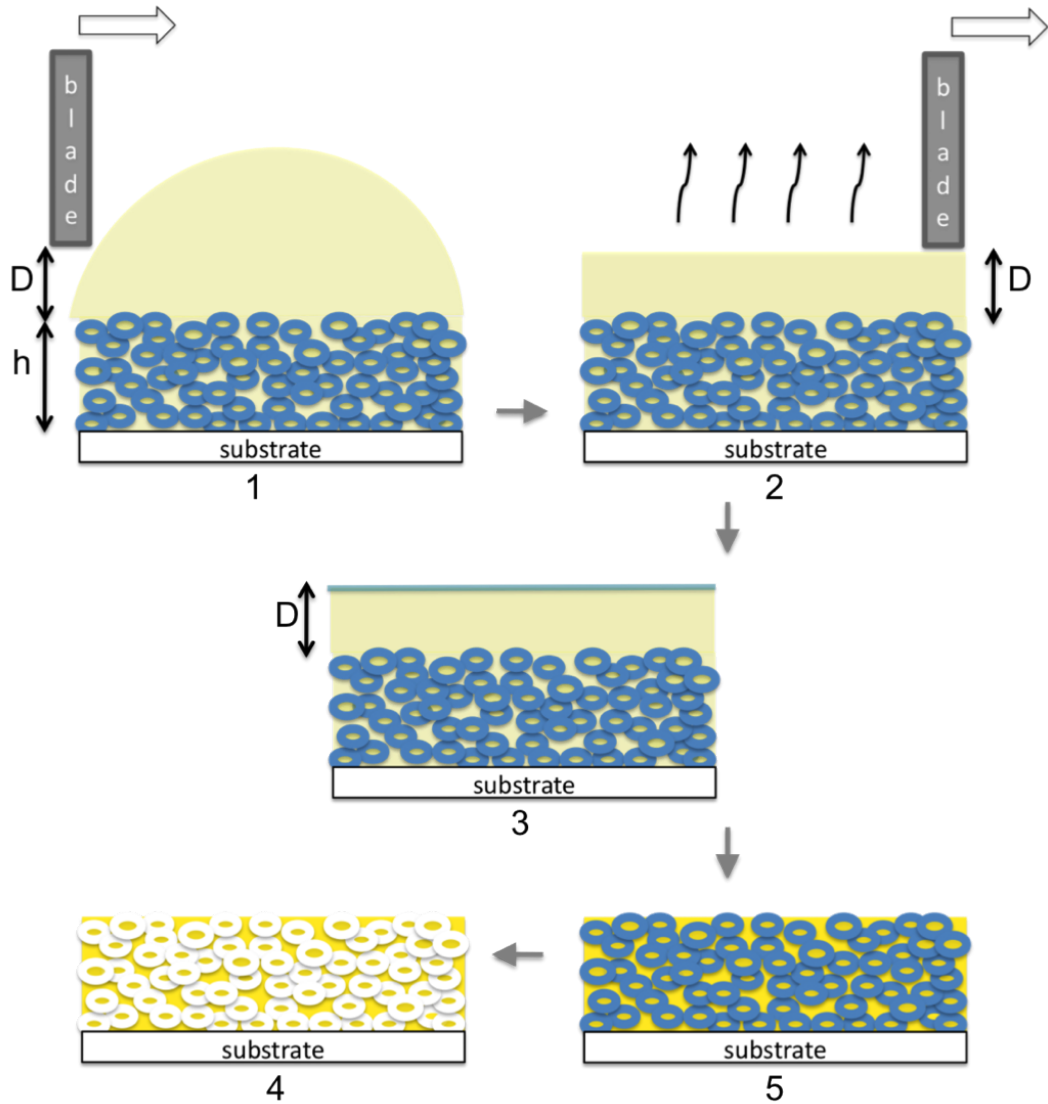


Figure 6.5: Schematic illustration of mesoporous I(G)ZO formation by blade coating of I(G)ZO solution onto the porous PS template (1, 2), placing a PTFE film on the film surface to allow a slow drying of the solvent (3), and when the solution is dried (4), the PS template is removed (5) by thermal calcination or oxygen plasma treatment

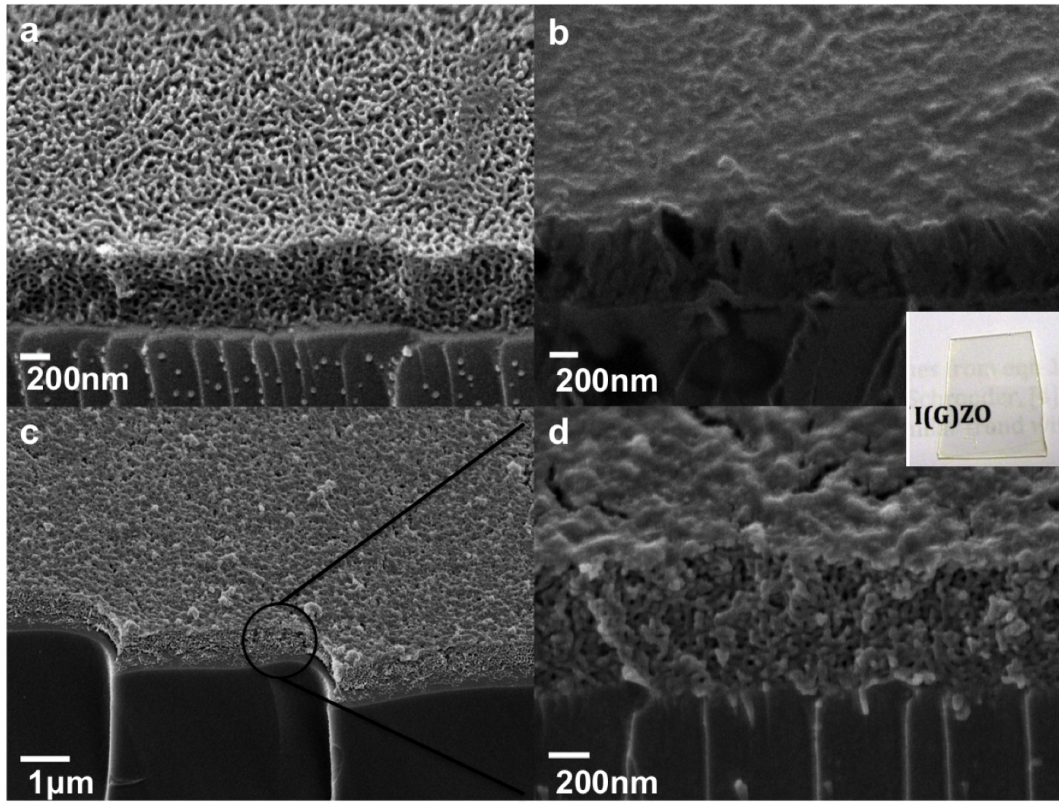


Figure 6.6: Complete replication process demonstrated using SEM images (a) PS template (b) IGZO precursor infiltrated into PS template, as deposited before heat treatment (c) upon removal of PS template via calcination at 400 °C (d) higher magnification image of (c) The optical image reveals the transparency of this film

blade coating followed by slow evaporation of solvent results in successful fabrication of porous IGZO thin films. Although experimental optimisation would be required, this approach can be applied to porous templates of various thicknesses. It is also likely that some structural collapse might have occurred in the bottom part of the film, as the resulting film is 150 nm thinner than the starting template of 600 nm thickness.

6.3.2.3 Further Characterisation

X-ray diffraction

The X-ray diffraction (XRD) spectra of the fabricated porous IGZO film is presented in **Fig. 6.7**. Distinct peaks corresponding to neither of In_3O_2 , Ga_3O_2 , or ZnO are absent, indicating that the material remains to be amorphous.

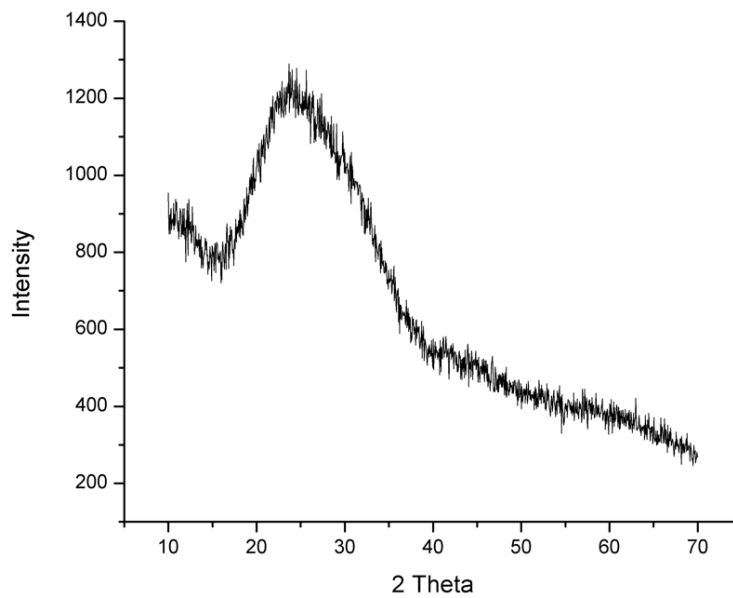


Figure 6.7: The XRD spectra of mesoporous IGZO film prepared on a glass substrate confirms that the films stays amorphous after solution processing and thermal calcination. IZO films of various composition used in conductivity study also exhibited amorphous broad maxima, almost identical to this figure.

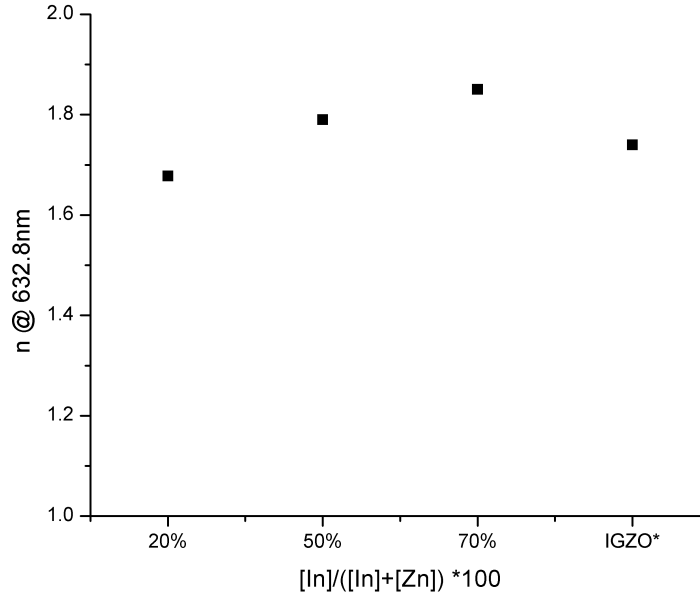


Figure 6.8: Refractive index of I(G)ZO of various compositions

Optical Characterisation

The refractive index of compact I(G)ZO film of various compositions prepared on Si substrates were first measured using ellipsometry (**Fig. 6.8**). Compared to the refractive index of 1.98 reported for IGZO fabricated by pulse laser deposition (PLD)^[1], the refractive index value is somewhat lower. This could be attributed to the nature of sol-gel chemistry used. Based on the refractive index measured for the compact films and the film thickness measured by SEM analysis, the refractive of the porous film (70% In) was approximated from curve fitting of transmittance and reflectance spectra (**Fig. 6.9**) using the transfer matrix method.^[20] The best fit gave a refractive index value of 1.5, corresponding to a porosity of $\sim 41\%$. This is lower than the calculated value of 65%, assuming that the entire volume of polystyrene template was conserved as a voided space. Based on the transmission and reflectance spectra, both mesoporous and compact thin films are indeed transparent. (**Fig.6.9**)

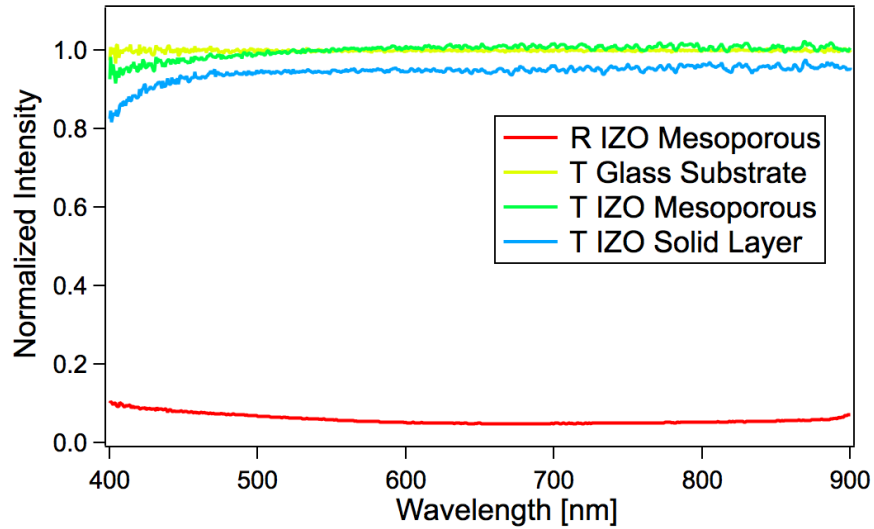


Figure 6.9: Transmission and reflectance spectra of mesoporous IZO (70% In) film, non-porous IZO film measured using optical spectroscopy. The transmittance of a blank glass substrate, which was used for calibration, is also displayed.

It is worth noting that, under the same measurement conditions, mesoporous film is more transmissive compared to the non-porous one, which agrees with the decreased refractive index of the porous film (~ 1.6), almost matching the refractive index of the glass (~ 1.5). The transmittance of the mesoporous film was measured from UV-VIS absorption spectra, as shown in **Fig.6.10**. The slightly decreased transmittance compared to that shown in **Fig.6.9** could be due to instrumental error and larger measurement area. Nevertheless, this confirms that the mesoporous film transmits across the entire visible spectrum from approximately 0.4-1.1 μm , which is required for a TCO material for display applications.^[21]

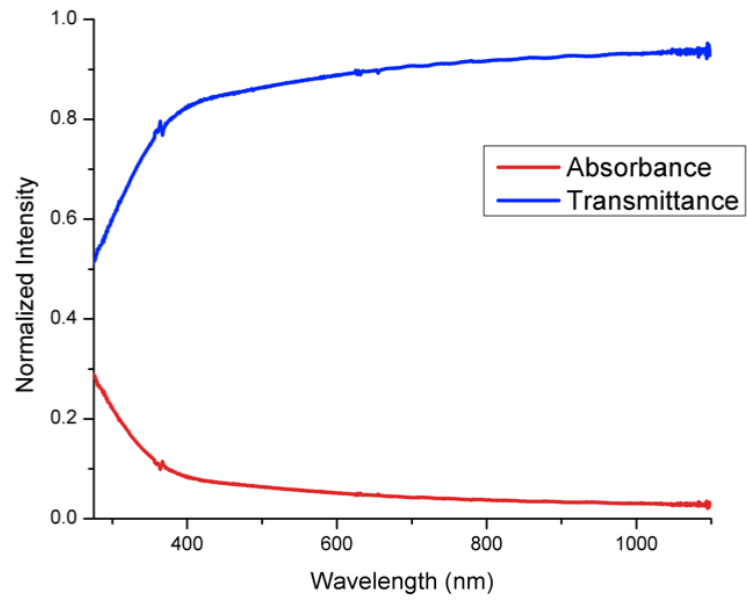


Figure 6.10: Absorption and transmission spectra of IZO (70% In) measured using UV-vis spectroscopy

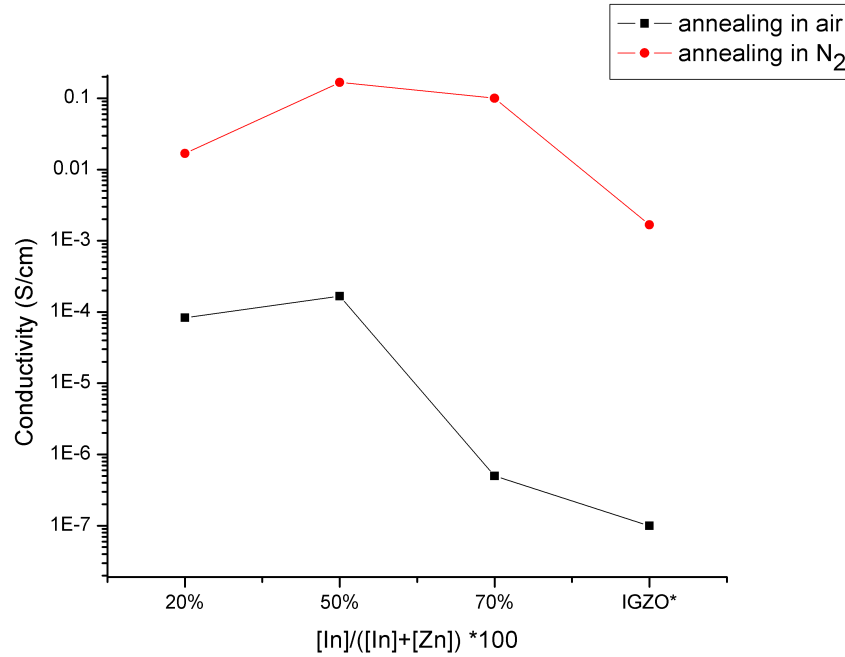


Figure 6.11: Conductivity of mesoporous films (400nm thickness) prepared using precursor solutions of IZO of different In:Zn ratios and IGZO. IGZO was prepared by introducing 5% of Ga precursors to In:Zn=7:3 solution. The ordinate values were calculated using Eq. 6.2.

Electrical Characterisation

As made, the conductivity for the mesoporous layers was relatively low in comparison to that reported for the analogous dense amorphous oxide thin film. (Fig. 6.11) As previously reported by Gwinner *et al.*^[22], annealing the completed devices (referred as post contact annealing) in the absence of oxygen is known to enhance the conductivity in oxides by inducing more intrinsic vacancies and reducing contact resistance, (not calculated here) to provide for better charge injection and extraction. The films were subsequently annealed at 260°C for one hour in a nitrogen atmosphere after which current voltage measurements were made on the same day. The conductivity shows the expected increase, in this case by approx. 4 orders of magnitude, which then results in comparable values to those of mesoporous ATO

and ITO^[7,9]. Importantly, it can be seen as previously observed for dense thin films, the conductivity of the mesoporous layer can also be tailored by stoichiometric adjustment of the metal oxide ratios, and further still by additional doping with the gallium which suppresses the formation of oxygen vacancies due to its higher Gibbs free energy of oxidation.

6.4 Conclusions and Future Work

In this chapter, a novel fabrication method of mesoporous a TCO was developed by taking advantage of two unique systems of micro-phase-separation of BCP and sol-gel chemistry of amorphous IGZO. The problem of fast hydrolysis kinetics, which is common in solution processing of transition metal oxides was avoided by using metal alkoxide sol-gel chemistry in a H₂O and O₂ free environment, allowing the condensation process to occur via ololation and oxylation once the precursor solution has fully infiltrated into the complex 3D structured template.

A reliable route to thin film fabrication of porous IGZO via impregnation was established by elucidating the pore filling mechanism by various processing conditions of immediate drying, spin coating and blade coating. In order to achieve complete replication and avoid the top compact layer, often observed in solution impregnation of templates, control of two key factors were required: deposition of the correct amount of the precursors and slow solvent evaporation.

The optical characterisation demonstrates that the refractive index can be lowered by creating pores in the structure and that the porous film is exceptionally transparent with very little scattering. By creating porous templates which can result in different porosities, the refractive index can be tuned while maintaining transparency of the material. Through electrical characterisation, it was demonstrated that conductivity of the mesoporous film could be varied by altering the stoichiometry of the precursors. Future effort should be placed on work to improve the conductivity of the films by further optimising the chemistry of the precursor solution and investigating alternative post annealing options such as exposure to UV and O₂ plasma.

Since the material is relatively new, additional characterisations remain to be made. For example, it would be useful to determine the work function, which can be characterised using X-ray photoemission spectroscopy (XPS) and ultraviolet

6.4 Conclusions and Future Work

photoemission spectroscopy (UPS). This would allow more detailed examination of the application potential in optoelectronic and organic solar cell applications.

Bibliography

- [1] Galca, A., Socol, G., and Craciun, V. (2012) Optical properties of amorphous-like indium zinc oxide and indium gallium zinc oxide thin films. *Thin Solid Films*, **520** (14), 4722–4725, doi:10.1016/j.tsf.2011.10.194. [103](#), [118](#)
- [2] Thakur, A., Kang, S., Baik, J., Yoo, H., Lee, I., Lee, H., Jung, S., Park, J., and Shin, H. (2012) Effects of working pressure on morphology, structural, electrical and optical properties of a-ingazno thin films. *Materials Research Bulletin*.
- [3] Kumar, B., Gong, H., and Akkipeddi, R. (2005) High mobility undoped amorphous indium zinc oxide transparent thin films. *Journal of applied physics*, **98** (7), 073 703–073 703.
- [4] Jung, K.T., Jin, Y.J., Ho, G.T., Nilesh, B., Young, K.J., Young, H.S., Dong, K.Y., Min, H.S., Hyuk, C.J., and Jinho, J. (2011) Effect of the ga ratio on the dielectric function of solution-processed ingazno films. *J. Korean Phys. Soc.*, **59** (6), 3396, doi: 10.3938/jkps.59.3396.
- [5] Ide, K., Nomura, K., Hiramatsu, H., Kamiya, T., and Hosono, H. (2012) Structural relaxation in amorphous oxide semiconductor, a-in-ga-zn-o. *Journal of Applied Physics*, **111** (7), 073 513–073 513. [103](#)
- [6] Banger, K.K., Yamashita, Y., Mori, K., Peterson, R.L., Leedham, T., Rickard, J., and Sirringhaus, H. (2010) Low-temperature, high-performance solution-processed metal oxide thin-film transistors formed by a ‘sol-gel on chip’ process. *Nat Mater*, **10** (1), 45–50, doi:10.1038/nmat2914. URL <http://dx.doi.org/10.1038/nmat2914>. [103](#), [104](#), [107](#)
- [7] Müller, V., Rasp, M., Rathouský, J., Schütz, B., Niederberger, M., and Fattakhova-Rohlfing, D. (2010) Transparent conducting films of antimony-doped tin oxide with uniform mesostructure assembled from preformed nanocrystals. *Small*, **6** (5), 633–637, doi:10.1002/sml.200901887. [103](#), [122](#)
- [8] von Graberg, T., Hartmann, P., Rein, A., Gross, S., Seelandt, B., Röger, C., Zieba, R., Traut, A., Wark, M., and Janek, J. (2011) Mesoporous tin-doped indium oxide thin films: effect of mesostructure on electrical conductivity. *Science and Technology of Advanced Materials*, **12** (2), 025 005.

- [9] Liu, Y., Štefanić, G., Rathouský, J., Hayden, O., Bein, T., and Fattakhova-Rohlfing, D. (2012) Assembly of mesoporous indium tin oxide electrodes from nano-hydroxide building blocks. *Chem. Sci.*, **3** (7), 2367, doi:10.1039/c2sc20042b. [103](#), [122](#)
- [10] Jiang, S. (2006) A review of wet impregnation—an alternative method for the fabrication of high performance and nano-structured electrodes of solid oxide fuel cells. *Materials Science and Engineering: A*, **418** (1), 199–210. [104](#)
- [11] Lepoutre, S., Julián-López, B., Sanchez, C., Amenitsch, H., Linden, M., and Grosso, D. (2010) Nanocasted mesoporous nanocrystalline zno thin films. *J. Mater. Chem.*, **20** (3), 537. [104](#)
- [12] Haffer, S., Waitz, T., and Tiemann, M. (2010) Mesoporous in₂o₃ with regular morphology by nanocasting: A simple relation between defined particle shape and growth mechanism. *The Journal of Physical Chemistry C*, **114** (5), 2075–2081. [104](#)
- [13] Hsueh, H. and Ho, R. (2012) Bicontinuous ceramics with high surface area from block copolymer templates. *Langmuir*, **28** (22), 8518–8529. [104](#), [109](#)
- [14] Lepoutre, S., Smått, J.H., Laberty, C., Amenitsch, H., Grosso, D., and Lindén, M. (2009) Detailed study of the pore-filling processes during nanocasting of mesoporous films using sno₂/sio₂ as a model system. *Microporous and Mesoporous Materials*, **123** (1-3), 185–192, doi:10.1016/j.micromeso.2009.03.047. [104](#)
- [15] Bradley, D., Chudzynska, H., Frigo, D., Hursthouse, M., and Mazid, M. (1988) A penta-indium oxo alkoxide cluster with a central 5-co-ordinate oxygen. preparation and x-ray crystal structure of (inopri)₅ (μ₂-opri)₄ (μ₃-opri)₄ (μ₅-o). *J. Chem. Soc., Chem. Commun.*, (18), 1258–1259. [106](#)
- [16] Leedham, T. (2008) Improvements in or relating to the synthesis of gallium and indium alkoxides. *GB Patent Application No. 2454019*. [106](#)
- [17] Kageyama, H., Miki, K., Tanaka, N., Kasai, N., Ishimori, M., Heki, T., and Tsuruta, T. (1982) Molecular structure of [zn (och₂ch₂ome)₂·(etznoch₂ch₂ome)₆]. an enantiomorphic catalyst for the stereoselective polymerization of methyloxirane. *Die Makromolekulare Chemie, Rapid Communications*, **3** (12), 947–951. [106](#)
- [18] Schroder, D.K. (2005) *Semiconductor Material and Device Characterization*, John Wiley Sons, Inc., Hoboken, NJ, USA. [108](#)
- [19] Docampo, P., Hey, A., Guldin, S., Gunning, R., Steiner, U., and Snaith, H.J. (2012) Pore filling of spiro-ometad in solid-state dye-sensitized solar cells determined via optical reflectometry. *Adv. Funct. Mater.*, pp. n/a–n/a, doi:10.1002/adfm.201201223. [109](#), [110](#), [114](#)
- [20] Born, M. Wolf, E. (1964) *Principles of optics: electromagnetic theory of propagation, interference and diffraction of light.*, Oxford, Pergamon Press. [118](#)

- [21] Paine, D., Yaglioglu, B., and Berry, J. (2010) Characterization of tco materials. *Handbook of Transparent Conductors*, pp. 111–148. [119](#)
- [22] Gwinner, M.C., Vaynzof, Y., Banger, K.K., Ho, P.K.H., Friend, R.H., and Sirringhaus, H. (2010) Solution-processed zinc oxide as high-performance air-stable electron injector in organic ambipolar light-emitting field-effect transistors. *Adv. Funct. Mater.*, **20** (20), 3457–3465. [121](#)

1

Chapter 7

Fabrication of Mesoporous ZnO via Blockcopolymer Co-Assembly

7.1 Introduction

Mesoporous ZnO with feature sizes on the 20-50 nm length scale has a number of attractive properties for emerging technological applications. The high surface area combined with the intrinsic properties of ZnO-based materials such as a direct band gap of 3.2 eV, and high charge carrier mobility make them desirable for use in organic and dye-sensitised solar cells, gas sensing and photocatalysis, to name a few.^[1-3]

However, realising a 3D mesoporous ZnO structure is still a challenge. Replication through atomic layer deposition (ALD), as presented in Chapter 5, carries tremendous potential, but a solution-based approach remains the only other feasible route. Other dry ZnO fabrication methods available, such as PLD or magnetron sputtering only allow isotropic deposition, making them unsuitable for 3D replication.

Solution-based metal oxide impregnation (as demonstrated in Chapter 6) pro-

vides another route to fabrication of mesoporous metal oxides, using BCP as a sacrificial template. Alternatively, block copolymers can also be used as a structure-guiding agent to realise mesoporous metal oxides, as discussed in Chapter 2. Despite the restrictions inherent to this method, it offers a simple, elegant fabrication route to mesoporous metal oxides. For this reason, numerous metal oxides such as SiO_2 , TiO_2 , ZrO_2 , and WO_3 have been successfully fabricated via BCP-guided coassembly.

These metal oxide sol-gel systems require a fine-tuned harmony of four conditions to lead to successful device fabrication. These include 1) nano-sized inorganic sol particles small enough to be incorporated into the block of polymer chains, 2) selective swelling of one block of the BCP by the sol particles, 3) a common solvent that dissolves both blocks and the sol particles equally well, and 4) gelation kinetics slower than that of BCP micro phase separation. Normally, the nano-sized inorganic sol particles and slow gelation kinetics are achieved by slowing down the hydrolysis kinetics of the metal oxide sol gel system.^[4]

However, synthesis of mesoporous ZnO using this method is particularly challenging due to ZnOs tendency to readily crystallise. Even if the above four conditions were met, the rapid growth of ZnO into wurtzite crystals upon nucleation, destroys the polymer scaffold, which in other systems such as TiO_2 often confines the crystal growth of the metal oxides, keeping the structure intact.^[5] For this reason, no successful BCP co-assembly route to mesoporous ZnO has yet been reported, though several studies have come close. Solution-based processing of mesoporous ZnO has been demonstrated with larger (>200 nm) pores by electrodeposition of ZnO into an inverse opal polystyrene structure^[6], although the large pore size limits potential applications.

Elsewhere, a solution impregnation method was presented by Lepoutre *textitetal.*^[7] using a hard silica scaffold with 20 nm pores, thereby confining the ZnO crystal growth. However, this system faces a different challenge, as ZnO and SiO_2 have a

similar chemistry and share similar chemical etchants (both acid and base), which poses difficulty in selectively etching the silica scaffold. Only a narrow pH window allows successful selective etching, and the detrimental effect of the etchant on the ZnO surface cannot be neglected. Altogether, the evidence of a simple, reliable route to thin film processing of ZnO is limited.

Herein, we search for a simple, reliable route to mesoporous ZnO using BCP coassembly, which can easily be processed in thin film form. In order to bypass the rapid crystal growth tendency of ZnO, we first synthesise ZnO nanocrystals (nc-ZnO), which act analogously to the inorganic sols in the BCP co-assembly sol gel system. Such a process can be visualised as illustrated in **Fig. 7.1** Other TCO materials such as Sn₂^[8], In-doped SnO₂^[9], and Sd-doped SnO₂^[10] have employed this nanocrystal route and achieved reasonable mesoporous structures on the 20 nm length scale. However, a coassembly method using nc-ZnO has thus far not been reported in the literature. Developing reliable, robust thin film processing techniques

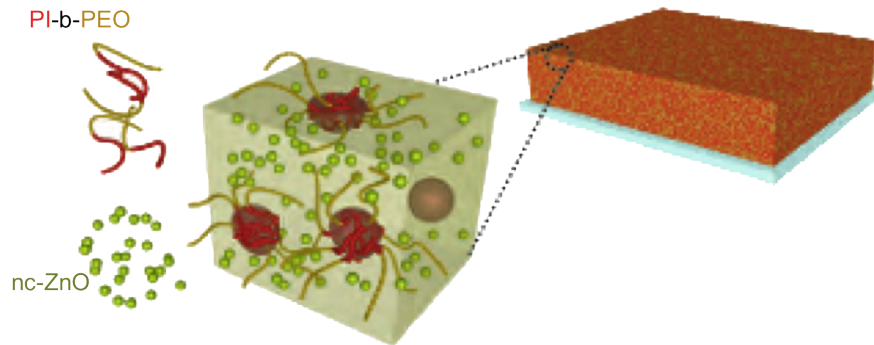


Figure 7.1: Schematics of using structure guiding PI-*b*-PEO to arrange nc-ZnO into a mesoporous structure. Modified from^[5] with permission.

for functional mesoporous metal oxides is not a straightforward problem. Although BCP coassembly of TiO₂ has long been studied, it was only recently that fabrication routes to mesoporous TiO₂ were established to a point that allows reliable thin film

processing, permitting exploitation in applications such as dye-sensitised solar cells and antireflection coatings. This is generally due to the conflicting requirements of the processing conditions for smooth film fabrication, and those that best induce BCP self assembly, notably slow solvent evaporation. Previous efforts towards thin film processing of porous 3D ZnO structures for use as a mesoporous active layer in organic solar cells^[11] exhibit evident room for improvement in terms of porosity and film quality.

As previously mentioned, the four crucial conditions required for this coassembly approach have not been previously met, due to the rapid crystallisation tendency of ZnO. In this chapter, we apply this technique to ZnO, using poly(isoprene-*b*-ethylene oxide) (PI-*b*-PEO) as the templating agent. The focus of this study was on establishing of a simple, reliable fabrication route to mesoporous ZnO films of high quality. Finally, the use of this material was demonstrated in an inverted organic hybrid solar cell.

7.2 Experimental

Materials

The chemicals used in this study are listed below.

- Methanol, HPLC grade, >99.9% (Sigma Aldrich)
- Chloroform, analytical grade, >99.9% (Fischer Scientific)
- Zinc acetate dihydrate ($\text{Zn}(\text{CH}_3\text{CO}_2)_2 \cdot \text{H}_2\text{O}$), 99.9% trace metals basis (Aldrich)
- Poly(isoprene-block-ethylene oxide) (PI-*b*-PEO)

The PI-*b*-PEO used in this work was synthesised and characterised by Juho Song and Morgan Stefik in Prof. Ulrich Wiesner's group in Cornell University, USA. The details of the synthesis and characterisation are summarised elsewhere.^[12] Two types of PI-*b*-PEO were used in this study of which the details

are summarised in 7.1.

PI- <i>b</i> -PEO	$M_{n,PI-b-PEO}$ [kg/mol]	N_{TOT}	$M_{n,PEO}$ [kg/mol]	N_{PEO}	f_{PEO}	PDI ($= \frac{M_w}{M_n}$)
PI- <i>b</i> -PEO-1	34.4	606	9.8	245	28.4	1.05
PI- <i>b</i> -PEO-2	91.6	1579	28.6	651	31.2	1.09

Table 7.1: Details of the BCPs used in this chapter

Synthesis of nc-ZnO

The synthesis method for nc-ZnO was based on and modified from that presented by Beek *et al.*^[13] In a three-neck round flask, 2.95g of Zinc acetate dihydrate was dissolved in 120 ml of anhydrous methanol at 60°C for 1 hour, stirring. A separately prepared solution of potassium hydroxide (1.48 g) dissolved in 65ml of methanol was added dropwise to the flask under vigorous stirring at 60 °C for 130 minutes from the time that addition of KOH solution began. Once the reaction is complete, the mixture as removed from the heat and left to cool to room temperature for over 2 hours. The solution was then centrifuged at 4000 rpm for between 30-90 minutes and the sediments were washed using fresh methanol. This process was repeated three times. The resulting nc-ZnO were analysed by dynamic light scattering (DLS) to measure their average diameter.

Preparation of mesoporous ZnO

PI-*b*-PEO was dissolved in Chloroform in a concentration between 5% and 10% depending on the experimental needs. The PI-*b*-PEO solution is slowly added using a glass pipet to the solution of nc-ZnO dispersed in chloroform. The % of nc-ZnO loading was calculated using

$$\frac{m(\text{ZnO})}{m(\text{ZnO}) + m(\text{PI} - b - \text{PEO})} \quad (7.1)$$

Removal of PI-b-PEO

PI-*b*-PEO was removed either by O₂ plasma etching (Diener Etcher, 100W), or thermal calcination at 450 °C in air.

Dynamic Light Scattering

Malvern Zetasizer was used to measure the size of nano crystals. 1 ml of nanocrystal solution of 2 wt% was collected in a quartz cuvet for the measurement.

X-ray Diffraction

Wide angle x-ray scattering (WAXS) measurements, were carried out using a Bruker D8 diffractometer. The samples were prepared on a Si substrate.

Photovoltaic device fabrication

The worm-like ZnO structures were fabricated on prepatterned ITO/glass substrates as described above. The poly(3-hexylthiophene) (P3HT) (from Reike Metals) polymers was dissolved in anhydrous chlorobenzene and spin-coated on the ZnO mesoporous layer. The samples were then transferred to a thermal evaporation chamber for WO₃ (10 nm), Ag (30 nm), and Al (60 nm) deposition under high vacuum (10 - 6 mbar). Finally, the devices were post-annealed at 140 °C for 10 mins.

Photovoltaic performance characterization

For External Quantum Efficiency (EQE) measurements (in air) a 250 W tungsten halogen lamp and an Oriel Cornerstone 130 monochromater were used. The measurements were performed as a function of wavelength at intensities 1 mW/cm³. To measure the $J - V$ curve of the device under AM1.5 conditions, an ABET Solar 2000 solar simulator was used. In order to obtain reliable data, a spectral mismatch correction is carried out using a calibrated and certified inorganic solar cell.

7.3 Results and Discussion

7.3.1 Solvent and size requirements for nc-ZnO

Once synthesised, nc-ZnO can only be dispersed in methanol at low concentrations (<10 mg/ml). In addition, methanol does not solvate PI and PEO block equally. Therefore, it was required to find a common solvent for the nanocrystals and PI-*b*-PEO. The nanocrystals were re-dispersed in THF, toluene, chloroform, and an azeotrope of 1-butanol/toluene, which are good solvents for both PI and PEO blocks. Out of the tested solvents, chloroform proved to be the only solvent in which nc-ZnO dissolved well and no ligands were required to reach solubility up to 80mg/ml. In the other solvents, the solution turned cloudy upon dispersing the nano crystals (ncs) and stayed cloudy even after 1 hour of ultra-sonication, which was an attempt to separate temporarily aggregated ncs.

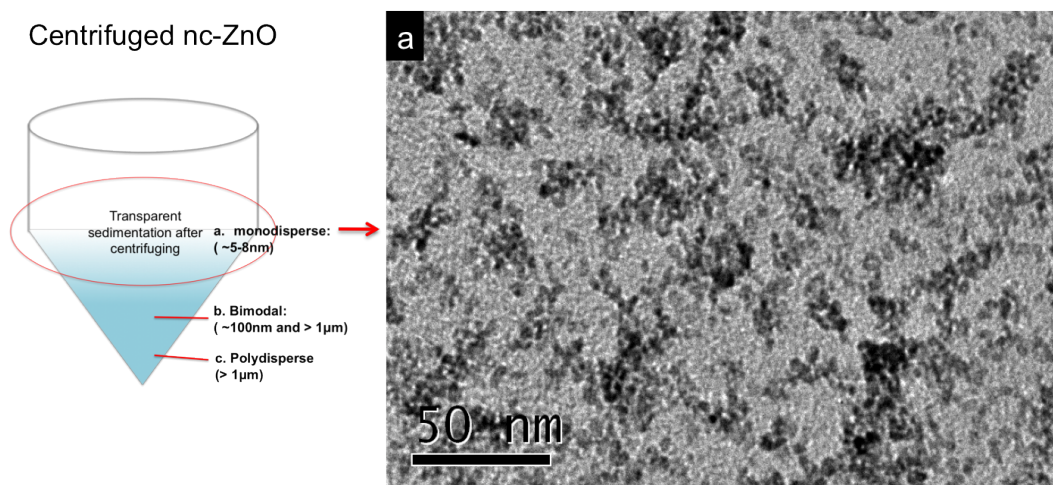


Figure 7.2: Illustration of collection of the centrifuged nanocrystals and their size measurements. Only the top transparent layer (a) exhibited monodisperse ~ 5 nm size distribution, which was also confirmed by TEM. The heavier particles in (b) and (c) regions, collected below the transparent layer, turned out be too large for the purpose of this study.

Upon washing the nc-ZnO in methanol three times, the nc-ZnO was centrifuged

once more. **Fig. 7.2** illustrates the type of sedimentation obtained upon centrifuging. The particles at the top (**Fig. 7.2 a**) demonstrated almost transparent layer whereas the bottom parts (b and c region in **Fig. 7.2**) were white. The nanocrystals were separately collected from three different parts of the sediments and dispersed in chloroform (~ 10 mg/ml) and the solutions were ultra-sonicated for 10 minutes to break apart aggregated particles before measuring their size using DLS. Only the top transparent particles were found to show particle sizes ranging between 5-7 nm. The particle sizes were confirmed by the transmission electron microscopy (**Fig. 7.2**) where mono-disperse ZnO nanocrystals of 5-7 nm were observed, consistent with what was observed in^[13]. Therefore, only the transparent top portion of the sedimented nano crystals were used for co-assembly experiments.

As discussed in Chapter 2, the size of ncs play an important role in their BCP guided assembly. The diameter of the ncs must be less than 5 nm for the BCP used in this study, as the radius of gyration for the PI-*b*-PEO is around 8 nm. Therefore, the diameter of synthesised nano crystals were in the upper limit of the suitable range. Efforts were made to synthesise nc-ZnO of smaller diameters by varying the concentration of KOH (decreasing) and the synthesis temperature. However, these approaches lead to other challenges such as difficulties in sedimenting the ncs and low yield.

7.3.2 Thin film Deposition methods

Once the symmetric solvent and small enough nano crystals were established, the next set of challenges include control of the kinetics of three competing systems: 1)the aggregation of nano crystals upon introducing PI-*b*-PEO into the system, 2)selective insertion of the ncs into the PEO block and 3)micro-phase separation of the BCP. In an ideal situation, the nano crystals must be incorporated first and followed by BCP-like micro-phase separation into a self-assembled morphology,

before finally the aggregation of nc-ZnO occurs.

For the BCP to self assemble into a periodic morphology, it is favourable to let the solvent to evaporate slowly, allowing the system to reach equilibrium. On the other hand, nc-ZnO without the ligands are often not in a stable state, especially when mixed with BCPs, and easily form agglomerates of size larger than what can be incorporated into the PEO block. Therefore, a narrow window where the three competing systems are at a balance must be reached in order to obtain a mesoporous structure. In order to investigate the kinetics, three deposition methods were studied: spin coating, blade coating, and drop casting, which have different solvent evaporation times. Moreover, the main challenge of solution processed mesoporous TCO-type materials is to deposit them in a smooth thin film form. Often, poor film quality is observed involving a rough top surface, uneven thickness throughout the film, formation of powder and flaking off of the substrate surface. Therefore, the three deposition methods were evaluated in terms of both the film quality and the resulting mesoporous morphology.

Drop casting

Drop casting proved to be an inappropriate method for preparation of mesoporous nc-ZnO thin film. Despite various substrate cleaning methods attempted (e.g. piranha etching, O₂ plasma etching), the wettability of the droplet was poor. The dried solution formed islands exhibiting numerous cracks, and upon removal of BCP through thermal calcination at 450°C, the film turned into powdery flakes of white with a slight tint of yellow colour. As shown in the SEM images (**Fig. 7.3**), the sample areas are dominated by aggregated nanocrystals instead of nanocrystals patterned into a porous matrix. This indicates that slow drying over a duration longer than 10 minutes, which was the time it took for the drop to dry, overtaken by the kinetics of aggregation of nanocrystals, which in turn hindered the incorporation of ncs into the PEO block.

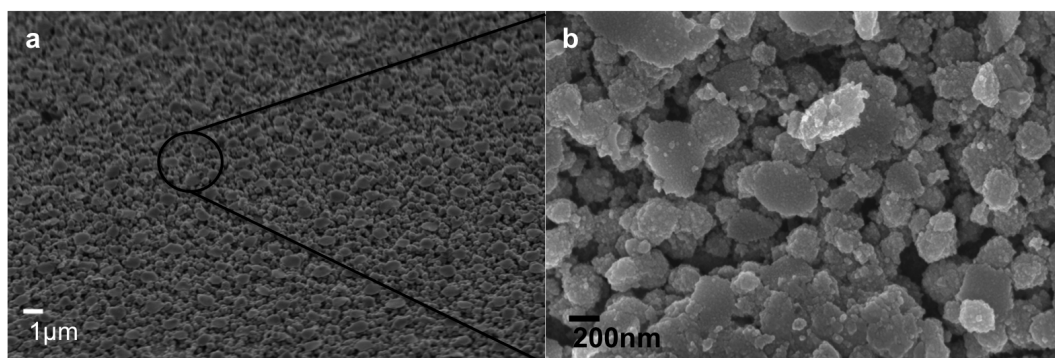


Figure 7.3: ZnO/PI-*b*-PEO (50% loading of ZnO) mixture drop casted and thermally calcined at 450°C

Blade coating

Mesoporous structure was observed in the films. Because chloroform evaporates quickly, blade coating resulted in drying of the solvents within seconds of deposition. In addition, solvents with concentrations higher than 5 wt% resulted in poor film quality, as it seemed that the solvent evaporated too quickly before the deposition was complete. Therefore, there was a discrepancy of thickness between the starting and finishing areas of the coating. For example, when 100 l of solution was deposited and 30m blade was used, one end of the sample was 350 nm thick, but the other end of the film had a thickness of 1.8m, clearly indicating that the solution concentration drastically changed during the coating process. Moreover, the thicker part of the film often was inhomogeneous exhibiting many cracks. (Fig. 7.4)

Spin coating

It appeared that spin coating provides the best compromise between the kinetics of nc-ZnO aggregation and micro phase separation due to the fast solvent evaporation kinetics that spin coating offers. As shown in Fig. 7.5, Fig. 7.6 a and Fig. 7.6 b , aggregated nano particles were not observed in spin coated samples, and a wormlike mesoporous structure, which seems to have resulted from kinetically trapping of BCP micro-phase separation due to fast solvent evaporation, was observed. More

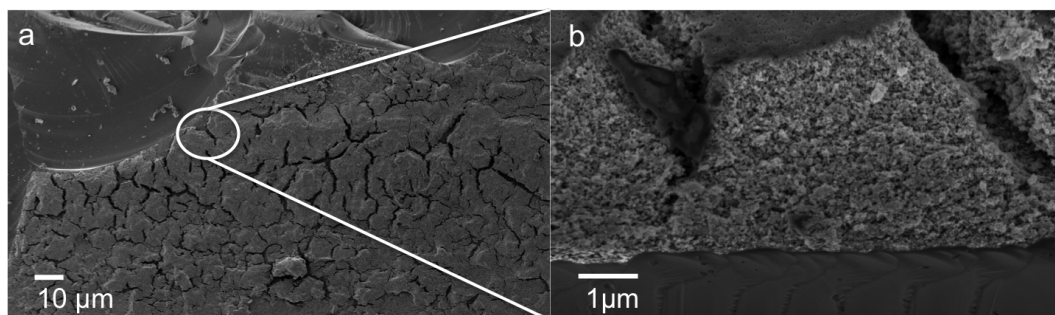


Figure 7.4: PI-*b*-PEO (50% loading of ZnO) mixture blade-coated and thermally calcined at 450°C. (a) Top view of the cracked film surface and (b) cross sectional view of the film. Some mesoporous structures are observed underneath the compact layer on top.

importantly, unlike the films prepared using drop casting and blade coating where flaking and peeling were often observed, the resulting film was smooth, crack free, and consistent over the entire substrate area (1.4 cm × 1.4 cm). When the nc-ZnO dispersed in chloroform at 80 mg/ml without the BCP is spin coated, the resulting film presented a dense film of 70 nm thickness, corresponding to 1/6 of the thickness of those that contain 40 mg of nc-ZnO and 35 mg of PI-*b*-PEO. (**Fig. 7.6 c**)

Upon removal of PI-*b*-PEO-1, a mesoporous structure with pore sizes varying between 20 nm and 30 nm was observed. Although the porous structure does not exhibit periodicity observed in self-assembled arrangements, it appeared to follow similar trends to what has been observed from BCP coassembly of TiO₂, which was realised by employing the same BCP, in two ways.^[14] Firstly, it appeared that increasing the metal oxide content relative to the polymer increased the thickness of the pore walls creating a more dense network while slightly decreasing the pore sizes. As shown in **Fig. 7.5**, 75% loading of ZnO resulted in a pore wall thickness ~30 nm whereas 50% lead to thinner pore walls (~20 nm) In addition, using a BCP with higher molecular weight (PI-*b*-PEO-2) lead to a clear increase in the pore dimensions of the structure. Based on the SEM characterisation, ((**Fig. 7.7 b**)), the pore dimension of the structure obtained by using PI-*b*-PEO-2 ranged from

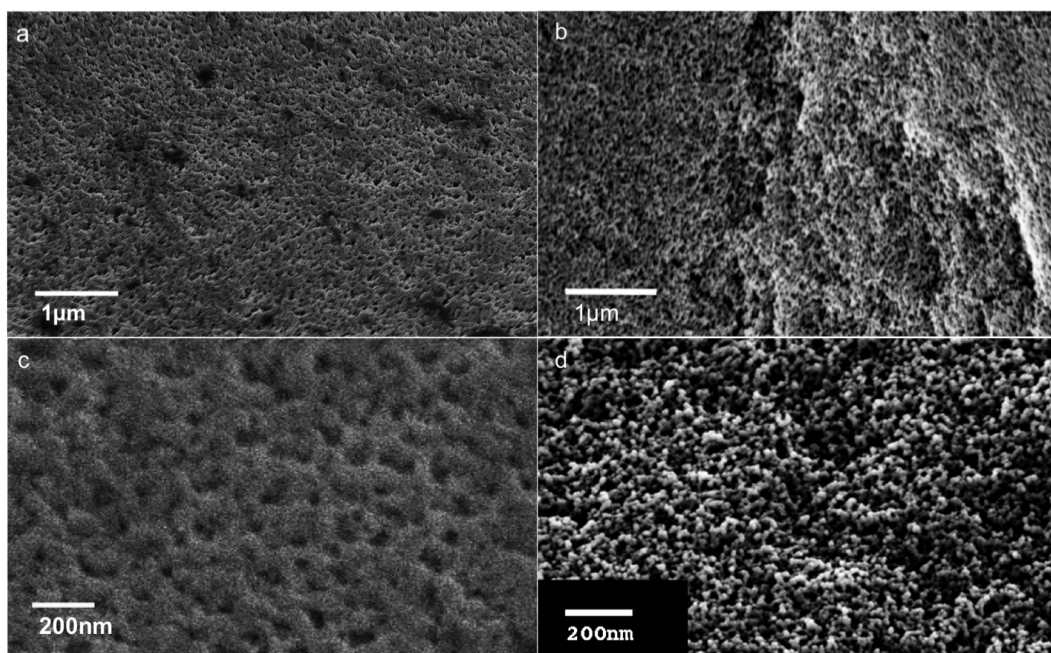


Figure 7.5: Mesoporous ZnO prepared by PI-b-PEO-1 with different % of nc-ZnO loading. (a) and (c) are images of 75% ZnO, (b) and (d) represent 50% ZnO loading

40 nm-50 nm, which is in reasonable agreement with expected increase in pore sizes. The pore size is dependent on the molecular weight of the minority block (PI), and increasing its molecular weight from 24.8 kg/mol to 63 kg/mol means that radius of gyration, when the BCP is dissolved in a good solvent, scales up by 1.6. Therefore, the observed pore size increase from 20-30 nm to 40-50 nm is reasonable.

The lack of long range order in the porous structures obtained using both BCPs can be attributed to several factors. The fast evaporation kinetics of spin coating or blade coating where the solvent evaporated in less than a minute is not favourable for inducing BCP equilibrium self assembly, as the system does not have enough time to reach equilibrium. However, as observed from drop casting, nc-ZnO aggregates during slow solvent evaporation. This may be combined with a possibility that hydrophilic interaction between the nc-ZnO and PEO is not very strong, leading to lose incorporation of nc-ZnO into PEO blocks, creating a mesoporous structure

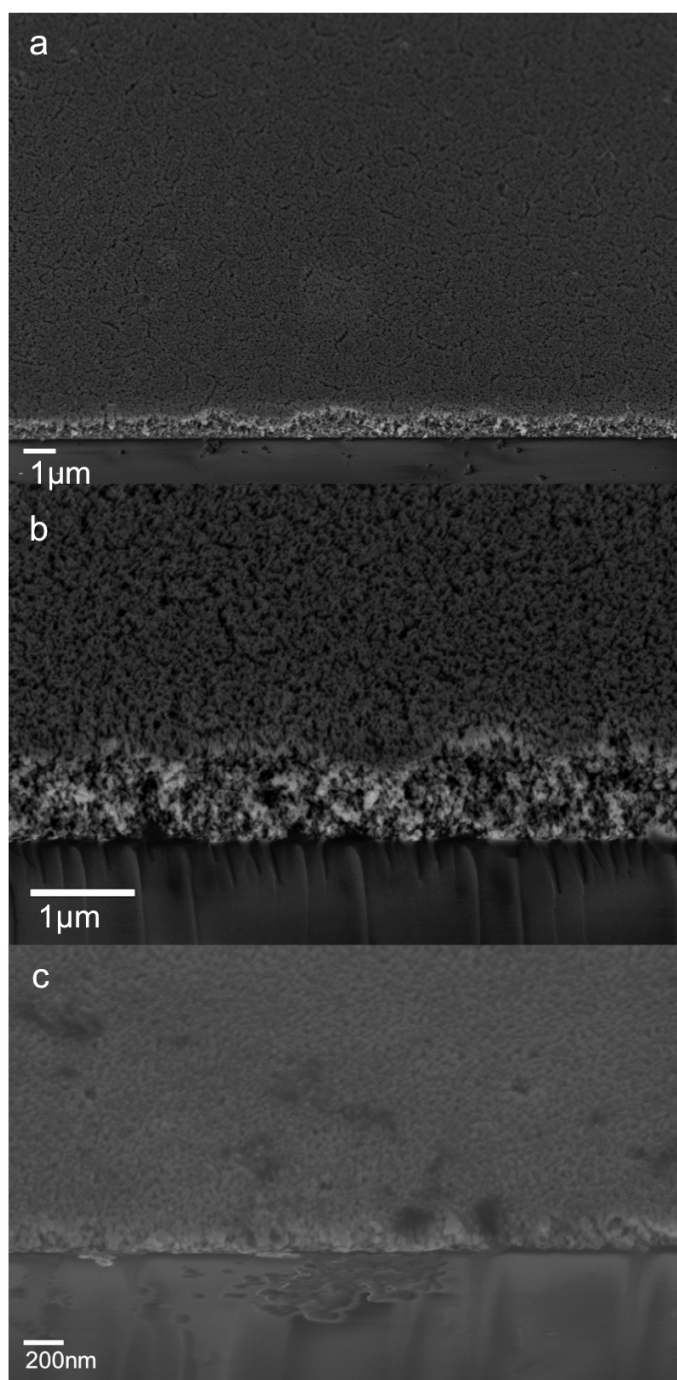


Figure 7.6: SEM representation imaged using 45° stubs. (a) low magnification view, demonstrating the mesoporous film of smooth, crack-free film quality, (b) and the wormlike, mesoporous morphology consistent throughout the film, and (c) a thin film prepared by nc-ZnO dispersed in chloroform (80 mg/ml), demonstrating a lack of porosity as well as a much decreased thickness

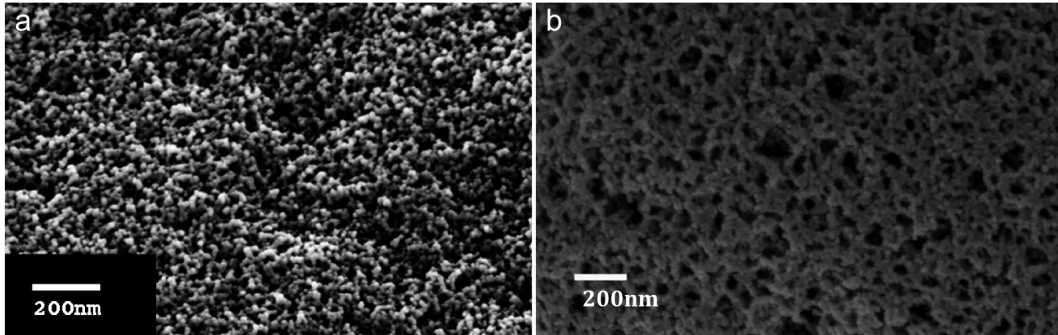


Figure 7.7: Mesoporous ZnO prepared at 50% ZnO loading by (a) PI-*b*-PEO-1 and (b) PI-*b*-PEO-2.

without a well-defined self assembled nanocrystal arrangements. In addition, perhaps the diameter of the nano crystals are required to be even smaller for them to be effectively incorporated into the PEO block.

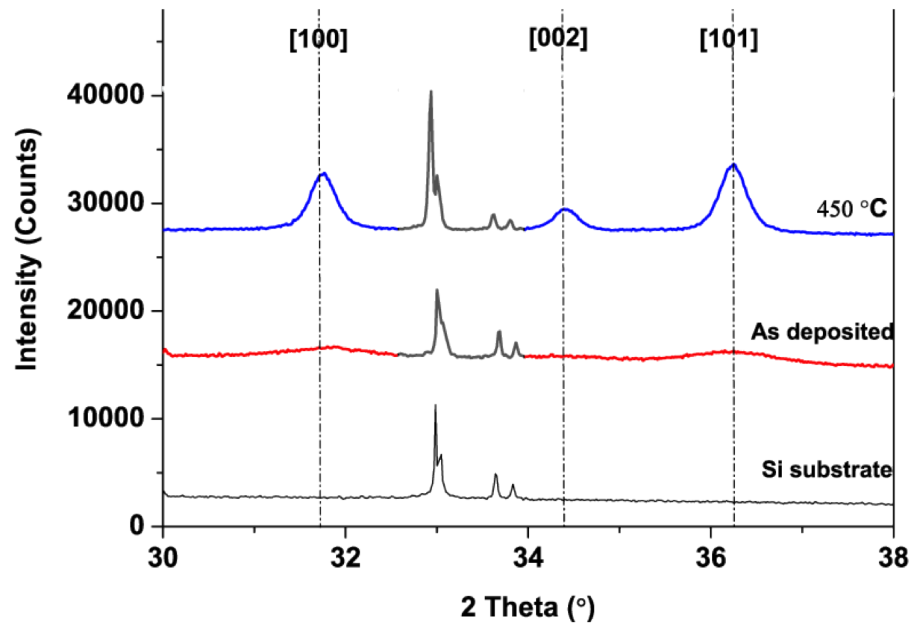


Figure 7.8: X-Ray Diffraction spectra of as deposited mesoporous ZnO and mesoporous ZnO thermally calcinated at 450°C

The mesoporous structures were characterised using XRD and the peaks corresponding to ZnO were observed. Unlike the nc-TiO₂ and ITO systems presented

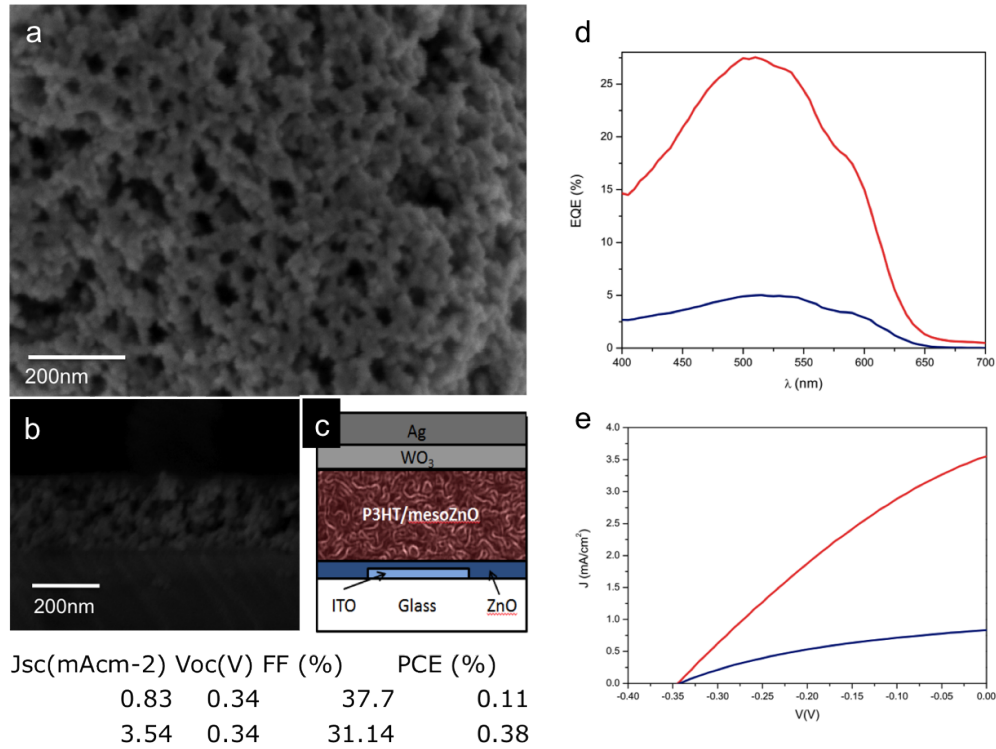


Figure 7.9: (a) The top view and (b) cross-sectional view of ZnO/P3HT solar cell device whose device architecture is illustrated in (c). The performance of the solar cell was recorded in terms of (d) EQE graph, (e) $J - V$ curve and the measurement values as summarised in the table at the bottom of the figure

in the recent report by Buonsanti et al^[9], the nc-ZnO did undergo clear crystallite growth after calcination at 450°C. The crystallite sizes were analysed from the XRD spectra using Debye-Scherrer equation for the sample after calcination at 450°C. Upon heating, the nc-ZnO appears to have grown from 5 nm (based on the TEM and DLS assessment) size of crystallite changes to approximately 20 nm. (**Fig. 7.8**)

7.3.3 Potential in Solar cell Applications

The mesoporous ZnO layer was then used to build a ZnO/P3HT device, in order to demonstrate its use in solar cell applications. A thickness of 200 nm was chosen based on the previous results of the best performing active layer thickness for

ZnO nanowires (NW)/P3HT cells, which exhibited improved performance compared to a bilayer ZnO/P3HT device.^[15] In order to allow room for the bulky PCBA molecules (a type of SAM- refer to Chapter 2) to coat the ZnO surface first and then fill the rest of the voided area, a pore size larger than 40 nm was preferable. Therefore, PI-*b*-PEO-2 was used to generate an active layer of pore sizes ranging from 35-50 nm. In the previous report on ZnO/P3HT solar cells using nc-ZnO paste, it was reported that devices built using 24 nm nano crystals were higher performing than those using 5 nm sized crystals.^[11] The layer was annealed at 450°C, which results in complete removal of the BCP as well as in a crystallite size of 20 nm.

The short circuit currents for both SAM modified and unmodified devices (3.54 mA/cm² and 0.83 mA/cm²) are significantly improved over that of a bilayer ZnO/P3HT device (0.47 mA/cm²) fabricated in the same device architecture^[16]. This can be explained by the much increased interfacial area of the P3HT/ZnO at which excitons can disassociate into charges which contribute to the photocurrent. Moreover, the SAM-modified cell exhibited higher short circuit current (J_{SC}) and open circuit voltage (V_{OC}) compared to the ZnO/P3HT device built using ZnO nanowires of 200 nm (2.5 mA and 0.19 V).^[15] Finally, the poor fill factors (FF), although comparable to those of ZnONW/P3HT devices (37%), suggest that charges are not extracted efficiently from the device. This is likely to result from the variations in film thickness and surface roughness which limit charge transport and extraction. However, the PCE and EQE of the cells are promising as they are comparable to or better performing than the previous reports of P3HT/ZnO nanocrystal mesoporous layers, clearly demonstrating potential as an active layer material for this system.^[11]

7.4 Conclusions

In this chapter, we have investigated a new fabrication route to mesoporous ZnO by using BCP as a structure guiding agent. nc-ZnO of diameter ~ 5 nm was synthesised and characterised, in order to avoid uncontrolled crystallisation behaviour often observed from ZnO sol gel process. PI-*b*-PEO was used in order to selectively incorporate the nc-ZnO into the PEO block. By using PI-*b*-PEO of two different molecular weights, 34 kg/mol and 91.6 kg/mol, average pore-sizes of the structure were varied from 20 nm-30 nm range to 40 nm-50 nm. Due to the competing kinetics between nc-ZnO aggregation and BCP self assembly, quenching the system under fast solvent evaporation kinetics allowed the incorporation of nc-ZnO into the PI-*b*-PEO network leading to mesoporous ZnO upon removal of PI-*b*-PEO. The lack of periodicity was attributed to several factors such as insufficient time given for the PI-*b*-PEO to self assembly and possibility of ZnO-PEO attraction being not strong enough for selective swelling of PEO. Nevertheless, a reliable thin film processing route to mesoporous ZnO was established.

The application of mesoporous ZnO was demonstrated by its use as an active layer in an inverted ZnO/P3HT hybrid solar cell, which exhibited superior performance to ZnONW-based devices of the same thickness under the same device fabrication conditions. The PCE and EQE values are comparable to the reported ZnO/P3HT solar cells which employ mesoporous nc-ZnO.^[11] Therefore, future work remains in exploiting this material system to improve the solar cell performance. The size and shape of the nc-ZnO as well as the active layer thickness are reported to greatly affect the solar cell performance.^[11] Therefore, scanning the solar cell performance by varying the active layer thickness, which is easily processable using the fabrication route introduced in this chapter, can further optimise the solar cell performance. It is also worth noting that nc-ZnO exhibited crystallite growth upon heating. Therefore, varying the annealing temperature and examining the

solar cell performance also can be useful.

Bibliography

- [1] Zhang, Q., Dandeneau, C.S., Zhou, X., and Cao, G. (2009) ZnO nanostructures for dye-sensitized solar cells. *Adv. Mater.*, **21** (41), 4087–4108, doi:10.1002/adma.200803827. [128](#)
- [2] Dhawale, D. and Lokhande, C. (2011) Chemical route to synthesis of mesoporous ZnO thin films and their liquefied petroleum gas sensor performance. *Journal of Alloys and Compounds*, **509** (41), 10 092–10 097, doi:10.1016/j.jallcom.2011.08.046.
- [3] Jang, Y., Kochuveedu, S., Cha, M., Jang, Y., Lee, J., Lee, J., Lee, J., Kim, J., Ryu, D., and Kim, D. (2010) Synthesis and photocatalytic properties of hierarchical metal nanoparticles/ZnO thin films hetero nanostructures assisted by diblock copolymer inverse micellar nanotemplates. *Journal of Colloid and Interface Science*, **345** (1), 125–130. [128](#)
- [4] Lee, J., Orilall, M.C., Warren, S.C., Kamperman, M., Disalvo, F.J., and Wiesner, U. (2008) Direct access to thermally stable and highly crystalline mesoporous transition-metal oxides with uniform pores. *Nat Mater*, **7** (3), 222–228, doi:10.1038/nmat2111. [129](#)
- [5] Guldin, S., Huttner, S., Tiwana, P., Orilall, M.C., Ulgut, B., Stefik, M., Docampo, P., Kolle, M., Divitini, G., Ducati, C., Redfern, S.A.T., Snaith, H.J., Wiesner, U., Eder, D., and Steiner, U. (2011) Improved conductivity in dye-sensitised solar cells through block-copolymer confined TiO₂ crystallisation. *Energy Environ. Sci.*, **4**, 225–233. [129](#), [130](#)
- [6] Ramirez, D., Bartlett, P., Abdelsalam, M., Gomez, H., and Lincot, D. (2008) Electrochemical synthesis of macroporous zinc oxide layers by employing hydrogen peroxide as oxygen precursor. *phys. stat. sol. (a)*, **205** (10), 2365–2370. [129](#)
- [7] Lepoutre, S., Julián-López, B., Sanchez, C., Amenitsch, H., Linden, M., and Grosso, D. (2010) Nanocasted mesoporous nanocrystalline ZnO thin films. *J. Mater. Chem.*, **20** (3), 537, doi:10.1039/b912613a. [129](#)
- [8] Ba, J., Polleux, J., Antonietti, M., and Niederberger, M. (2005) Non-aqueous synthesis of tin oxide nanocrystals and their assembly into ordered porous mesostructures. *Adv. Mater.*, **17** (20), 2509–2512, doi:10.1002/adma.200501018. [130](#)

- [9] Buonsanti, R., Pick, T., Krins, N., Richardson, T., Helms, B., and Milliron, D. (2012) Assembly of ligand-stripped nanocrystals into precisely controlled mesoporous architectures. *Nano Letters*, **12** (7), 3872–3877. [130](#), [142](#)
- [10] Müller, V., Rasp, M., Rathouský, J., Schütz, B., Niederberger, M., and Fattakhova-Rohlfing, D. (2010) Transparent conducting films of antimony-doped tin oxide with uniform mesostructure assembled from preformed nanocrystals. *Small*, **6** (5), 633–637, doi:10.1002/smll.200901887. [130](#)
- [11] Bouclé, J., Snaith, H., and Greenham, N. (2010) Simple approach to hybrid polymer/porous metal oxide solar cells from solution-processed zno nanocrystals. *The Journal of Physical Chemistry C*, **114** (8), 3664–3674. [131](#), [143](#), [144](#)
- [12] Allgaier, J., Poppe, A., Willner, L., and Richter, D. (1997) Synthesis and characterization of poly [1, 4-isoprene-b-(ethylene oxide)] and poly [ethylene-co-propylene-b-(ethylene oxide)] block copolymers. *Macromolecules*, **30** (6), 1582–1586. [131](#)
- [13] Beek, W., Wienk, M., Kemerink, M., Yang, X., and Janssen, R. (2005) Hybrid zinc oxide conjugated polymer bulk heterojunction solar cells. *The Journal of Physical Chemistry B*, **109** (19), 9505–9516. [132](#), [135](#)
- [14] Nedelcu, M., Lee, J., Crossland, E.J.W., Warren, S.C., Orilall, M.C., Guldin, S., Huttner, S., Ducati, C., Eder, D., Wiesner, U., Steiner, U., and Snaith, H.J. (2009) Block copolymer directed synthesis of mesoporous tio2 for dye-sensitized solar cells. *Soft Matter*, **5**, 134–139, doi:10.1039/B815166K. URL <http://dx.doi.org/10.1039/B815166K>. [138](#)
- [15] Vaynzof, Y. (2011) Improved photoinduced charge carriers separation in organic-inorganic hybrid photovoltaic devices. *PhD Dissertation*, pp. 118–135. [143](#)
- [16] Vaynzof, Y., Kabra, D., Zhao, L., Ho, P., Wee, A., and Friend, R. (2010) Improved photoinduced charge carriers separation in organic-inorganic hybrid photovoltaic devices. *Applied Physics Letters*, **97** (3), 033 309–033 309–3. [143](#)

Chapter 8

Conclusions and Future Work

In this thesis, reliable synthetic routes to 3D nanoarchitectures of ZnO-based materials have been established using three distinct approaches. Unlike other metal oxide systems such as TiO_2 and Al_2O_3 , fabrication of nanostructured TCOs, especially ZnO-based materials, have been a challenging task, due to difficulties of controlling the materials crystallisation behaviour. To date, a reliable route to thin film of ZnO-based materials of well-defined 3D nanostructure on the 20-40 nm length scale is yet to be reported. Nevertheless, the application potentials of these materials are enormous.

The key parameters to establishing a reliable, consistent fabrication routes were revealed, and their application potentials were demonstrated through either 1) using them as part of solar cell or 2) evaluating the electrical and optical properties, which correspond directly to the figure of merit of TCO materials.

Fabrication of nanostructured ZnO involved using sacrificial BCP as either a morphology replication tool or a structure directing agent. Before that, a thin film preparation route to the sacrificial polymeric template, to be used for replication, was explored using PS-b-PI (Chapter 4). The three approaches taken for the 3D ZnO fabrication include: 1) Atomic layer deposition of ZnO to replicate the 3D bicontin-

uous structure of sacrificial PS template, which has gyroid or wormlike morphologies (Chapter 5), 2) Solution impregnation of In-Ga-ZnO into the sacrificial polymeric template (identical to that used for (Chapter 6) 1)) to replicate the morphologies, 3) Co-assembly of nc-ZnO with sacrificial PI-b-PEO, which guides the nc-ZnO to 3D assembled structure via microphase separation (Chapter 7). While both gyroid and wormlike PS templates provided self-standing, 3D structures of interconnected pores, they had distinct strengths and weaknesses in a technological point of view. Gyroid templates provide extreme order and periodicity, which could be a benefit to applications, which require consistency throughout the structure. However, the fabrication process is rather time consuming and delicate. Wormlike morphology on the other hand, is much quicker and more reliable to process, at an expense of the extreme periodicity within the bicontinuous structure. The surface of resulting PS template is made hydrophilic, rich in OH group due to the UV and EtOH exposure during the selective removal of the minority (PI) block. This is advantageous for deposition of metal oxides into the pores of the substrate.

For the ALD of ZnO, the OH groups on the polymer surface acted as the binding sites to DEZ. Therefore, abundance of OH groups allowed for conformal coating instead of cluster formation. Because the channel diameter is only $\sim 30\text{-}40\text{nm}$, cluster formation can cause pore blocking, preventing the precursor molecules to diffuse deeper into the film.

For impregnation of IGZO into the polymer templates, hydrophilicity of the template surface allows the metal precursor solution to fully infiltrate throughout the pores. Upon infiltration of the precursor solution, thin film preparation of porous IGZO was found to be best prepared by blade coating followed by slow evaporation of the solvent. Finally, using PI-b-PEO directed co-assembly of nc-ZnO, an alternative processing route to mesoporous ZnO thin films to that using ALD was presented. Although the structure is less well-defined as those prepared by ALD replication,

this method presents other benefits such as inexpensive preparation methods and the possibility to fabricate thicker films ($i\mu\text{m}$) by multiple spin coating. It is suspected that the structure definition can be improved by allowing a stronger hydrophilic interaction between the nc-ZnO and the PEO block leading to clearer selective incorporation of the nc-ZnO into the PEO phase. Slow solvent evaporation to allow structure formation was not suitable in the case of this system due to the faster aggregation kinetics of nc-ZnO compared to that of reaching a self-assembled state. The recently reported ligand-stripping of the naturally formed ligands of nanocrystals seem to be a promising attempt to induce a stronger hydrophilic interaction between nc-ZnO and PEO.¹

Implementing the mesoporous ZnO layers from Chapter 5 and Chapter 7 into an inverted hybrid P3HT/ZnO solar cells demonstrated that such materials can indeed function as an active material. At present, the efficiencies of these devices are comparable to those reported from devices fabricated using nc-ZnO paste. The mesoporous nc-ZnO layers resulted in higher performance to those built using ALD-replicated ZnO based ones, despite the similar active layer thicknesses. This is suspected to be mainly attributed to difference in electronic structures of the materials prepared via two distinct routes. Gaining further insights on structure formation, transport behaviour of mesoporous ZnO, and optimisation of device fabrication should be the next obvious step to proceed. In addition, properly examining and tuning of the electronic structure (e.g. work function, HOMO/LUMO levels) of the ZnO surface should enable improvement of solar cell performance.

¹Rosen, E. L., Buonsanti, R., Llordes, A. *et al.*, (2012) *Exceptionally Mild Reactive Stripping of Native Ligands from Nanocrystal Surfaces by Using Meerwein's Salt*, *Angewandte Chem. Int. Ed.*, (51) 684-689

Extension to Other TCO Systems: Preliminary Results

ALD of SnO₂ Gyroid

The materials toolbox developed in this study can be further extended to ALD of other metal oxides such as TiO₂, SnO₂, and Sn:ZnO. Some of the efforts have started in the course of this study. In collaboration with Professor Roy Gordon's group in Harvard University, gyroid of SnO₂ was fabricated using the precursors synthesised in their group.¹ However, XPS examination showed that, some problems remain in this system. The flat Si substrate which was placed in the same chamber as the gyroid substrate resulted in a thin film of correct stoichiometric ratio, based on the XPS surface scan. The gyroid SnO₂ (**Fig. 8.1**), on the other hand, did not show any corresponding peaks for SnO₂. This could be due to various factors such as the precursors reacting with the PS template, forming an alternative compound to SnO₂. It is also possible that extended exposure time at 60°C lead to dissociation of H₂O₂, which was used as a precursor, or that the byproduct as well as the dissociated species were trapped inside the pores of gyroid network, overall affecting the final stoichiometry of the material. Confirming such hypotheses would require further elemental analysis such as XPS depth profiling and more detailed analysis, starting with ALD of SnO₂ on a flat PS substrate.

¹Heo, J. and Hock, A.S. and Gordon, R.G. (2010) *Low Temperature Atomic Layer Deposition of Tin Oxide*, Chemistry of Materials, **22** (17), 4964

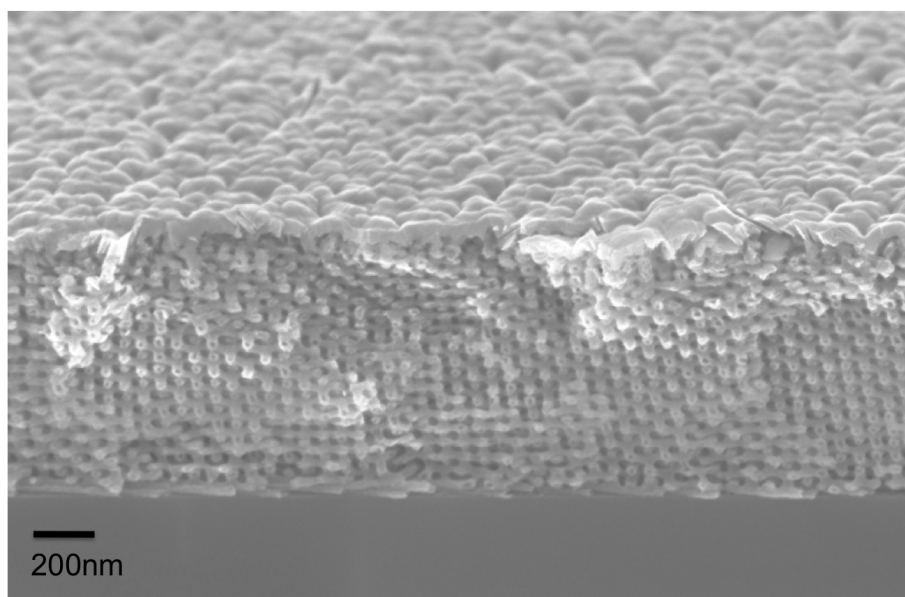


Figure 8.1: SEM image of resulting material from ALD of SnO_2 into a sacrificial PS gyroid template (from Chapter 4). The image was taken after removing the PS template by thermal calcination.

Dye-sensitised Solar Cells (DSSC) Using Mesoporous ZnO

The mesoporous ZnO fabricated in Chapter 7 was used as an active layer in DSSC using a D102 dye. The J-V curve of such device (**Fig. 8.2**) shows high V_{oc} (in comparison to other ZnO-based DSSCs¹), but a low J_{sc} . This could be due to the fact that the active layer was too thin ($\sim 450\text{nm}$), relative to the those of the DSSCs reported in literature. The highest PCE reported on ZnO-based DSSCs are only $\sim 2.5\%$, and used an active layer of $>10\mu\text{m}$. Therefore, optimising the multiple spin coating conditions to prepare thin films in micron-scale can be a valuable step to improve the solar cell performance.

¹Ko, SH., Lee, D., Kang, HW., *et al.*, (2011) *Nanoforest of Hydrothermally Grown Hierarchical ZnO Nanowires for a High Efficiency Dye-Sensitized Solar Cell*, Nano Letters, **11** (2), 666-671

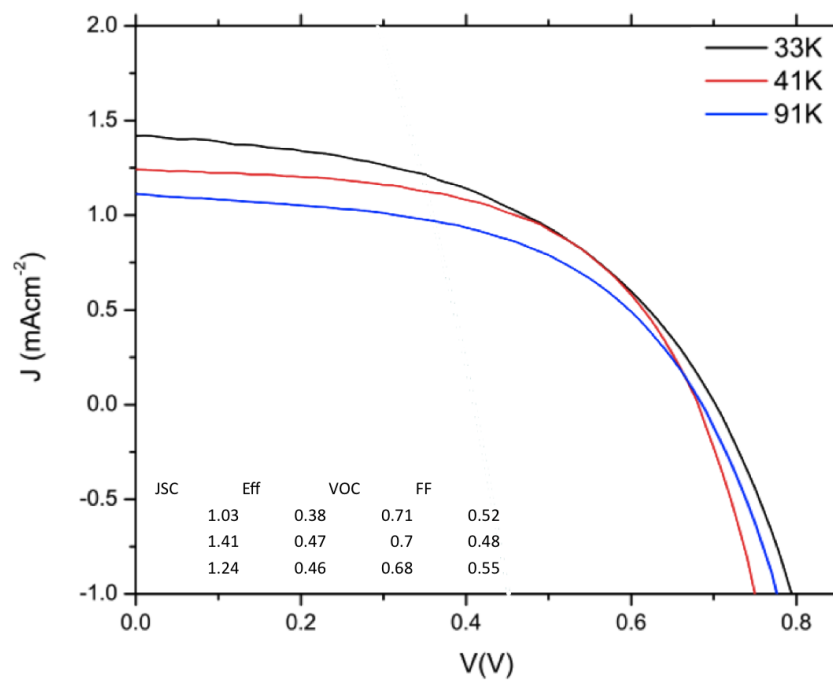


Figure 8.2: $J - V$ curve of a DSSC built using the mesoporous ZnO (450nm-thick) from Chapter 7 as an active layer.